INSIGHTS INTO GLIOMA INITIATION AND MAINTENANCE THROUGH THE ANALYSIS OF MUTANT BRAF AND HBEGF

by

Clifford H. Shin

A dissertation submitted to the faculty of
The University of Utah
in partial fulfillment of the requirements for the degree of

Doctor of Philosophy

Department of Oncological Sciences

The University of Utah

December 2016

The University of Utah Graduate School

STATEMENT OF DISSERTATION APPROVAL

The dissertation of **Clifford H. Shin**

has been approved by the following supervisory committee members:

Sheri L. Holmen	, Chair	**06-20-16** Date Approved
Howard Colman	, Member	**06-20-16** Date Approved
Daniel Webster Fults III	, Member	**06-20-16** Date Approved
Matthew W. VanBrocklin	, Member	**06-20-16** Date Approved
Katherine Elena Varley	, Member	**06-20-16** Date Approved

and by **Bradley Cairns** , Chair/Dean of

the Department/College/School of **Oncological Sciences**

and by David B. Kieda, Dean of The Graduate School.

ABSTRACT

Gliomas are the most common primary brain tumor and are associated with a poor prognosis. Understanding the essential factors in the formation of these tumors is critical to improve the treatment of this disease. We report a thorough investigation of two potential drivers in the formation and maintenance of low-grade and high-grade gliomas – the kinase domain of BRAF and activated HBEGF.

BRAF fusions have been observed in a majority of sporadic pilocytic astrocytomas, a low-grade glioma. In each fusion, the autoinhibitory domain of BRAF is lost, which results in activation via the retained kinase domain (BRAF-KD). Somatic cell gene transfer of the BRAF-KD alone did not cause tumors to develop; however, low-grade gliomas were detected in mice when combined with *Ink4a/Arf* loss. Pharmacologic inhibition of MEK and PI3K inhibited cell growth and induced apoptosis in astrocytes expressing BRAF-KD. Our findings demonstrate that the BRAF-KD can cooperate with *Ink4a/Arf* loss to drive the development of gliomas.

Heparin-binding epidermal growth factor (EGF)-like growth factor (HBEGF) is a ligand for the epidermal growth factor receptor (EGFR), one of the most commonly amplified receptor tyrosine kinases (RTK) in glioblastoma (GBM), a high-grade glioma. While HBEGF has been found to be expressed in a subset of malignant gliomas, its sufficiency for glioma initiation has not been evaluated. In this study, we demonstrate that

HBEGF can initiate GBM in mice in the context of *Ink4a/Arf* loss and *Pten* loss, and that these tumors are similar to the classical GBM subtype observed in patients. Isogenic astrocytes from these mice showed activation not only of Egfr but also the RTK Axl in response to HBEGF stimulation. Deletion of either RTK decreased the tumorigenic properties of HBEGF transformed cells. Silencing of HBEGF *in vivo* resulted in significantly increased survival suggesting that HBEGF may be a clinically relevant target.

The work outlined in this dissertation investigates the role of mutant BRAF and activated HBEGF in the initiation and maintenance of gliomas using a somatic cell gene transfer mouse model. These findings suggest that these proteins may be therapeutic targets in gliomas and provide valuable insight for the improvement of treatment.

To Jeehyun and our little ones

TABLE OF CONTENTS

LIST OF TABLES

LIST OF FIGURES

ACKNOWLEDGEMENTS

Firstly, I would like to express my gratitude to my mentor, Dr. Sheri Holmen. With your guidance, I have grown both as an experimentalist and communicator. Through publishing, presenting at conferences, and successfully applying for a NIH F30, I have learned so much. Your dedication to your family and work is how I hope to model my future career.

I would also like to thank the members of my committee, Drs. Colman, Fults, VanBrocklin, and Varley. Thank you for your guidance and taking the time to meet with me to discuss my projects and career path.

I would also like to thank past and present members of the Holmen Lab, with a special thanks to James, who trained me when I first joined. Thank you Dee and Jess for keeping the Department of Oncological Sciences running smoothly. Thank you Drs. Stewart and Engel for your insights during journal club.

I would like to thank Drs. Dean Li and Jerry Kaplan for accepting me into the MD-PhD program and Drs. Gabrielle Kardon and Mary Hartnett for their continued support. Thank you Janet, our MD-PhD mom, for always looking out for me.

Lastly, I would like to express my deepest gratitude to my family for all their love and encouragement through all these years, especially my wife, Jeehyun, and my parents both in Los Angeles and in Seoul for their unconditional support. I love you all.

CHAPTER 1

INTRODUCTION

1.1 Glioma Statistics

Gliomas are the most common primary brain tumors in adults, with a yearly incidence of six cases per 100,000 or approximately 20,000 patients diagnosed annually in the United States (Ostrom et al., 2014a). There are many types of gliomas, with a wide range of incidences and clinical outcomes. Pilocytic astrocytoma, a benign tumor to which the pediatric population is predisposed, has an annual incidence of 0.93 per 100,000 and a 5-year survival rate of 94% (Ostrom et al., 2014b). In contrast, glioblastoma, a very aggressive tumor found mostly in older adults, has an annual incidence of 3.19 per 100,000 and a 5-year survival rate of 5% (Ostrom et al., 2014a). Malignant brain tumors account for 2.4% of all cancer deaths each year (Therese A. Dolecek, Jennifer M. Propp, 2012).

1.2 Glioma Classification

The World Health Organization (WHO) classification of gliomas is based solely on histological criteria and divided into four grades (Louis et al., 2007). Grades I and II are low-grade gliomas and Grades III and IV are high-grade gliomas. Grade I astrocytic tumors are pilocytic astrocytomas, which are slow-growing, circumscribed tumors detected in pediatric patients. Grade II tumors are diffusely infiltrative with cytological atypia. Grade

III gliomas show anaplasia and brisk mitotic activity and include the anaplastic astrocytomas and anaplastic oligodendrogliomas, while Grade IV gliomas are more commonly known as glioblastomas and are characterized by nuclear atypia, mitotic activity, cellular pleomorphism, vascular thrombosis, necrosis, and microvascular proliferation. Astrocytomas have prominent cytoplasmic processes and stain intensely with glial fibrillary acidic protein (GFAP), while oligodendrogliomas have small cytoplasm and round nuclei (Watanabe et al., 2002).

In the next update of the WHO classification due this year, molecular markers will serve as important complementary diagnostic criteria (Louis et al., 2016). About 30% of glioblastomas with the proneural signature have isocitrate dehydrogenase (*IDH1*) mutations, which is associated with the genome-wide glioma cytosine-phosphate-guanine methylator phenotype (G-CIMP) (Noushmehr et al., 2010; Verhaak et al., 2010). Gliomas with mutations in alpha thalassemia / mental retardation syndrome X-linked (*ATRX*) are found in anaplastic astrocytomas while mutations in telomerase reverse transcriptase (*TERT*) are found in anaplastic oligodendrogliomas (Arita et al., 2013; Jiao et al., 2012). Concomitant loss of chromosomes 1p and 19q is a marker for improved survival and is associated with oligodendrogliomas (Smith et al., 2000). With the detection of *IDH1* mutations in the majority of low-grade gliomas, three categories have emerged: those with *IDH1* mutations and 1p19q co-deletion (oligodendrogliomas), those with *IDH1* mutations and *p53* or *ATRX* mutations (astrocytomas), and those without *IDH* mutations (Balss et al., 2008; Yan et al., 2009). With the widespread use of next generation genomics and proteomics, more molecular markers will likely be discovered to aid in diagnosis and stratification of therapy.

1.3 Glioma Risk Factors

Close to 10% of patients have an inherited risk from genetic syndromes such as Li-Fraumeni syndrome (*p53* mutations), neurofibromatosis (*NF1* and *NF2* mutations), melanoma-astrocytoma syndrome (*CDKN2A* mutations), tuberous sclerosis (*TSC1* and *TSC2* mutations), and Cowden syndrome (*PTEN* mutations) (Goodenberger and Jenkins, 2012). The vast majority of gliomas arise from a combination of complex environmental factors and genetic predispositions (de Andrade et al., 2001). Ionizing radiation is the only known risk factor that increases the chance for the development of gliomas (Mathews et al., 2013; Sadetzki et al., 2005). Other factors that increase risk, such as pesticides and cell phone usage, have been implicated but not conclusively shown (Frei et al., 2011; Hardell et al., 2013; Provost et al., 2007; Yiin et al., 2012). Meanwhile studies have shown that patients with increased immunological activity due to allergic conditions have a reduced glioma risk (Calboli et al., 2011; Linos et al., 2007; Wigertz et al., 2007).

1.4 Clinical Presentation & Treatment of Glioma

Brain tumors are associated with acute symptoms such as seizures, headaches, nausea, and vomiting. Evaluation of a patient with a suspected tumor involves imaging with either a CT or MRI scan, although the gold standard is histological examination either from biopsy or surgical resection. In glioblastoma, the standard of care is fractionated localized radiation therapy totaling 60 Gy combined with temozolomide, a cytotoxic DNA-alkylating agent, following maximal surgical resection (Stupp et al., 2005). Favorable prognostic factors for malignant gliomas include younger age, extent of surgical resection, and high Karnofsky scores (Bauchet et al., 2010). Besides these clinical factors, molecular

characteristics of the tumors also inform prognosis. Patients with mutations in the promoter of O-6-methylguanine-DNA methyltransferase (MGMT), a DNA repair protein, show greater efficacy with temozolomide (Hegi et al., 2005). While efficacious in recurrent glioblastoma, use of the antivascular endothelial growth factor (VEGF) drug, bevacizumab, in newly diagnosed glioblastoma showed no further benefit over the standard treatment (Chinot et al., 2014; Friedman et al., 2009; Gilbert et al., 2014; Kreisl et al., 2009). Other treatments that have been tested but failed to show improvement over the temozolomide and radiotherapy regimen include combinations of carmustine wafers, EGFR inhibitors, PDGFR inhibitors, and PKC inhibitors (Van Den Bent et al., 2009; Raymond et al., 2008; Westphal et al., 2003; Wick et al., 2010). Thus the median survival for patients with glioblastoma is still about 14 months with the current standard of care, highlighting the need for new therapies.

For grade III gliomas, the presence of the 1p19q co-deletion, which usually defines the anaplastic oligodendrogliomas, dictates use of adjuvant radiation therapy and the chemotherapy regimen consisting of procarbazine, lomustine, and vincristine (PCV) (Cairncross et al., 1998; Ino et al., 2001). For patients without the 1p19q co-deletion, radiotherapy and temozolomide are usually indicated. Patients with grade III gliomas have median survivals on the order of years (3 for anaplastic astrocytoma and 15 for anaplastic oligodendroglioma).

Low-grade gliomas usually present in younger patients compared to high-grade gliomas. As these are slower growing tumors, focal neural deficits from mass effect are not seen and many of these tumors are found incidentally from an imaging study for an unrelated complaint. Unlike high-grade gliomas where surgery is always indicated, for a

patient with well-controlled seizures or no neurological deficits, it may be best to monitor rather than intervene. On the other hand, anaplastic gliomas can look like low-grade gliomas on MRI, and surgery allows for improved accuracy over needle biopsies in diagnosis, so intervention may be advantageous. Improved survival has been shown in patients with low-grade gliomas that underwent maximal safe resection (Jakola et al., 2012; McGirt et al., 2008).

1.5 Genetics of Glioblastoma

Characterizing tumors based on molecular markers has assumed a larger role recently, although challenges posed by tumor heterogeneity remain (Brennan et al., 2013; Parsons et al., 2008; Phillips et al., 2006; Verhaak et al., 2010). The Cancer Genome Atlas Network (TCGA) undertook a systematic approach to characterize glioblastomas based on analysis of several dimensions including DNA copy number, gene expression, and clinical treatment information. Alterations in three core pathways were revealed. Ninety percent have alterations in the receptor tyrosine kinase/RAS/phosphatidylinositol 3 kinase (RTK/RAS/PI3K) pathway with genetic alterations in phosphatase and tensin homolog deleted on chromosome 10 (*PTEN*), epidermal growth factor receptor (*EGFR*), and platelet-derived growth factor receptor alpha polypeptide (*PDGFRA*) most frequent. Eighty-six percent have alterations in p53-associated pathways, represented by mostly cyclin-dependent kinase inhibitor 2A (*CDKN2A*) deletion and mutations in *p53*. Seventy-nine percent have alterations in the retinoblastoma pathway, with alterations in *CDKN2A* and cyclin-dependent kinase 4 (*CDK4*) being the most common. Furthermore, transcriptomic subtyping of glioblastoma classified tumors within the proneural subtype,

mesenchymal subtype, and proliferative subtype, which is further classified into the neural and classical subtypes (Phillips et al., 2006; Verhaak et al., 2010). Clinically translating this wealth of knowledge is complicated because most of these genetic alterations, except for the RTKs, cannot be traditionally targeted with pharmacological agents, which focuses research on downstream effectors and alternate mutated pathways.

Mutations in the metabolic enzyme isocitrate dehydrogenase (*IDH*) have been found in more than 80% of grade II gliomas (diffuse astrocytomas), 70% of grade III gliomas (anaplastic astrocytomas and oligodendrogliomas), and 80% of secondary glioblastomas (Yan et al., 2009). *IDH1* mutations have not been found in grade I gliomas (pilocytic astrocytomas) and only in a small subset of primary glioblastomas (3%), although it is possible that some of these were misclassified as primary because their genetic profiles were found to be similar to secondary glioblastomas (Toedt et al., 2011). Primary glioblastomas do not arise from a known precursor lesion and occur in older, adult patients, while secondary glioblastomas derive from a less malignant tumor and tend to occur in younger patients; histologically they are indistinguishable. While the distinction between primary and secondary glioblastomas was observed almost 70 years ago, it was not fully appreciated until different genetic alterations were identified (Scherer, 1940). Distinctly, primary glioblastomas have *EGFR* amplification, *PTEN* mutations, *TERT* mutations and loss of chromosome 10 (Ekstrand et al., 1992; Fujisawa et al., 2000; Ohgaki et al., 2004; Tohma et al., 1998). Secondary glioblastomas are characterized by *IDH1* mutations, *p53* mutations, *ATRX* mutations, and 19q loss (Nakamura et al., 2000; Nobusawa et al., 2009; Watanabe et al., 1997).

1.6 BRAF in Glioma

About 88% of gliomas show alterations in the MAPK pathway. RAF is a MAPK kinase that consists of three family members: ARAF, BRAF, and CRAF. RAF serine-threonine kinases become activated when associated with RAS and in turn activate MEK1/2 and consequently ERK1/2. In adult gliomas, $BRAF^{V600E}$ mutations are found in about 5% of high-grade gliomas as well diffuse low-grade gliomas (Basto et al., 2005; Chi et al., 2013; Davies et al., 2002; Kleinschmidt-DeMasters et al., 2013). Gene fusions involving BRAF have been found in over 80% of pilocytic astrocytomas and follow the motif of an in-frame fusion of the C-terminal BRAF kinase domain with loss of the N-terminal autoinhibitory region (Cin et al., 2011). Surgery is usually curative for these low-grade gliomas, but some tumors are not amendable to resection due to location while others reoccur after resection. In these cases radiotherapy and chemotherapy are indicated although special attention to the long-term effects of treatment must be paid as many of these patients are from the pediatric population (Douw et al., 2009). Part of the allure for using targeted therapy would be to spare the patient from the side effects of conventional therapy. Unfortunately, these BRAF fusions lack the codon 600 mutation, making them resistant to mutant BRAF inhibitors (Jones et al., 2009; Sievert et al., 2013). In fact, BRAF codon 600 mutations in pilocytic astrocytomas are found in less than 6% of patients, but are found in the majority of pleomorphic xanthoastrocytomas (up to 65%) and gangliogliomas (up to 75%) (Dahiya et al., 2013; Dias-Santagata et al., 2011; Schiffman et al., 2010; Schindler et al., 2011). The sufficiency of the BRAF kinase domain to form low-grade gliomas is unknown.

1.7 HBEGF in Glioma

Aberrant activation of EGFR is seen in 45% of glioblastoma patients and is a hallmark of the classical subtype of glioblastoma (The Cancer Genome Atlas Network, 2008; Verhaak et al., 2010). Expression of EGFR and the deletion mutant EGFRvIII, which is a truncated mutant lacking exons 2 to 7, are detected in about 40% of malignant gliomas (Wikstrand et al., 1997). EGFRvIII acts synergistically with PTEN to transform neural precursor cells as well as confer resistance to EGFR inhibitors (Li et al., 2009). One of the main transcriptional targets of EGFRvIII is an EGFR ligand, heparin-binding epidermal growth factor-like growth factor (HBEGF) (Li et al., 2014). HBEGF has been shown to be co-expressed with EGFR by immunohistochemistry in up to 40% of malignant gliomas (Mishima et al., 1998; Ramnarain et al., 2006). While its mitogenic effects in normal astrocytes and human glioma cells have been characterized, transformation of astrocytes by HBEGF *in vitro* or *in vivo* remains to be elucidated (Puschmann et al., 2014; Ramnarain et al., 2006).

1.8 PDGFA in Glioma

PDGF autocrine stimulation is sufficient for the development of gliomas in mice (Uhrbom et al., 1998). PDGF signaling appears to be a crucial step to form oligodendrogliomas (Ozawa et al., 2014). Malignant gliomas express higher levels of PDGFRA, the receptor for PDGFA compared to lower grade gliomas or normal tissue (Takeuchi et al., 2004). Aberrations in the PDGFA signaling are considered a defining feature of the proneural subtype, which express oligodendrocytic development genes such as OLIG2 and NKX2-2 (Verhaak et al., 2010). Expression of PDGFA was found to be a

positive prognostic marker in malignant gliomas (Martinho et al., 2009). As IDH1 mutations have also been associated with the proneural subtype and better prognosis, there is likely overlap between PDGFA signaling and IDH1 mutations (Sturm et al., 2012). In fact, recently it was shown that IDH1 mutations can induce PDGFRA expression by relieving epigenetic suppression in the form of insulators (Flavahan et al., 2015).

1.9 Mouse Models of Glioma

Animal models for gliomas have proven important in the development of therapeutics. Retrospective studies on the efficacy of carmustine and temozolomide found that the animal models were able to predict the modest survival benefit for carmustine and the better response seen with temozolomide compared to nitrosoureas (Amarasingh et al., 2009; Hirst et al., 2013). There are two general types of mouse models – xenografts and genetically engineered models. Xenograft mouse models require the use of immune-deficient mice for transplantation of human glioma cells that are either well-established in culture or patient-derived. Examples include the U251 and U87 glioma models where the cancer cells are implanted either subcutaneously or orthotopically in the brain (Camphausen et al., 2005; Radaelli et al., 2009). While these tumors show striking resemblance to human glioblastoma from immunohistochemical analyses, the utility of these models is limited due to the user-dependent differences in cell culture *in vitro* as well as the differences in growth *in vivo* in the absence of an immune system. These drawbacks do not affect genetically engineered mouse models, of which there are two main types – those with germline modifications and those generated through somatic cell gene transfer.

One of the first glioma models using germline modification was created by using

the simian virus SV40 gene (Brinster et al., 1984). Microinjection of eggs with the viral gene caused random oncogenesis in the brain but also caused pathology in the kidneys and thymus. The first transgenic mouse model with brain specificity used the GFAP promoter to express the SV40 large T antigen to generate astrocytomas (Danks et al., 1995). Others have generated transgenic mouse models that are more clinically relevant using genetic lesions found in patients – such as NF1 loss and EGFRvIII expression. Using the GFAP promoter, expression of EGFRvIII was not sufficient to generate tumors and only with concurrent expression of HRas or loss of *Ink4a/Arf* and *Pten* were gliomas observed (Ding et al., 2003; Zhu et al., 2009). Loss of NF1, like loss of EGFRvIII, was not sufficient to form gliomas, but concurrent loss of p53 led to gliomagenesis (Reilly et al., 2000; Zhu et al., 2005).

Somatic cell gene transfer through the RCAS-TVA system addresses the main disadvantage of germline-modified transgenic models: the cost associated with developing a new strain of mice. With the RCAS-TVA model, oncogenes can be tested for sufficiency and necessity experiments by simply generating a new viral vector in a matter of days. Specific delivery of the oncogene is accomplished because of ectopic expression of the avian receptor TVA driven by a tissue-specific promoter such as Nestin or GFAP (Fisher et al., 1999). The RCAS-TVA glioma model has been used successfully with many putative and established oncogenes such as $Kras^{G12D}$, *PDGF-B*, and $BRAF^{V600E}$ (Dai et al., 2001; Holland et al., 2000; Robinson et al., 2010).

1.10 Preview

The work outlined in this dissertation investigates the role of BRAF and HBEGF in the initiation and maintenance of gliomas using an *in vivo* model. BRAF fusion genes have been identified in greater than 80% of pilocytic astrocytomas that result in loss of the BRAF N-terminal auto-inhibitory domain and constitutive activation of the BRAF C-terminal domain. While the importance of MAPK signaling in gliomas has been known for some time, the sufficiency of the BRAF kinase domain in the formation of gliomas *in vivo* remains an important question in the field. In Chapter 2, we show that the kinase domain of BRAF cooperates with *CDKN2A* loss to generate well-circumscribed, indolent gliomas in mice. We also demonstrate the efficacy of combined MEK and PI3K inhibition in astrocytes expressing the BRAF kinase domain.

HBEGF has been observed to be upregulated in a significant subset of malignant gliomas, and HBEGF expression correlates with decreased survival, but *in vitro* or *in vivo* transformation by HBEGF has not been assessed. In Chapter 3, we show that HBEGF-driven gliomas require loss of *PTEN* to generate malignant gliomas, while loss of *CDKN2A* led to initiation of low-grade gliomas. We uncovered a novel signaling pathway for HBEGF involving the receptor tyrosine kinase, *Axl*, and used transcriptome profiling to compare tumors driven by HBEGF, PDGFA, and $BRAF^{V600E}$ to the TCGA subtypes. We also demonstrate the feasibility of HBEGF as a clinical target using an *in vivo* tetracycline-regulated model.

After Chapter 4, supporting information involving HBEGF-, PDGFA-, and BRAF-driven gliomas that could not be added due to space limitations during the publication process of Chapters 2 and 3 are in the appendices. The appendices also contain other

unpublished data concerning our work to generate a tetracycline-responsive model for $BRAF^{V600E}$-driven glioblastoma.

1.11 References

Amarasingh, S., Macleod, M.R., and Whittle, I.R. (2009). What is the translational efficacy of chemotherapeutic drug research in neuro-oncology? A systematic review and meta-analysis of the efficacy of BCNU and CCNU in animal models of glioma. J. Neurooncol. *91*, 117–125.

de Andrade, M., Barnholtz, J.S., Amos, C.I., Adatto, P., Spencer, C., and Bondy, M.L. (2001). Segregation analysis of cancer in families of glioma patients. Genet. Epidemiol. *20*, 258–270.

Arita, H., Narita, Y., Fukushima, S., Tateishi, K., Matsushita, Y., Yoshida, A., Miyakita, Y., Ohno, M., Collins, V.P., Kawahara, N., et al. (2013). Upregulating mutations in the TERT promoter commonly occur in adult malignant gliomas and are strongly associated with total 1p19q loss. Acta Neuropathol. *126*, 267–276.

Balss, J., Meyer, J., Mueller, W., Korshunov, A., Hartmann, C., and von Deimling, A. (2008). Analysis of the IDH1 codon 132 mutation in brain tumors. Acta Neuropathol. *116*, 597–602.

Basto, D., Trovisco, V., Lopes, J.M., Martins, A., Pardal, F., Soares, P., and Reis, R.M. (2005). Mutation analysis of B-RAF gene in human gliomas. Acta Neuropathol. *109*, 207–210.

Bauchet, L., Mathieu-Daude, H., Fabbro-Peray, P., Rigau, V., Fabbro, M., Chinot, O., Pallusseau, L., Carnin, C., Laine, K., Schlama, A., et al. (2010). Oncological patterns of care and outcome for 952 patients with newly diagnosed glioblastoma in 2004. Neuro. Oncol. *12*, 725–735.

Van Den Bent, M.J., Brandes, A.A., Rampling, R., Kouwenhoven, M.C.M., Kros, J.M., Carpentier, A.F., Clement, P.M., Frenay, M., Campone, M., Baurain, J.F., et al. (2009). Randomized phase II trial of erlotinib versus temozolomide or carmustine in recurrent glioblastoma: EORTC brain tumor group study 26034. J. Clin. Oncol. *27*, 1268–1274.

Brennan, C.W., Verhaak, R.G.W., McKenna, A., Campos, B., Noushmehr, H., Salama, S.R., Zheng, S., Chakravarty, D., Sanborn, J.Z., Berman, S.H., et al. (2013). The somatic genomic landscape of glioblastoma. Cell *155*, 462–477.

Brinster, R.L., Chen, H.Y., Messing, A., van Dyke, T., Levine, A.J., and Palmiter, R.D. (1984). Transgenic mice harboring SV40 t-antigen genes develop characteristic brain

tumors. Cell *37*, 367–379.

Cairncross, J.G., Ueki, K., Zlatescu, M.C., Lisle, D.K., Finkelstein, D.M., Hammond, R.R., Silver, J.S., Stark, P.C., Macdonald, D.R., Ino, Y., et al. (1998). Specific genetic predictors of chemotherapeutic response and survival in patients with anaplastic oligodendrogliomas. J. Natl. Cancer Inst. *90*, 1473–1479.

Calboli, F.C.F., Cox, D.G., Buring, J.E., Gaziano, J.M., Ma, J., Stampfer, M., Willett, W.C., Tworoger, S.S., Hunter, D.J., Camargo, C.A., et al. (2011). Prediagnostic plasma IgE levels and risk of adult glioma in four prospective cohort studies. J. Natl. Cancer Inst. *103*, 1588–1595.

Camphausen, K., Purow, B., Sproull, M., Scott, T., Ozawa, T., Deen, D.F., and Tofilon, P.J. (2005). Orthotopic growth of human glioma cells quantitatively and qualitatively influences radiation-induced changes in gene expression. Cancer Res. *65*, 10389–10393.

Chi, A.S., Batchelor, T.T., Yang, D., Dias-Santagata, D., Borger, D.R., Ellisen, L.W., Iafrate, A.J., and Louis, D.N. (2013). BRAF V600E mutation identifies a subset of low-grade diffusely infiltrating gliomas in adults. J. Clin. Oncol. *31*, e233–e236.

Chinot, O.L., Wick, W., Mason, W., Henriksson, R., Saran, F., Nishikawa, R., Carpentier, A.F., Hoang-Xuan, K., Kavan, P., Cernea, D., et al. (2014). Bevacizumab plus radiotherapy-temozolomide for newly diagnosed glioblastoma. N. Engl. J. Med. *370*, 709–722.

Cin, H., Meyer, C., Herr, R., Janzarik, W.G., Lambert, S., Jones, D.T.W., Jacob, K., Benner, A., Witt, H., Remke, M., et al. (2011). Oncogenic FAM131B-BRAF fusion resulting from 7q34 deletion comprises an alternative mechanism of MAPK pathway activation in pilocytic astrocytoma. Acta Neuropathol. *121*, 763–774.

Dahiya, S., Haydon, D.H., Alvarado, D., Gurnett, C.A., Gutmann, D.H., and Leonard, J.R. (2013). BRAF(V600E) mutation is a negative prognosticator in pediatric ganglioglioma. Acta Neuropathol. *125*, 901–910.

Dai, C., Celestino, J.C., Okada, Y., Louis, D.N., Fuller, G.N., and Holland, E.C. (2001). PDGF autocrine stimulation dedifferentiates cultured astrocytes and induces oligodendrogliomas from and oligoastrocytomas neural progenitors and astrocytes in vivo. Genes Dev. *15*, 1913–1925.

Danks, R. A, Orian, J.M., Gonzales, M.F., Tan, S.-S., Alexander, B., Mikoshiba, K., and Kaye, a H. (1995). Transformation of astrocytes in transgenic mice expressing {SV40} T antigen ander the transcriptional control of the glial acidic protein promoter. Cancer Res. *55*, 4302–4310.

Davies, H., Bignell, G.R., Cox, C., Stephens, P., Edkins, S., Clegg, S., Teague, J., Woffendin, H., Garnett, M.J., Bottomley, W., et al. (2002). Mutations of the BRAF gene

in human cancer. Nature *417*, 949–954.

Dias-Santagata, D., Lam, Q., Vernovsky, K., Vena, N., Lennerz, J.K., Borger, D.R., Batchelor, T.T., Ligon, K.L., Iafrate, A.J., Ligon, A.H., et al. (2011). Braf V600E mutations are common in pleomorphic xanthoastrocytoma: Diagnostic and therapeutic implications. PLoS One *6*.

Ding, H., Shannon, P., Lau, N., Wu, X., Roncari, L., Baldwin, R.L., Takebayashi, H., Nagy, A., Gutmann, D.H., and Guha, A. (2003). Oligodendrogliomas result from the expression of an activated mutant epidermal growth factor receptor in a RAS transgenic mouse astrocytoma model. Cancer Res. *63*, 1106–1113.

Douw, L., Klein, M., Fagel, S.S., van den Heuvel, J., Taphoorn, M.J., Aaronson, N.K., Postma, T.J., Vandertop, W.P., Mooij, J.J., Boerman, R.H., et al. (2009). Cognitive and radiological effects of radiotherapy in patients with low-grade glioma: long-term follow-up. Lancet Neurol. *8*, 810–818.

Ekstrand, A.J., Sugawa, N., James, C.D., and Collins, V.P. (1992). Amplified and rearranged epidermal growth factor receptor genes in human glioblastomas reveal deletions of sequences encoding portions of the N- and/or C-terminal tails. Proc. Natl. Acad. Sci. U. S. A. *89*, 4309–4313.

Fisher, G.H., Orsulic, S., Holland, E., Hively, W.P., Li, Y., Lewis, B.C., Williams, B.O., and Varmus, H.E. (1999). Development of a flexible and specific gene delivery system for production of murine tumor models. Oncogene *18*, 5253–5260.

Flavahan, W.A., Drier, Y., Liau, B.B., Gillespie, S.M., Venteicher, A.S., Stemmer-Rachamimov, A.O., Suvà, M.L., and Bernstein, B.E. (2015). Insulator dysfunction and oncogene activation in IDH mutant gliomas. Nature *529*, 110–114.

Frei, P., Poulsen, A.H., Johansen, C., Olsen, J.H., Steding-Jessen, M., and Schüz, J. (2011). Use of mobile phones and risk of brain tumours: update of Danish cohort study. BMJ *343*, d6387.

Friedman, H.S., Prados, M.D., Wen, P.Y., Mikkelsen, T., Schiff, D., Abrey, L.E., Yung, W.K.A., Paleologos, N., Nicholas, M.K., Jensen, R., et al. (2009). Bevacizumab alone and in combination with irinotecan in recurrent glioblastoma. J. Clin. Oncol. *27*, 4733–4740.

Fujisawa, H., Reis, R.M., Nakamura, M., Colella, S., Yonekawa, Y., Kleihues, P., and Ohgaki, H. (2000). Loss of heterozygosity on chromosome 10 is more extensive in primary (de novo) than in secondary glioblastomas. Lab. Invest. *80*, 65–72.

Gilbert, M.R., Dignam, J.J., Armstrong, T.S., Wefel, J.S., Blumenthal, D.T., Vogelbaum, M.A., Colman, H., Chakravarti, A., Pugh, S., Won, M., et al. (2014). A randomized trial of bevacizumab for newly diagnosed glioblastoma. N. Engl. J. Med. *370*, 699–708.

Goodenberger, M.L., and Jenkins, R.B. (2012). Genetics of adult glioma. Cancer Genet. *205*, 613–621.

Hardell, L., Carlberg, M., Söderqvist, F., and Mild, K.H. (2013). Pooled analysis of case-control studies on acoustic neuroma diagnosed 1997-2003 and 2007-2009 and use of mobile and cordless phones. Int. J. Oncol. *43*, 1036–1044.

Hegi, M.E., Diserens, A.-C., Gorlia, T., Hamou, M.-F., de Tribolet, N., Weller, M., Kros, J.M., Hainfellner, J. a, Mason, W., Mariani, L., et al. (2005). MGMT gene silencing and benefit from temozolomide in glioblastoma. N. Engl. J. Med. *352*, 997–1003.

Hirst, T.C., Vesterinen, H.M., Sena, E.S., Egan, K.J., Macleod, M.R., and Whittle, I.R. (2013). Systematic review and meta-analysis of temozolomide in animal models of glioma: was clinical efficacy predicted? Br. J. Cancer *108*, 64–71.

Holland, E.C., Celestino, J., Dai, C., Schaefer, L., Sawaya, R.E., and Fuller, G.N. (2000). Combined activation of Ras and Akt in neural progenitors induces glioblastoma formation in mice. Nat. Genet. *25*, 55–57.

Ino, Y., Betensky, R.A., Zlatescu, M.C., Sasaki, H., Macdonald, D.R., Stemmer-Rachamimov, A.O., Ramsay, D.A., Cairncross, J.G., and Louis, D.N. (2001). Molecular subtypes of anaplastic oligodendroglioma: implications for patient management at diagnosis. Clin. Cancer Res. *7*, 839–845.

Jakola, A.S., Myrmel, K.S., Kloster, R., Torp, S.H., Lindal, S., Unsgård, G., and Solheim, O. (2012). Comparison of a strategy favoring early surgical resection vs a strategy favoring watchful waiting in low-grade gliomas. JAMA *308*, 1881–1888.

Jiao, Y., Killela, P.J., Reitman, Z.J., Rasheed, A.B., Heaphy, C.M., de Wilde, R.F., Rodriguez, F.J., Rosemberg, S., Oba-Shinjo, S.M., Nagahashi Marie, S.K., et al. (2012). Frequent ATRX, CIC, FUBP1 and IDH1 mutations refine the classification of malignant gliomas. Oncotarget *3*, 709–722.

Jones, D.T.W., Kocialkowski, S., Liu, L., Pearson, D.M., Ichimura, K., and Collins, V.P. (2009). Oncogenic RAF1 rearrangement and a novel BRAF mutation as alternatives to KIAA1549:BRAF fusion in activating the MAPK pathway in pilocytic astrocytoma. Oncogene *28*, 2119–2123.

Kleinschmidt-DeMasters, B.K., Aisner, D.L., Birks, D.K., and Foreman, N.K. (2013). Epithelioid GBMs show a high percentage of BRAF V600E mutation. Am. J. Surg. Pathol. *37*, 685–698.

Kreisl, T.N., Kim, L., Moore, K., Duic, P., Royce, C., Stroud, I., Garren, N., Mackey, M., Butman, J.A., Camphausen, K., et al. (2009). Phase II trial of single-agent bevacizumab followed by bevacizumab plus irinotecan at tumor progression in recurrent glioblastoma. J. Clin. Oncol. *27*, 740–745.

Li, L., Dutra, A., Pak, E., Labrie, J.E., Gerstein, R.M., Pandolfi, P.P., Recht, L.D., and Ross, A.H. (2009). EGFRvIII expression and PTEN loss synergistically induce chromosomal instability and glial tumors. Neuro. Oncol. *11*, 9–21.

Li, L., Chakraborty, S., Yang, C.-R., Hatanpaa, K.J., Cipher, D.J., Puliyappadamba, V.T., Rehman, a, Jiwani, a J., Mickey, B., Madden, C., et al. (2014). An EGFR wild type-EGFRvIII-HB-EGF feed-forward loop regulates the activation of EGFRvIII. Oncogene *33*, 4253–4264.

Linos, E., Raine, T., Alonso, A., and Michaud, D. (2007). Atopy and risk of brain tumors: A meta-analysis. J. Natl. Cancer Inst. *99*, 1544–1550.

Louis, D.N., Ohgaki, H., Wiestler, O.D., Cavenee, W.K., Burger, P.C., Jouvet, A., Scheithauer, B.W., and Kleihues, P. (2007). The 2007 WHO classification of tumours of the central nervous system. Acta Neuropathol. *114*, 97–109.

Louis, D.N., Perry, A., Reifenberger, G., von Deimling, A., Figarella-Branger, D., Cavenee, W.K., Ohgaki, H., Wiestler, O.D., Kleihues, P., and Ellison, D.W. (2016). The 2016 World Health Organization Classification of Tumors of the Central Nervous System: a summary. Acta Neuropathol. *131*, 803–820.

Martinho, O., Longatto-Filho, A., Lambros, M.B.K., Martins, A., Pinheiro, C., Silva, A., Pardal, F., Amorim, J., Mackay, A., Milanezi, F., et al. (2009). Expression, mutation and copy number analysis of platelet-derived growth factor receptor A (PDGFRA) and its ligand PDGFA in gliomas. Br. J. Cancer *101*, 973–982.

Mathews, J.D., Forsythe, A. V, Brady, Z., Butler, M.W., Goergen, S.K., Byrnes, G.B., Giles, G.G., Wallace, A.B., Anderson, P.R., Guiver, T.A., et al. (2013). Cancer risk in 680,000 people exposed to computed tomography scans in childhood or adolescence: data linkage study of 11 million Australians. BMJ *346*, f2360.

McGirt, M.J., Chaichana, K.L., Attenello, F.J., Weingart, J.D., Than, K., Burger, P.C., Olivi, A., Brem, H., and Quinoñes-Hinojosa, A. (2008). Extent of surgical resection is independently associated with survival in patients with hemispheric infiltrating low-grade gliomas. Neurosurgery *63*, 700–707; author reply 707–708.

Mishima, K., Higashiyama, S., Asai, A., Yamaoka, K., Nagashima, Y., Taniguchi, N., Kitanaka, C., Kirino, T., and Kuchino, Y. (1998). Heparin-binding epidermal growth factor-like growth factor stimulates mitogenic signaling and is highly expressed in human malignant gliomas. Acta Neuropathol. *96*, 322–328.

Nakamura, M., Yang, F., Fujisawa, H., Yonekawa, Y., Kleihues, P., and Ohgaki, H. (2000). Loss of heterozygosity on chromosome 19 in secondary glioblastomas. J. Neuropathol. Exp. Neurol. *59*, 539–543.

Nobusawa, S., Watanabe, T., Kleihues, P., and Ohgaki, H. (2009). IDH1 mutations as

molecular signature and predictive factor of secondary glioblastomas. Clin. Cancer Res. *15*, 6002–6007.

Noushmehr, H., Weisenberger, D.J., Diefes, K., Phillips, H.S., Pujara, K., Berman, B.P., Pan, F., Pelloski, C.E., Sulman, E.P., Bhat, K.P., et al. (2010). Identification of a CpG Island Methylator Phenotype that Defines a Distinct Subgroup of Glioma. Cancer Cell *17*, 510–522.

Ohgaki, H., Dessen, P., Jourde, B., Horstmann, S., Nishikawa, T., Di Patre, P.L., Burkhard, C., Sch+-ler, D., Probst-Hensch, N., Maiorka, P., et al. (2004). Genetic pathways to glioblastoma: a population-based study. Cancer Res. *64*, 6892–6899.

Ostrom, Q.T., Gittleman, H., Liao, P., Rouse, C., Chen, Y., Dowling, J., Wolinsky, Y., Kruchko, C., and Barnholtz-Sloan, J. (2014a). CBTRUS Statistical Report: Primary Brain and Central Nervous System Tumors Diagnosed in the United States in 2007-2011. Neuro. Oncol. *16 Suppl 4*, iv1–iv63.

Ostrom, Q.T., de Blank, P.M., Kruchko, C., Petersen, C.M., Liao, P., Finlay, J.L., Stearns, D.S., Wolff, J.E., Wolinsky, Y., Letterio, J.J., et al. (2014b). Alex's Lemonade Stand Foundation Infant and Childhood Primary Brain and Central Nervous System Tumors Diagnosed in the United States in 2007-2011. Neuro. Oncol. *16*, x1–x36.

Ozawa, T., Riester, M., Cheng, Y.K., Huse, J., Squatrito, M., Helmy, K., Charles, N., Michor, F., and Holland, E.C. (2014). Most human non-GCIMP glioblastoma subtypes evolve from a common proneural-like precursor glioma. Cancer Cell *26*, 288–300.

Parsons, D.W., Jones, S., Zhang, X., Lin, J.C., Leary, R.J., Angenendt, P., Mankoo, P., Carter, H., Siu, I., Gallia, G.L., et al. (2008). An integrated genomic analysis of human glioblastoma multiforme. Science *321*, 1807–1812.

Phillips, H.S., Kharbanda, S., Chen, R., Forrest, W.F., Soriano, R.H., Wu, T.D., Misra, A., Nigro, J.M., Colman, H., Soroceanu, L., et al. (2006). Molecular subclasses of high-grade glioma predict prognosis, delineate a pattern of disease progression, and resemble stages in neurogenesis. Cancer Cell *9*, 157–173.

Provost, D., Cantagrel, A., Lebailly, P., Jaffré, A., Loyant, V., Loiseau, H., Vital, A., Brochard, P., and Baldi, I. (2007). Brain tumours and exposure to pesticides: a case-control study in southwestern France. Occup. Environ. Med. *64*, 509–514.

Puschmann, T.B., Zandén, C., Lebkuechner, I., Philippot, C., De Pablo, Y., Liu, J., and Pekny, M. (2014). HB-EGF affects astrocyte morphology, proliferation, differentiation, and the expression of intermediate filament proteins. J. Neurochem. *128*, 878–889.

Radaelli, E., Ceruti, R., Patton, V., Russo, M., Degrassi, A., Croci, V., Caprera, F., Stortini, G., Scanziani, E., Pesenti, E., et al. (2009). Immunohistopathological and neuroimaging characterization of murine orthotopic xenograft models of glioblastoma multiforme

recapitulating the most salient features of human disease. Histol. Histopathol. *24*, 879–891.

Ramnarain, D.B., Park, S., Lee, D.Y., Hatanpaa, K.J., Scoggin, S.O., Otu, H., Libermann, T. a, Raisanen, J.M., Ashfaq, R., Wong, E.T., et al. (2006). Differential gene expression analysis reveals generation of an autocrine loop by a mutant epidermal growth factor receptor in glioma cells. Cancer Res. *66*, 867–874.

Raymond, E., Brandes, A.A., Dittrich, C., Fumoleau, P., Coudert, B., Clement, P.M.J., Frenay, M., Rampling, R., Stupp, R., Kros, J.M., et al. (2008). Phase II study of imatinib in patients with recurrent gliomas of various histologies: A European organisation for research and treatment of cancer brain tumor group study. J. Clin. Oncol. *26*, 4659–4665.

Reilly, K.M., Loisel, D. a, Bronson, R.T., McLaughlin, M.E., and Jacks, T. (2000). Nf1;Trp53 mutant mice develop glioblastoma with evidence of strain-specific effects. Nat. Genet. *26*, 109–113.

Robinson, J.P., VanBrocklin, M.W., Guilbeault, a R., Signorelli, D.L., Brandner, S., and Holmen, S.L. (2010). Activated BRAF induces gliomas in mice when combined with Ink4a/Arf loss or Akt activation. Oncogene *29*, 335–344.

Sadetzki, S., Chetrit, A., Freedman, L., Stovall, M., Modan, B., and Novikov, I. (2005). Long-term follow-up for brain tumor development after childhood exposure to ionizing radiation for tinea capitis. Radiat. Res. *163*, 424–432.

Scherer, H.J. (1940). Cerebral Astrocytomas and Their Derivatives. Am. J. Cancer *40*, 159–198.

Schiffman, J.D., Hodgson, J.G., VandenBerg, S.R., Flaherty, P., Polley, M.-Y.C., Yu, M., Fisher, P.G., Rowitch, D.H., Ford, J.M., Berger, M.S., et al. (2010). Oncogenic BRAF mutation with CDKN2A inactivation is characteristic of a subset of pediatric malignant astrocytomas. Cancer Res. *70*, 512–519.

Schindler, G., Capper, D., Meyer, J., Janzarik, W., Omran, H., Herold-Mende, C., Schmieder, K., Wesseling, P., Mawrin, C., Hasselblatt, M., et al. (2011). Analysis of BRAF V600E mutation in 1,320 nervous system tumors reveals high mutation frequencies in pleomorphic xanthoastrocytoma, ganglioglioma and extra-cerebellar pilocytic astrocytoma. Acta Neuropathol. *121*, 397–405.

Sievert, A.J., Lang, S., Katie, L., Madsen, P.J., Slaunwhite, E., Choudhari, N., Kellet, M., Storm, P.B., Resnick, A.C., Kjetland, E.F., et al. (2013). Paradoxical activation and RAF inhibitor resistance of BRAF protein kinase fusions characterizing pediatric astrocytomas. Proc. Natl. Acad. Sci. *110*, 8750–8750.

Smith, J.S., Perry, A., Borell, T.J., Lee, H.K., O'Fallon, J., Hosek, S.M., Kimmel, D., Yates, A., Burger, P.C., Scheithauer, B.W., et al. (2000). Alterations of chromosome arms 1p and 19q as predictors of survival in oligodendrogliomas, astrocytomas, and mixed

oligoastrocytomas. J. Clin. Oncol. *18*, 636–645.

Stupp, R., Mason, W.P., van den Bent, M.J., Weller, M., Fisher, B., Taphoorn, M.J.B., Belanger, K., Brandes, A. a, Marosi, C., Bogdahn, U., et al. (2005). Radiotherapy plus concomitant and adjuvant temozolomide for glioblastoma. N. Engl. J. Med. *352*, 987–996.

Sturm, D., Witt, H., Hovestadt, V., Khuong-Quang, D.A., Jones, D.T.W., Konermann, C., Pfaff, E., T??njes, M., Sill, M., Bender, S., et al. (2012). Hotspot Mutations in H3F3A and IDH1 Define Distinct Epigenetic and Biological Subgroups of Glioblastoma. Cancer Cell *22*, 425–437.

Takeuchi, H., Kanzawa, T., Kondo, Y., and Kondo, S. (2004). Inhibition of platelet-derived growth factor signalling induces autophagy in malignant glioma cells. Br. J. Cancer *90*, 1069–1075.

The Cancer Genome Atlas Network (2008). Comprehensive genomic characterization defines human glioblastoma genes and core pathways. Nature *455*, 1061–1068.

Therese A. Dolecek, Jennifer M. Propp, N.E.S. and C.K. (2012). CBTRUS Statistical Report: Primary Brain and Central Nervous System Tumors Diagnosed in the United States in 2005–2009. Neuro. Oncol. *14(suppl 5*, 1–57.

Toedt, G., Barbus, S., Wolter, M., Felsberg, J., Tews, B., Blond, F., Sabel, M.C., Hofmann, S., Becker, N., Hartmann, C., et al. (2011). Molecular signatures classify astrocytic gliomas by IDH1 mutation status. Int. J. Cancer *128*, 1095–1103.

Tohma, Y., Gratas, C., Biernat, W., Peraud, A., Fukuda, M., Yonekawa, Y., Kleihues, P., and Ohgaki, H. (1998). PTEN (MMAC1) mutations are frequent in primary glioblastomas (de novo) but not in secondary glioblastomas. J. Neuropathol. Exp. Neurol. *57*, 684–689.

Uhrbom, L., Hesselager, G., Nistér, M., and Westermark, B. (1998). Induction of brain tumors in mice using a recombinant platelet-derived growth factor B-chain retrovirus. Cancer Res. *58*, 5275–5279.

Verhaak, R.G.W., Hoadley, K. A., Purdom, E., Wang, V., Qi, Y., Wilkerson, M.D., Miller, C.R., Ding, L., Golub, T., Mesirov, J.P., et al. (2010). Integrated genomic analysis identifies clinically relevant subtypes of glioblastoma characterized by abnormalities in PDGFRA, IDH1, EGFR, and NF1. Cancer Cell *17*, 98–110.

Watanabe, K., Sato, K., Biernat, W., Tachibana, O., von Ammon, K., Ogata, N., Yonekawa, Y., Kleihues, P., and Ohgaki, H. (1997). Incidence and timing of p53 mutations during astrocytoma progression in patients with multiple biopsies. Clin. Cancer Res. *3*, 523–530.

Watanabe, T., Nakamura, M., Kros, J.M., Burkhard, C., Yonekawa, Y., Kleihues, P., and Ohgaki, H. (2002). Phenotype versus genotype correlation in oligodendrogliomas and low-

grade diffuse astrocytomas. Acta Neuropathol. *103*, 267–275.

Westphal, M., Hilt, D.C., Bortey, E., Delavault, P., Olivares, R., Warnke, P.C., Whittle, I.R., Jääskeläinen, J., and Ram, Z. (2003). A phase 3 trial of local chemotherapy with biodegradable carmustine (BCNU) wafers (Gliadel wafers) in patients with primary malignant glioma. Neuro. Oncol. *5*, 79–88.

Wick, W., Puduvalli, V.K., Chamberlain, M.C., Van Den Bent, M.J., Carpentier, A.F., Cher, L.M., Mason, W., Weller, M., Hong, S., Musib, L., et al. (2010). Phase III study of enzastaurin compared with lomustine in the treatment of recurrent intracranial glioblastoma. J. Clin. Oncol. *28*, 1168–1174.

Wigertz, A., Lönn, S., Schwartzbaum, J., Hall, P., Auvinen, A., Christensen, H.C., Johansen, C., Klæboe, L., Salminen, T., Schoemaker, M.J., et al. (2007). Allergic conditions and brain tumor risk. Am. J. Epidemiol. *166*, 941–950.

Wikstrand, C.J., McLendon, R.E., Friedman, A.H., and Bigner, D.D. (1997). Cell surface localization and density of the tumor-associated variant of the epidermal growth factor receptor, EGFRvIII. Cancer Res. *57*, 4130–4140.

Yan, H., Parsons, D.W., Jin, G., McLendon, R., Rasheed, B.A., Yuan, W., Kos, I., Batinic-Haberle, I., Jones, S., Riggins, G.J., et al. (2009). IDH1 and IDH2 mutations in gliomas. N. Engl. J. Med. *360*, 765–773.

Yiin, J.H., Ruder, A.M., Stewart, P.A., Waters, M.A., Carreón, T., Butler, M.A., Calvert, G.M., Davis-King, K.E., Schulte, P.A., Mandel, J.S., et al. (2012). The Upper Midwest Health Study: a case-control study of pesticide applicators and risk of glioma. Environ. Health *11*, 39.

Zhu, H., Acquaviva, J., Ramachandran, P., Boskovitz, A., Woolfenden, S., Pfannl, R., Bronson, R.T., Chen, J.W., Weissleder, R., Housman, D.E., et al. (2009). Oncogenic EGFR signaling cooperates with loss of tumor suppressor gene functions in gliomagenesis. Proc. Natl. Acad. Sci. U. S. A. *106*, 2712–2716.

Zhu, Y., Guignard, F., Zhao, D., Liu, L., Burns, D.K., Mason, R.P., Messing, A., and Parada, L.F. (2005). Early inactivation of p53 tumor suppressor gene cooperating with NF1 loss induces malignant astrocytoma. Cancer Cell *8*, 119–130.

CHAPTER 2

THE BRAF KINASE DOMAIN PROMOTES THE DEVELOPMENT OF GLIOMAS IN VIVO

2.1 Preface

This chapter is a reformatted version of a manuscript published in *Genes & Cancer* in January 2015. The work presented herein was completed with the following coauthors: Allie H. Grossmann, Sheri L. Holmen, and James P. Robinson. Reprinted with permission from Impact Journals, LLC.

2.2 Introduction

Aberrant RAS mitogen activated protein kinase (MAPK pathway) activation is a hallmark of gliomas (Abounader, 2009). Activation of this pathway occurs through mutations or amplifications in receptor tyrosine kinases or downstream signaling mediators such as RAS, RAF, MEK, and ERK (Kondo et al., 2004). Recently, a novel mechanism involving *RAF* fusion genes has been identified in pilocytic astrocytomas (PA) that allows for MAPK activation. In-frame fusions between *FAM131B* and *BRAF* have been observed in 2% of sporadic PA (Cin et al., 2011), fusions between *SRGAP3* and *RAF1* have also been found in 2% of sporadic PA (Jones et al., 2009), and fusions between *KIAA1549* and *BRAF* have been identified in nearly 80% of sporadic PA samples tested (Forshew et al.,

2009; Jones et al., 2008; Sievert et al., 2009). The majority (>70%) of the *KIAA1549:BRAF* fusions occur between exon 16 of *KIAA1549* and exon 9 of *BRAF,* but multiple different fusions have been identified (Cin et al., 2011; Tatevossian et al., 2010a). The presence of a BRAF fusion gene is now considered highly diagnostic for PA (Lawson et al., 2010). These fusions cause anchorage-independent growth when overexpressed in NIH3T3 cells (Jones et al., 2008, 2009) and cerebellar neural stem cell (NSC) cultures (Kaul et al., 2012). Cerebellar engraftment of NSCs expressing *KIAA1549:BRAF* in mice led to the formation of glioma-like lesions after a latency of 6 months (Kaul et al., 2012).

In each fusion the N-terminus of RAF is replaced by FAM131B, SRGAP3 or KIAA1549, resulting in loss of the N-terminal autoinhibitory domain of RAF and constitutive activation of the MAPK pathway via the retained C-terminal kinase domain (BRAF-KD) (Figure 2.1). The specificity with which the C-terminus of RAF fuses to these different genes suggests that it is required for tumorigenesis in this context; however, the role of the C-terminal domain of *BRAF* within the fusions in glioma formation has not been validated. Expression of a BRAF kinase domain mutant carrying the V600E alteration (BRAF-KD^{VE}) was sufficient to induce PA-like lesions in mice (Gronych et al., 2011). However, in patients, the BRAF kinase domain has not been found to be mutated in this manner in the context of a fusion gene. V600E mutations in full length BRAF are seen in a small percentage of PA (6%) (Chin et al., 1998; Lawson et al., 2010; Schiffman et al., 2010; Zhang et al., 2013); however, they are much more common in grade II, and high-grade malignant pediatric gliomas, accounting for 18% of grade II, 33% of grade III, and 18% of grade IV tumors (23% grades II-IV) (Roussel, 1999). We have previously demonstrated that *BRAF^{V600E}* can cooperate with *Ink4a/Arf* loss to induce high-grade

gliomas in mice (Robinson et al., 2010).

The development of small molecule serine-threonine kinase inhibitors (vemurafenib and dabrafenib) that specifically target mutant BRAF has revolutionized the treatment of melanoma, and clinical trials are underway for treatment of pediatric gliomas carrying the $BRAF^{V600E}$ mutation (NCT01748149, NCT02034110). However, paradoxically these inhibitors activate MAPK signaling in tumors that do not carry codon 600 mutations, and new small molecule inhibitors designed to break this paradox do not inhibit BRAF fusion mutants at physiologically relevant doses (Sievert et al., 2013). Furthermore, mutations causing the truncation and loss of the BRAF autoregulatory domain are known to drive resistance to small molecule inhibitors that target the oncogenic codon 600 mutations (Kaul et al., 2012).

In addition to constitutive MAPK activity, mutations targeting the p53/Rb cell cycle pathways are also seen in gliomas. In PA, loss of p16 correlates strongly with reduced senescence, increased cell division, and tumor progression (Kaul et al., 2012; Tatevossian et al., 2010b). Higher grade pediatric gliomas demonstrate constitutive MAPK activity, but this is almost always accompanied by homozygous deletion of the *cyclin-dependent kinase inhibitor 2A* (*CDKN2A*) locus (Schiffman et al., 2010). This locus encodes both p16 (INK4a) and p14 (ARF) (Chin et al., 1998; Roussel, 1999). p16 functions to inhibit CDK4/6 mediated phosphorylation of the Retinoblastoma (Rb) protein, and its loss allows for unregulated cell division (Quelle et al., 1995). Loss of p14 leads to increased ubiquitination and destruction of p53 by HDM2 (Ivanchuk et al., 2008). Interestingly, 38.5% of PAs show loss of heterozygosity at 9q21, the location of the *CDKN2A* locus and homozygous deletion is seen in 6.4% of cases (Horbinski et al., 2010).

A follow-up study of PA patients receiving adjuvant therapy after surgery also found 14% of cases had both p16 loss and BRAF rearrangements (Horbinski et al., 2012).

In the current study, we used the well-established RCAS/TVA glioma mouse model to assess the role of the BRAF-KD in glioma development *in vivo*. We show that although the BRAF-KD is not tumorigenic on its own, cooperation with *Ink4a/Arf* loss leads to the development of relatively indolent but highly atypical and cellular gliomas *in vivo.*

2.3 Results

2.3.1 The BRAF kinase domain promotes anchorage-independent growth. We previously demonstrated the transformative capacity of N-TVA/*Ink4a*/*Arf*$^{-/-}$ astrocytes infected with RCASBP(A) viruses containing CRAF$^{\Delta 22W}$, BRAF^{V600E} or KRAS^{G12D}, which form numerous colonies in soft agar (Robinson et al., 2010). To assess the transforming potential of the BRAF kinase domain BRAF-KD, we infected N-TVA/*Ink4a*/*Arf*$^{-/-}$ astrocytes with RCASBP(A)BRAF-KD and the full length *BRAF* with the V600E mutation, RCASBP(A)BRAF^{V600E} (hereafter BRAF-FL^{VE}). Gene delivery and expression was confirmed by immunoblotting (Figure 2.2A). Analysis of phosphorylated Erk 1/2 (P-Erk) demonstrated elevated MAPK activation in cells expressing BRAF-KD (Figure 2.2B). *Ink4a/Arf*-deficient astrocytes expressing BRAF-KD or BRAF-FL^{VE} proliferated more rapidly than the negative control; however, there was no significant difference between proliferation of BRAF-KD or BRAF-FL^{VE} cells (P = 0.29; Figure 2.2C). Whereas *Ink4a/Arf*-deficient astrocytes did not form colonies in soft agar, expression of BRAF-KD or our positive control BRAF-FL^{VE}, induced colonies demonstrating their ability to transform cells in the context of altered Rb and/or p53 signaling (Figure 2.2D).

Interestingly, there was a statistically significant difference between the number of colonies formed by BRAF-KD and BRAF-FL^{VE} expression ($P = 0.04$).

2.3.2 The BRAF-kinase domain promotes transformation and tumor growth in vivo. A more stringent assay of tumorigenic potential is the ability to form tumors *in vivo*. The cell lines used for these orthotopic studies are syngeneic with the immunocompetent host mouse strain. Therefore, to assess tumorigenicity *in vivo*, 2 x 10^4 astrocytes were delivered intracranially to newborn mice, and the mice were monitored for signs of tumor formation. *Ink4a/Arf*-deficient astrocytes expressing mutant KRAS served as a positive control. Tumors formed within 3 weeks in 100% of mice injected with *Ink4a/Arf*-deficient astrocytes expressing KRAS^{G12D} (8 / 8) or the BRAF-KD (8 / 8). No tumors formed following the injection of uninfected astrocytes within this time frame. Histologically, the BRAF-KD tumors resembled highly cellular and invasive gliomas; both possessed a diffuse growth pattern but lacked the necrosis and endothelial hyperplasia typical of grade IV tumors, glioblastoma multiforme (GBM) (Figure 2.3). Expression of the BRAF-KD was confirmed using IHC for the HA epitope Tag (Figure 2.3). MAPK pathway activation within the tumors was assessed using IHC for P-Erk (Figure 2.3). All the tumors expressed the glial progenitor marker Nestin; however, expression of the glial fibrillary acidic protein (GFAP) was absent (Figure 2.3).

2.3.3 Expression of the BRAF-KD in combination with Ink4a/Arf loss induces gliomas in mice. The RCAS/TVA system allows us to deliver genes to somatic Nestin-TVA cells *in vivo.* This enables determination of the roles of specific genes in glioma initiation and progression. Using this system we previously validated the role of mutant BRAF and canonical MAPK signaling in glioma development and maintenance. We found

that intracranial infection of newborn N-TVA/*Ink4a/Arf*$^{lox/lox}$ mice with RCASBP(A) viruses containing BRAF-FL^{VE}, KRAS^{G12D} or gain of function MEK (MEK^{GF}) in combination with Cre leads to the development of high-grade gliomas of various subtypes and morphologies (Robinson et al., 2010, 2011). Here, we set out to determine if the BRAF-KD is sufficient to induce gliomas *in vivo* alone or in combination with *Ink4a/Arf* loss. Newborn N-TVA/*Ink4a/Arf*$^{lox/lox}$ mice were infected intracranially with RCASBP(A) virus containing BRAF-KD and/or Cre, and survival was assessed over a 12-week period. All mice infected with RCASBP(A) viruses containing BRAF-KD (12 / 12), Cre (30 / 30) or BRAF-KD + Cre (29 / 29) survived the 12-week experimental period. Brain tissue from all injected mice was analyzed histologically. None of the mice infected with RCASBP(A) viruses containing BRAF-KD or Cre alone developed tumors; however, gliomas were detected in 21% (6 / 29) of mice injected with RCASBP(A) viruses containing BRAF-KD and Cre (Figure 2.4A). This incidence is not statistically different (P = 0.15) from our previously published experiments, where 38% (10 / 26) of mice injected with full length BRAF^{V600E} and Cre viruses developed tumors; however, the mice with BRAF-FL^{VE}-induced tumors had to be sacrificed before 12 weeks due to tumor burden (Robinson et al., 2010) whereas the BRAF-KD mice demonstrated no obvious symptoms (Figure 2.4B). Histologic analysis of the brains from the BRAF-KD cohort revealed the presence of tumors, which suggests a distinct progression from the BRAF^{V600E}-induced tumors. The stark difference in the posthoc survival analysis of tumor-bearing BRAF-KD and BRAF-FL^{VE} mice ($P < 0.001$) as well as the lower level of P-Erk1 and P-Erk2 ($P < 0.001$) in astrocytes expressing BRAF-KD compared to BRAF-FL^{VE} suggests that the BRAF-KD tumors are less malignant gliomas (Figure 2.4B and Figure 2.4C).

Histologically, the BRAF-KD *Ink4a/Arf*$^{-/-}$ tumors were highly cellular, with atypical nuclei and mitoses, similar to the BRAF-FL^{VE}-induced tumors. In contrast to the BRAF-FL^{VE}-induced tumors, the BRAF-KD–induced tumors showed a more circumscribed, less invasive border. Furthermore, the BRAF-KD-induced tumors had a lower mitotic index compared to BRAF-FL^{VE}-induced tumors (Figure 2.5A) (Robinson et al., 2010). Immunostaining for the cellular proliferation marker Ki-67 demonstrated generally lower cellular proliferation in BRAF-KD tumors compared to BRAF-FL^{VE} tumors which were consistently highly proliferative (Figure 2.5).

Similar to the BRAF-FL^{VE}-induced tumors, there was considerable heterogeneity between tumors within the same sections; some were composed mainly of spindle cells while others were predominantly epithelioid. Several tumors also contained populations of giant tumor cells (Figure 2.6A). Immunostaining using a C-terminal antibody for BRAF and for the HA-epitope tag confirmed expression of virally delivered BRAF-KD. All of the tumors expressed Nestin, and GFAP expression was present in several smaller tumors (Figure 2.6B). Together, the lower mitotic index, the lower MAPK activation, and the more circumscribed tumor borders may explain the lack of symptoms observed in these mice at 12 weeks postinjection as compared to BRAF-FL^{VE}-induced tumors. These distinct features suggest that the tumors driven by BRAF-KD have a later onset or more indolent behavior than tumors driven by BRAF^{V600E} (Robinson et al., 2010).

2.3.4 MEK and PI3K/mTOR inhibition reduces proliferation and induces significant apoptosis in cells expressing the BRAF-KD. Type 1 BRAF^{V600E} mutant inhibitors (vemurafenib, dabrafenib) have been demonstrated to cause paradoxical activation of the MAPK pathway in cells expressing the BRAF-KD fusions (Sievert et al.,

2013). Since activating mutations in BRAF drives cell growth and proliferation primarily through canonical MAPK signaling (e.g., BRAF-MEK–ERK), we chose to test the effect of Mek inhibition on the growth of cell lines driven by BRAF-FL^{VE} and BRAF-KD. The concentration required for the inhibition of Erk phosphorylation with the Mek inhibitor PD0325901 (hereafter 901) in N-TVA;*Ink4a/Arf*$^{-/-}$ astrocytes expressing BRAF-FL^{VE} and BRAF-KD, was determined by titration using 100 nmol/L and 1 μmol/L of 901. Treatment with 0.1μM significantly reduced Erk1/2 phosphorylation and 1 μM of the Mek inhibitor was sufficient for complete blockade (Figure 2.7A). As expected, we observed a negative-feedback loop between Mek and PI3K signaling, evidenced by the increasing levels of P-Akt with increasing Mek inhibition (Robinson et al., 2011); therefore, we also targeted PI3K/mTOR signaling using 1 μmol/l of the PI3K/mTOR inhibitor NVP-BEZ235 (hereafter; BEZ). The proliferation of *Ink4a/Arf*$^{-/-}$ astrocytes expressing BRAF-FL^{VE} and BRAF-KD was significantly inhibited by both 901 and BEZ. Combined treatment with 901 and BEZ produced an additive effect ($S = 1.2$, $P = 0.0633$) in the context of the BRAF-KD and synergistic effect in the context of BRAF^{V600E} ($S = 0.516$, $P = 0.0001$) as assessed by reduction in cell growth over 96 hours with synergy and additivity calculations performed as described previously (Figure 2.7B) (Robinson et al., 2011). A significant increase in apoptosis in BRAF^{V600E} and BRAF-KD cells was also observed (Figure 2.7C).

2.4 Discussion

While the role of the N-terminal segment within BRAF fusion genes (i.e., KIAA1549, SRGAP3, FAM131b) is unknown, there is evidence to suggest their possible function. SRGAP3 has been proposed to play a role in neurogenesis (Bacon et al., 2009)

and contains a Fes/CIP4 Homology (FCH) domain, which has a putative function in regulating the microtubule cytoskeleton (Yang et al., 2006). KIAA1549 harbors two transmembrane domains, which have been proposed to tether RAF to the membrane. However, the minimal FAM131b fusion component is only 9 amino acids in size and has no known or predicted function (Cin et al., 2011). Our results demonstrate that the BRAF-KD alone can cooperate with *Ink4a/Arf* loss to drive gliomagenesis *in vivo*. Deletion of the N-terminal autoinhibitory domain allows activation of the protein at sufficient levels to drive tumorigenesis. We suspect that the transforming capabilities of the various BRAF fusion genes lies within the BRAF-KD, and the promoters of FAM131b, SRGAP3, and KIAA1549 simply serve to direct expression to the appropriate cells in the brain. Thus, the result of the rearrangements is the loss of the regulatory domain leading to constitutive MAPK activation, a phenomenon that is observed in 80-90% of Pas (Jones et al., 2012). While it has been shown before that BRAF-KD^{VE} can form lesions in mice resembling PA (Gronych et al., 2011), BRAF fusion genes in humans do not harbor the V600E mutation. To our knowledge, this is the first report to show that BRAF-KD can lead to glioma development in cooperation with *Ink4a/Arf* loss.

Expression of a powerful oncogene, such as BRAF^{V600E}, in otherwise normal cells can prevent proliferation by inducing senescence; this phenomenon, referred to as 'Oncogene Induced Senescence' (OIS), is especially common in melanoma, where it prevents the progression of benign nevi with BRAF^{V600E} mutations into melanoma (Michaloglou et al., 2005). Loss of p16 expression is a common occurrence in melanoma and, interestingly, loss of p16 also correlates strongly with reduced senescence, increased cell division, and progression of PAs into WHO grade II astrocytomas (Cancer and Atlas,

2008; Horbinski et al., 2012). The BRAF-KD *Ink4a/Arf*$^{-/-}$ mice demonstrated no obvious symptoms within the 12-week experimental timeframe and survived to endpoint, in contrast to the BRAF-FL^{VE} *Ink4a/Arf*$^{-/-}$ mice that began to die from the 3rd week. Other distinguishing characteristics between the BRAF-KD and BRAF-FL^{VE} include histology showing a lack of necrosis and less invasive borders as well as immunoblotting demonstrating decreased levels of MAPK activation in tumors driven by the BRAF-KD. This suggests that the level of canonical BRAF signaling plays a role in glioma development and progression. Fascinatingly, expression of the full length KIAA1549:BRAF fusion protein has never been detected either *in vitro* or *in vivo,* even in KIAA1549:BRAF transgenic mice (Kaul et al., 2013), suggesting that sporadic PA require low levels of BRAF signaling, and that this is one way in which they may escape OIS in the context of p16 expression. Hereditary melanoma–astrocytoma syndrome is characterized by a dual predisposition to melanoma and development of low-grade paediatric astrocytomas. This syndrome is associated with germline mutations that effect only *CDKN2A* exon 1β, resulting in loss of p14 expression but not p16 expression (Randerson-Moor et al., 2001). For these reasons, future experiments will concentrate on determining the grade and response to treatment of tumors induced with BRAF-KD and either p16 or p14 loss.

MEK inhibition in gliomas is an area of ongoing study. Currently, a clinical trial (NCT02124772) is underway to investigate the efficacy of treating V600E gliomas with a combination of a Trametinib and Dabrafenib. Recently, both drugs have shown limited penetration into the brain due to active efflux across the blood-brain-barrier (BBB) (Mittapalli et al., 2013; Vaidhyanathan et al., 2014). Thus for our *in vitro* studies, we opted

for 901 because it has been shown to penetrate the BBB (Barrett et al., 2008; Rice et al., 2012). In fact, the toxic effects of 901 are likely due to its ability to cross the BBB. The paradoxical activation of the MAPK pathway caused by $BRAF^{V600E}$ inhibitors could be inhibited by dual BRAF-MEK inhibition as has been observed in melanoma, but the consequence of this is expected to be more p-AKT (Kudchadkar et al.). As proposed previously, we believe that a combination of 901 and BEZ can serve as a rational cancer therapeutic (Robinson et al., 2011). To date there have been no clinical trials studying the specific combination of BEZ and 901; however, two trials have examined the combined effect of dual inhibition MAPK and PI3K involving either BEZ or 901. NCT01337765 was a phase 1 trial for studying BEZ with a different MEK compound (MEK162), and NCT01347866 is a currently ongoing phase 1 trial to study 901 with another PI3K-mTOR compound (PF-05212384).

In summary, our findings demonstrate that the BRAF-KD region of the numerous BRAF fusion genes drives gliomagenesis. As cancers with BRAF mutations are often addicted to this signaling pathway, targeting BRAF signaling represents a reasonable therapeutic strategy. However, cells expressing KIAA1549-BRAF fusions genes display paradoxical activation when they are targeted with $BRAF^{V600E}$ inhibitors (i.e., vemurafenib) (Schnetzke et al., 2013). Unfortunately, next generation, paradox breaker BRAF inhibitors that have reduced capacity to paradoxically activate wild-type BRAF do not inhibit BRAF fusions genes at physiologically relevant doses (Le et al., 2013; Sievert et al., 2013). We previously demonstrated that efficacy of combined MEK and PI3K/mTOR inhibition for the treatment of high-grade gliomas driven by $BRAF^{V600E}$ (Robinson et al., 2011); our latest results suggest that combined MEK and PI3K/mTOR

inhibition is a rational therapy for the treatment of gliomas driven by fusion genes containing the BRAF-KD as well.

2.5 Materials and Methods

2.5.1 Mice and genotyping. Nestin-TVA;*Ink4a/Arf*$^{lox/lox}$ mice and genotyping procedures have been described (Robinson et al., 2010). The mice are on a mixed genetic background consisting of FVB/n, 129, and C57Bl/6. PCR genotyping for the TVA transgene and for the *Ink4a/Arf*^{lox} and wild-type *Ink4a/Arf* alleles was performed as described (Holmen and Williams, 2005; Robinson et al., 2010). All experiments were approved by the IACUC before experimentation.

2.5.2 Establishment of N-TVA;Ink4a/Arf*$^{lox/lox}$ *astrocytes in culture. N-TVA;*Ink4a*/*Arf*$^{lox/lox}$ primary astrocytes were established following dissection of newborn mouse brain tissue by physical disruption into single cells using scalpels and 0.25% trypsin. Cell cultures were maintained in RPMI (Invitrogen) containing 10% FBS, and gentamicin at 37°C.

2.5.3 Viral constructs. The retroviral vectors used in this study are replication-competent avian leukosis virus (ALV) long terminal repeat (LTR), splice acceptor, and Bryan polymerase-containing vectors of envelope subgroup A [designated RCASBP(A) and abbreviated RCAS]. RCASBP(A)CRE, RCASBP(A)BRAF^{V600E} and RCASBP(A)KRAS^{G12D} have been previously described (Holmen and Williams, 2005; Robinson et al., 2010). RCASBP(A)BRAF-KD was created by PCR amplification from pcDNA3.1 BRAF template DNA, [a gift from Martin McMahon (UCSF)] followed by TOPO cloning into the Gateway entry vector pCR8 (Invitrogen) and recombination into

RCASBP(A) DV using LR Clonase Enzyme Mix (Invitrogen) (Forward: atggcgtacccat acgacgtcccagactacgctaaaacacttggtagacgggactc, Reverse: cagtggacaggaaacgcacca) per the manufacturer's specifications. To propagate the RCAS viruses, proviral DNA was transfected into DF-1 cells grown at 39°C using the calcium phosphate transfection method (Kingston et al., 2003). RCAS vectors are replication-competent in the DF-1 cell line, an immortalized chicken fibroblast line, and high titer viral stocks can be obtained (Schaefer-Klein et al., 1998). The supernatants were filtered through a 0.45-μm filter, and viral titers were determined as described (Smith et al.).

2.5.4 Viral infections in vitro. Primary N-TVA;*Ink4a*/*Arf*$^{lox/lox}$ astrocytes were seeded in 6-well plates at a density of 5×10^4 cells/well and were maintained in RPMI with 5% FBS, gentamicin at 37°C as described previously (Robinson et al., 2010). After the cells attached, 1 mL of filtered virus-containing medium was added in the presence of 8 μg/ml polybrene (Sigma) for 2 h at 37°C in 5% CO_2.

2.5.5 Growth in soft agar. To assess anchorage-independent growth, 1.5×10^5 cells were suspended in 0.35% Difco agar noble (Becton Dickinson) in RPMI with 10% FBS and layered over presolidified 0.65% Difco Noble Agar in RPMI with 10% FBS per well of a six-well dish. Each cell line was assayed in triplicate.

2.5.6 Western blotting. Protein concentrations were determined using the Bio-Rad D_C Protein Assay (Bio-Rad). The proteins were separated on a 4-20% Tris-glycine gradient polyacrylamide gel, transferred to nitrocellulose, and incubated for 1 h at room temperature in blocking solution (0.05% Tween-20 in Tris-buffered saline with 5% NFDM or 5% BSA). Blots were immunostained for the following antigens: phospho-Erk at Thr202/Tyr204 (4370, 1:1000, Cell Signaling); total Erk (9102, 1:1000, Cell Signaling);

tubulin (T9026, 1:5000, Sigma); HA epitope on BRAF-KD (HA.11, 1:1000, Covance); C-terminus of BRAF (SC166, 1:500, Santa Cruz Biotechnology); and $BRAF^{V600E}$ (E1929, 1:2000, Spring Bioscience). The blots were then incubated with an anti-mouse or anti-rabbit IgG-HRP secondary antibody, incubated with ECL solution (Amersham), and exposed to film (Kodak).

2.5.7 In vivo infection. Infected DF-1 cells from a confluent culture in a 10-cm dish were trypsinized, pelleted, resuspended in 50 μL PBS, and placed on ice. Newborn mice were injected intracranially 2 mm ventral from bregma (intersection of the coronal and sagittal sutures) with 5 μL of infected DF-1 cells using a gas-tight Hamilton syringe as described previously (Robinson et al., 2010, 2011).

2.5.8 Histological analysis. Brain tissue from injected mice was fixed in 10% formalin, embedded in paraffin and 5-μm sections were adhered to glass slides. The sections were stained with hematoxylin and eosin or left unstained for immunohistochemistry (IHC). Images were captured using a Zeiss Axio microscope equipped with an AxioCam ICc3 camera (Zeiss).

2.5.9 Immunohistochemistry. Tissue sections were deparaffinized and antigen retrieval was performed in 'Diva Decloaking' buffer (Biocare Medical) by boiling for 10 min. Sections were treated with 3% H_2O_2 and blocked in Background Sniper (Biocare Medical) for 10 min. Primary antibodies were diluted in Renaissance background reducing diluent (Biocare Medical). Sections were incubated overnight at 4°C and probed with Mach 4 rabbit polymer reagent (Biocare Medical) or Mach 4 mouse probe for 15 min followed by Mach 4 polymer for 15 min for mouse monoclonal antibodies. Visualization was carried out with DAB (Biocare Medical). Sections were counterstained with hematoxylin.

Antibodies against the following antigens were used: GFAP (13-0300, 1:500, Invitrogen); synaptophysin (ab32127, 1:200, Abcam); BRAF-KD (detected using an antibody to the HA epitope (HA.11, 1:1000, Covance) and C-terminal BRAF antibody (SC166, 1:500, Santa Cruz Biotechnology)); Nestin (ab6142, 1:200, Abcam); phospho-Erk (4370, 1:100, Cell Signaling); and Ki-67 (M7246, 1:50, Dako,) using a rabbit anti-rat linker (P0450, 1:50, Dako).

2.5.10 Drug treatment. To measure the effect of MEK inhibition on phosphorylated Erk (P-Erk) in astrocytes expressing BRAF constructs, drug was serially diluted in 10-fold increments in RPMI containing 2% FBS and added to cells in 6-well plates. 0.1% DMSO vehicle was added in negative control wells. After 1 h, cells were washed twice in PBS before analysis by Western blot. To measure the effect of the MEK inhibitor PD0325901 or the PI3K/mTOR inhibitor NVP-BEZ235 on cell proliferation as measured by ATP levels, drug was diluted to 1.0 μM and added to astrocytes. After 96 h, ATP levels were detected using the ATPlite 1step Luminescence Assay System (Perkin Elmer), following the manufacturer's instructions. In brief, 100μl of reconstituted ATPlite reagent was added to cells in a 96-well plate. The plate was incubated on an orbital shaker at 700rpm for 3 min and dark-adapted for 10 min before luminescence was read for 0.1 sec per well on a Synergy HT multimode microplate reader (BioTek). To measure the effect of the MEK inhibitor PD0325901 or the PI3K/mTOR inhibitor NVP-BEZ235 on apoptosis, drugs were diluted to 1.0 μM and added to astrocytes. After 96 h, the cells were resuspended in Guava Viacount reagent (Millipore) and 5000 events per sample were read according to the manufacturer's instructions, as described previously (Robinson et al., 2011). All drug treatment experiments were done in three biological replicates.

2.5.11 Statistical analysis. Western blot density analysis was performed using Image J. Kaplan Meier survival data analysis and determination of synergy between PD032509 and NVP-BEZ235 were done as previously described (Robinson et al., 2011). To compare means, two-tailed Student's t test was used. P values below 0.05 were considered significant.

2.6 Acknowledgements

This work was supported by the Huntsman Cancer Institute, the National Brain Tumor Foundation, the American Cancer Society [RSG-06-198-01-TBE], and the National Institutes of Health [R01NS073870]. We thank Joshua Sonnen for his helpful comments about histology. We also thank Rowan Arave for her assistance.

2.7 References

Abounader, R. (2009). Interactions between PTEN and receptor tyrosine kinase pathways and their implications for glioma therapy. Expert Rev. Anticancer Ther. *9*, 235–245.

Bacon, C., Endris, V., and Rappold, G. (2009). Dynamic expression of the Slit-Robo GTPase activating protein genes during development of the murine nervous system. J. Comp. Neurol. *513*, 224–236.

Barrett, S.D., Bridges, A.J., Dudley, D.T., Saltiel, A.R., Fergus, J.H., Flamme, C.M., Delaney, A.M., Kaufman, M., LePage, S., Leopold, W.R., et al. (2008). The discovery of the benzhydroxamate MEK inhibitors CI-1040 and PD 0325901. Bioorg. Med. Chem. Lett. *18*, 6501–6504.

Cancer, T., and Atlas, G. (2008). Comprehensive genomic characterization defines human glioblastoma genes and core pathways. Nature *455*, 1061–1068.

Chin, L., Pomerantz, J., and DePinho, R. a (1998). The INK4a/ARF tumor suppressor: one gene--two products--two pathways. Trends Biochem. Sci. *23*, 291–296.

Cin, H., Meyer, C., Herr, R., Janzarik, W.G., Lambert, S., Jones, D.T.W., Jacob, K., Benner, A., Witt, H., Remke, M., et al. (2011). Oncogenic FAM131B-BRAF fusion

resulting from 7q34 deletion comprises an alternative mechanism of MAPK pathway activation in pilocytic astrocytoma. Acta Neuropathol. *121*, 763–774.

Forshew, T., Tatevossian, R.G., Lawson, A.R.J., Ma, J., Neale, G., Ogunkolade, B.W., Jones, T.A., Aarum, J., Dalton, J., Bailey, S., et al. (2009). Activation of the ERK/MAPK pathway: a signature genetic defect in posterior fossa pilocytic astrocytomas. J. Pathol. *218*, 172–181.

Gronych, J., Korshunov, A., Bageritz, J., Milde, T., Jugold, M., Hambardzumyan, D., Remke, M., Hartmann, C., Witt, H., Jones, D.T.W., et al. (2011). An activated mutant BRAF kinase domain is sufficient to induce pilocytic astrocytoma in mice. J. Clin. Invest. *121*, 1344–1348.

Holmen, S.L., and Williams, B.O. (2005). Essential role for Ras signaling in glioblastoma maintenance. Cancer Res. *65*, 8250–8255.

Horbinski, C., Hamilton, R.L., Nikiforov, Y., and Pollack, I.F. (2010). Association of molecular alterations, including BRAF, with biology and outcome in pilocytic astrocytomas. Acta Neuropathol. *119*, 641–649.

Horbinski, C., Nikiforova, M.N., Hagenkord, J.M., Hamilton, R.L., and Pollack, I.F. (2012). Interplay among BRAF, p16, p53, and MIB1 in pediatric low-grade gliomas. Neuro. Oncol. *14*, 777–789.

Ivanchuk, S.M., Mondal, S., and Rutka, J.T. (2008). p14ARF interacts with DAXX: effects on HDM2 and p53. Cell Cycle *7*, 1836–1850.

Jones, D.T.W., Kocialkowski, S., Liu, L., Pearson, D.M., Bäcklund, L.M., Ichimura, K., and Collins, V.P. (2008). Tandem duplication producing a novel oncogenic BRAF fusion gene defines the majority of pilocytic astrocytomas. Cancer Res. *68*, 8673–8677.

Jones, D.T.W., Kocialkowski, S., Liu, L., Pearson, D.M., Ichimura, K., and Collins, V.P. (2009). Oncogenic RAF1 rearrangement and a novel BRAF mutation as alternatives to KIAA1549:BRAF fusion in activating the MAPK pathway in pilocytic astrocytoma. Oncogene *28*, 2119–2123.

Jones, D.T.W., Gronych, J., Lichter, P., Witt, O., and Pfister, S.M. (2012). MAPK pathway activation in pilocytic astrocytoma. Cell. Mol. Life Sci. *69*, 1799–1811.

Kaul, A., Chen, Y.-H., Emnett, R.J., Dahiya, S., and Gutmann, D.H. (2012). Pediatric glioma-associated KIAA1549:BRAF expression regulates neuroglial cell growth in a cell type-specific and mTOR-dependent manner. Genes Dev. *26*, 2561–2566.

Kaul, A., Chen, Y.-H., Emnett, R.J., Gianino, S.M., and Gutmann, D.H. (2013). Conditional KIAA1549:BRAF mice reveal brain region- and cell type-specific effects. Genesis *51*, 708–716.

Kingston, R.E., Chen, C.A., and Okayama, H. (2003). Calcium phosphate transfection. Curr. Protoc. Cell Biol. *Chapter 20*, Unit 20.3.

Kondo, Y., Hollingsworth, E.F., and Kondo, S. (2004). Molecular targeting for malignant gliomas (Review). Int. J. Oncol. *24*, 1101–1109.

Kudchadkar, R., Paraiso, K.H.T., and Smalley, K.S.M. Targeting mutant BRAF in melanoma: current status and future development of combination therapy strategies. Cancer J. *18*, 124–131.

Lawson, A.R.J., Tatevossian, R.G., Phipps, K.P., Picker, S.R., Michalski, A., Sheer, D., Jacques, T.S., and Forshew, T. (2010). RAF gene fusions are specific to pilocytic astrocytoma in a broad paediatric brain tumour cohort. Acta Neuropathol. *120*, 271–273.

Le, K., Blomain, E.S., Rodeck, U., and Aplin, A.E. (2013). Selective RAF inhibitor impairs ERK1/2 phosphorylation and growth in mutant NRAS, vemurafenib-resistant melanoma cells. Pigment Cell Melanoma Res. *26*, 509–517.

Michaloglou, C., Vredeveld, L.C.W., Soengas, M.S., Denoyelle, C., Kuilman, T., van der Horst, C.M. a M., Majoor, D.M., Shay, J.W., Mooi, W.J., and Peeper, D.S. (2005). BRAFE600-associated senescence-like cell cycle arrest of human naevi. Nature *436*, 720–724.

Mittapalli, R.K., Vaidhyanathan, S., Dudek, A.Z., and Elmquist, W.F. (2013). Mechanisms limiting distribution of the threonine-protein kinase B-RaF(V600E) inhibitor dabrafenib to the brain: implications for the treatment of melanoma brain metastases. J. Pharmacol. Exp. Ther. *344*, 655–664.

Quelle, D.E., Zindy, F., Ashmun, R. a, and Sherr, C.J. (1995). Alternative reading frames of the INK4a tumor suppressor gene encode two unrelated proteins capable of inducing cell cycle arrest. Cell *83*, 993–1000.

Randerson-Moor, J. a, Harland, M., Williams, S., Cuthbert-Heavens, D., Sheridan, E., Aveyard, J., Sibley, K., Whitaker, L., Knowles, M., Bishop, J.N., et al. (2001). A germline deletion of p14(ARF) but not CDKN2A in a melanoma-neural system tumour syndrome family. Hum. Mol. Genet. *10*, 55–62.

Rice, K.D., Aay, N., Anand, N.K., Blazey, C.M., Bowles, O.J., Bussenius, J., Costanzo, S., Curtis, J.K., Defina, S.C., Dubenko, L., et al. (2012). Novel Carboxamide-Based Allosteric MEK Inhibitors: Discovery and Optimization Efforts toward XL518 (GDC-0973). ACS Med. Chem. Lett. *3*, 416–421.

Robinson, J.P., VanBrocklin, M.W., Guilbeault, a R., Signorelli, D.L., Brandner, S., and Holmen, S.L. (2010). Activated BRAF induces gliomas in mice when combined with Ink4a/Arf loss or Akt activation. Oncogene *29*, 335–344.

Robinson, J.P., Vanbrocklin, M.W., Lastwika, K.J., McKinney, a J., Brandner, S., and Holmen, S.L. (2011). Activated MEK cooperates with Ink4a/Arf loss or Akt activation to induce gliomas in vivo. Oncogene *30*, 1341–1350.

Roussel, M.F. (1999). The INK4 family of cell cycle inhibitors in cancer. Oncogene *18*, 5311–5317.

Schaefer-Klein, J., Givol, I., Barsov, E. V, Whitcomb, J.M., VanBrocklin, M., Foster, D.N., Federspiel, M.J., and Hughes, S.H. (1998). The EV-O-derived cell line DF-1 supports the efficient replication of avian leukosis-sarcoma viruses and vectors. Virology *248*, 305–311.

Schiffman, J.D., Hodgson, J.G., VandenBerg, S.R., Flaherty, P., Polley, M.-Y.C., Yu, M., Fisher, P.G., Rowitch, D.H., Ford, J.M., Berger, M.S., et al. (2010). Oncogenic BRAF mutation with CDKN2A inactivation is characteristic of a subset of pediatric malignant astrocytomas. Cancer Res. *70*, 512–519.

Schnetzke, U., Fischer, M., Frietsch, J.J., Finkensieper, A., Clement, J.H., Hochhaus, A., and Rosée, P. La (2013). Paradoxical MAPK-activation in response to treatment with tyrosine kinase inhibitors in CML: Flow cytometry loses track. Cytometry B. Clin. Cytom. *17*, 601–603.

Sievert, A.J., Jackson, E.M., Gai, X., Hakonarson, H., Judkins, A.R., Resnick, A.C., Sutton, L.N., Storm, P.B., Shaikh, T.H., and Biegel, J. a (2009). Duplication of 7q34 in pediatric low-grade astrocytomas detected by high-density single-nucleotide polymorphism-based genotype arrays results in a novel BRAF fusion gene. Brain Pathol. *19*, 449–458.

Sievert, A.J., Lang, S., Katie, L., Madsen, P.J., Slaunwhite, E., Choudhari, N., Kellet, M., Storm, P.B., Resnick, A.C., Kjetland, E.F., et al. (2013). Paradoxical activation and RAF inhibitor resistance of BRAF protein kinase fusions characterizing pediatric astrocytomas. Proc. Natl. Acad. Sci. *110*, 8750–8750.

Smith, E.J., Fadly, A., and Okazaki, W. An enzyme-linked immunosorbent assay for detecting avian leukosis-sarcoma viruses. Avian Dis. *23*, 698–707.

Tatevossian, R.G., Lawson, A.R.J., Forshew, T., Hindley, G.F.L., Ellison, D.W., and Sheer, D. (2010a). MAPK pathway activation and the origins of pediatric low-grade astrocytomas. J. Cell. Physiol. *222*, 509–514.

Tatevossian, R.G., Tang, B., Dalton, J., Forshew, T., Lawson, A.R., Ma, J., Neale, G., Shurtleff, S.A., Bailey, S., Gajjar, A., et al. (2010b). MYB upregulation and genetic aberrations in a subset of pediatric low-grade gliomas. Acta Neuropathol. *120*, 731–743.

Vaidhyanathan, S., Mittapalli, R.K., Sarkaria, J.N., and Elmquist, W.F. (2014). Factors Influencing the CNS Distribution of a Novel MEK 1/2 Inhibitor: Implications for Combination Therapy for Melanoma Brain Metastases. Drug Metab. Dispos.

Yang, Y., Marcello, M., Endris, V., Saffrich, R., Fischer, R., Trendelenburg, M.F., Sprengel, R., and Rappold, G. (2006). MEGAP impedes cell migration via regulating actin and microtubule dynamics and focal complex formation. Exp. Cell Res. *312*, 2379–2393.

Zhang, J., Wu, G., Miller, C.P., Tatevossian, R.G., Dalton, J.D., Tang, B., Orisme, W., Punchihewa, C., Parker, M., Qaddoumi, I., et al. (2013). Whole-genome sequencing identifies genetic alterations in pediatric low-grade gliomas. Nat. Genet. *45*, 602–612.

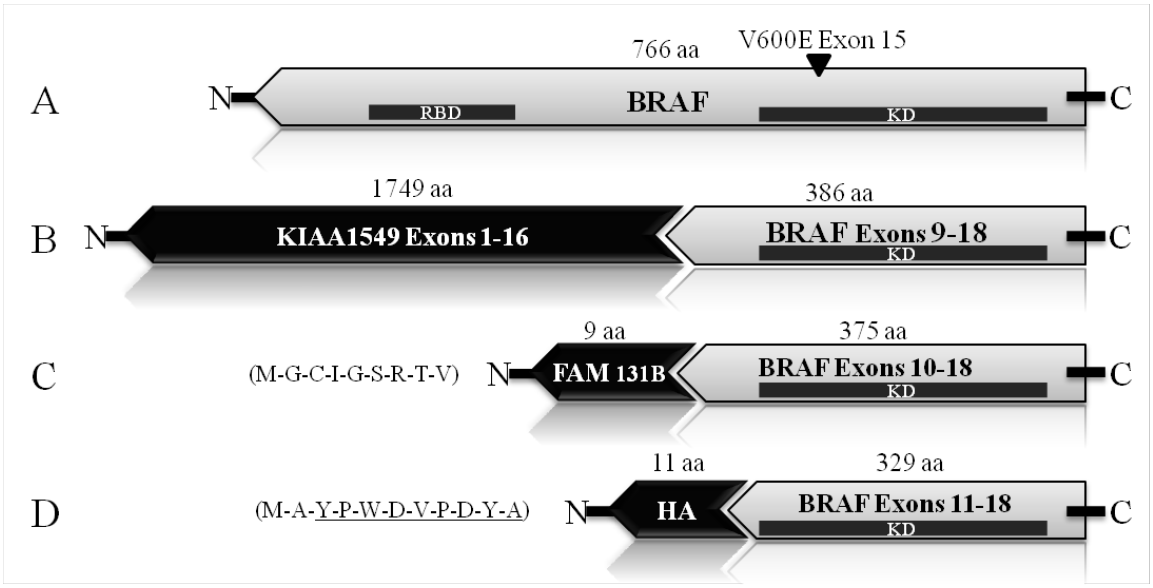

Figure 2.1 BRAF schematic. A: $BRAF^{V600E}$ **B:** KIAA1549:BRAF **C:** FAM131B-BRAF, showing FAM131B amino acids **D:** BRAF-kinase domain (BRAF-KD), showing amino acids of the HA epitope Tag. RBD=Ras binding domain.

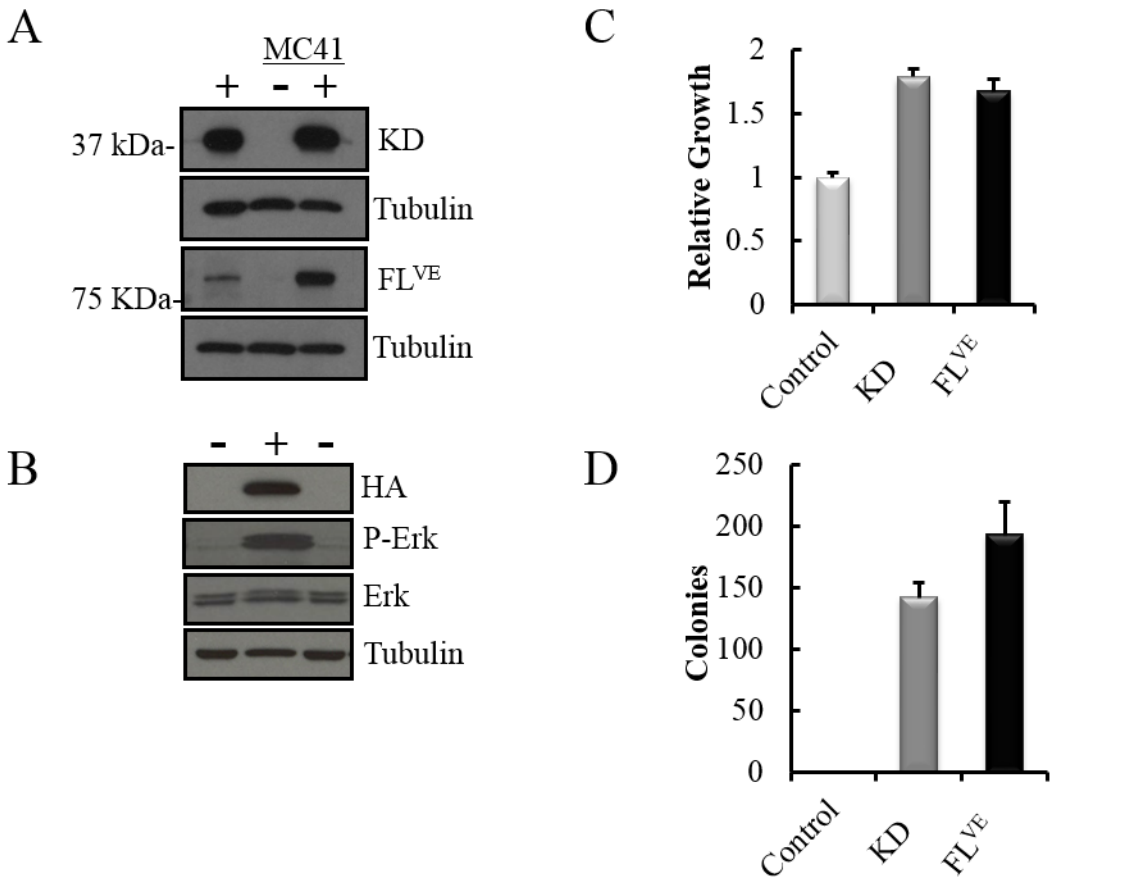

Figure 2.2 Analysis of the expression and functional activity of the BRAF-KD in the context of *Ink4a/Arf*-deficiency. A: Western blot of *Ink4a/Arf*-deficient astrocytes (MC41+) infected with BRAF-KD (KD) and $BRAF^{V600E}$ (FL^{VE}) with corresponding uninfected, negative control astrocytes (MC41-), and positive control avian fibroblasts (+). **B:** BRAF-KD expression causes MAPK activation as measured by P-Erk in BRAF-KD transfected human 293FT cells (+) compared to mock transfected cells (-). **C:** Relative proliferation of *Ink4a/Arf*-deficient astrocytes infected with BRAF-KD (KD) or $BRAF^{V600E}$ (FL^{VE}) compared to uninfected, control cells. The mean of three replicates is shown with error bars for standard error. **D:** Colony formation of *Ink4a/Arf*-deficient astrocytes infected with BRAF-KD (KD) or $BRAF^{V600E}$ (FL^{VE}) compared to uninfected, control cells in soft agar. Error bars reflect standard error of three replicates.

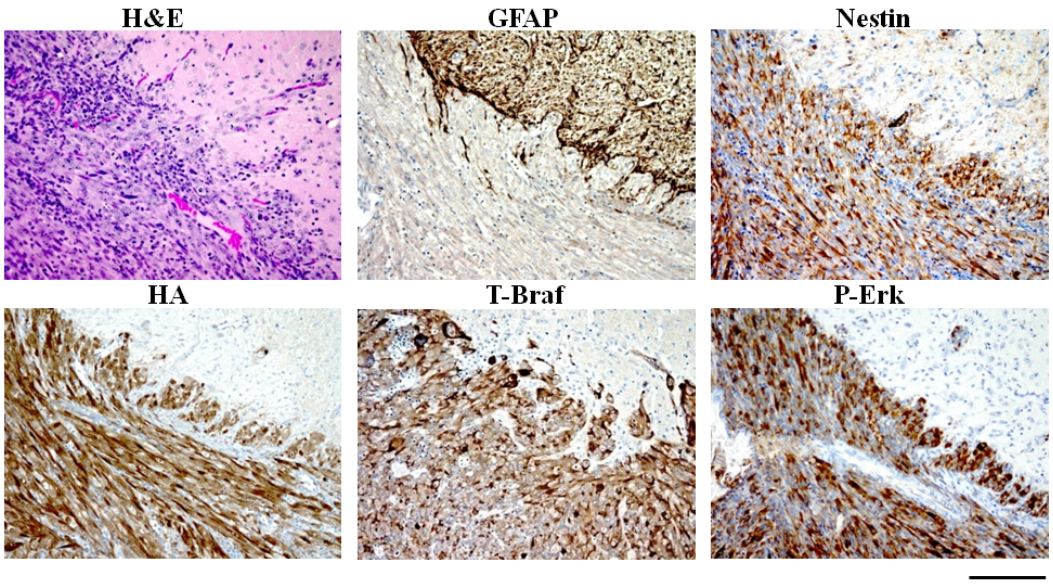

Figure 2.3 Histological examination of brain sections from mice injected with *Ink4a/Arf*-deficient astrocytes expressing BRAF-KD. H&E: sections stained with hematoxylin and eosin. IHC for P-Erk demonstrates that the MAPK pathway is active in the tumor but not adjacent normal brain. Nestin and GFAP are glial specific markers. BRAF-KD expression was detected by IHC for the HA epitope tag on virally delivered BRAF or by using the C-terminal BRAF antibody. IHC sections were counterstained with hematoxylin. Scale bar represents 200μm.

A

Genes delivered	Mice	Incidence
Cre	0/30	0%
BRAF-KD	0/12	0%
BRAF-KD+ Cre	6/29	21 %
Previously published data		
BRAF-FL^{VE}	*0/28*	*0%*
BRAF-FL^{VE} + Cre	*10/26*	*38 %*

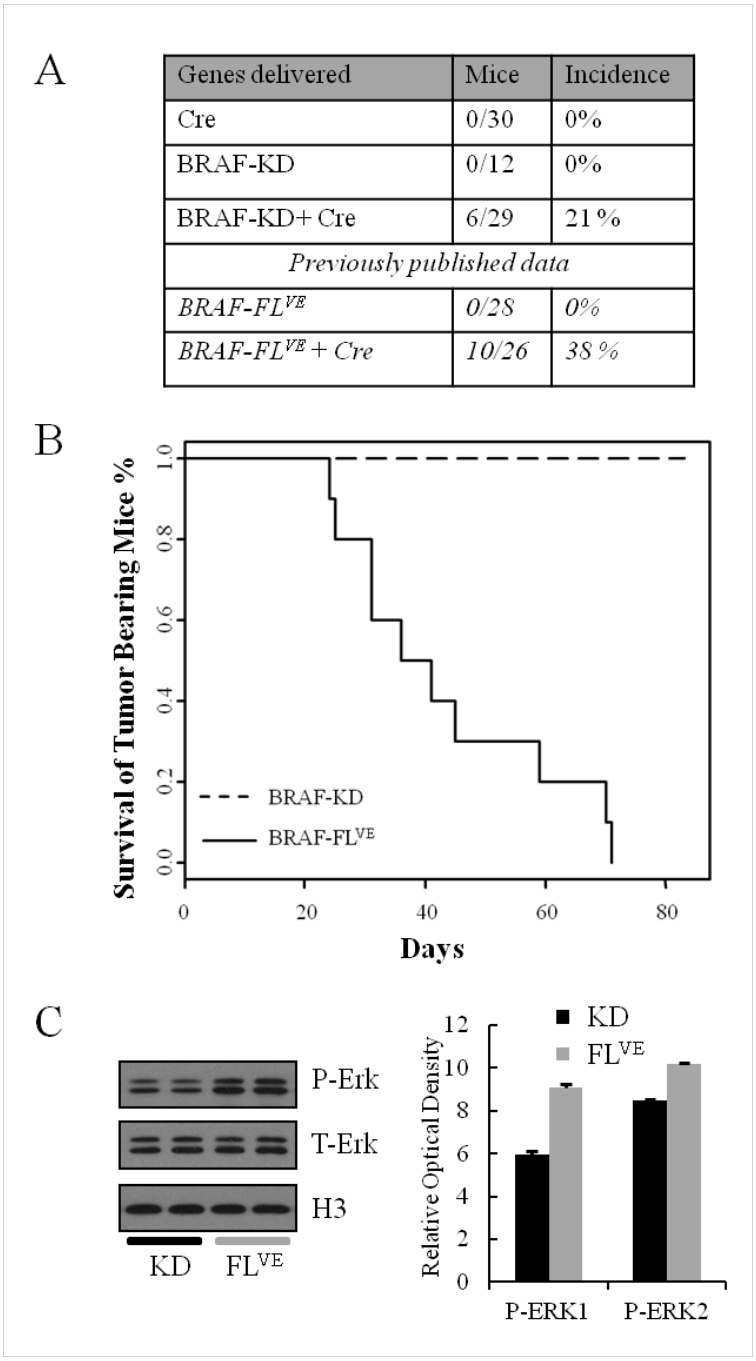

Figure 2.4 Difference in survival of tumor-bearing mice between BRAF-KD and BRAF-FL^{VE}. A: Incidence of tumor formation for BRAF-KD and BRAF-FL^{VE} in Nestin-TVA;*Ink4a/Arf$^{lox/lox}$* mice. **B:** Kaplan-Meier post-hoc survival analysis between BRAF-KD *Ink4a/Arf$^{-/-}$* and BRAF-KD *Ink4a/Arf$^{-/-}$* mice. **C:** Western blot comparing P-Erk levels between BRAF-KD *Ink4a/Arf$^{-/-}$* and BRAF-FL^{VE} *Ink4a/Arf$^{-/-}$* astrocytes with corresponding quantification of P-Erk relative to total levels of Erk. Data are represented as mean ± S.E.M of six replicates, of which two are shown in the western blot.

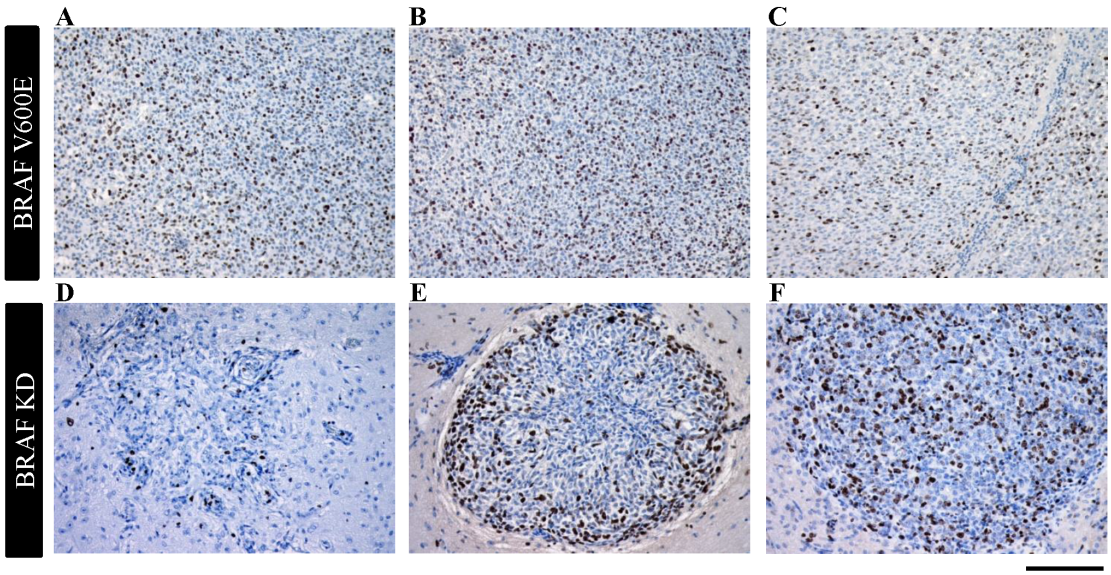

Figure 2.5 A comparison of cellular proliferation between brain sections from RCASBP(A) BRAF-KD & CRE injected and RCASBP(A) BRAFV600E & CRE injected mice. IHC for cellular proliferation marker Ki67 demonstrated that BRAFV600E tumors (A-C) were consistently highly proliferative while proliferation varied significantly in BRAF-KD tumors (D-F). IHC sections were counterstained with hematoxylin. Scale bar represents 200μm.

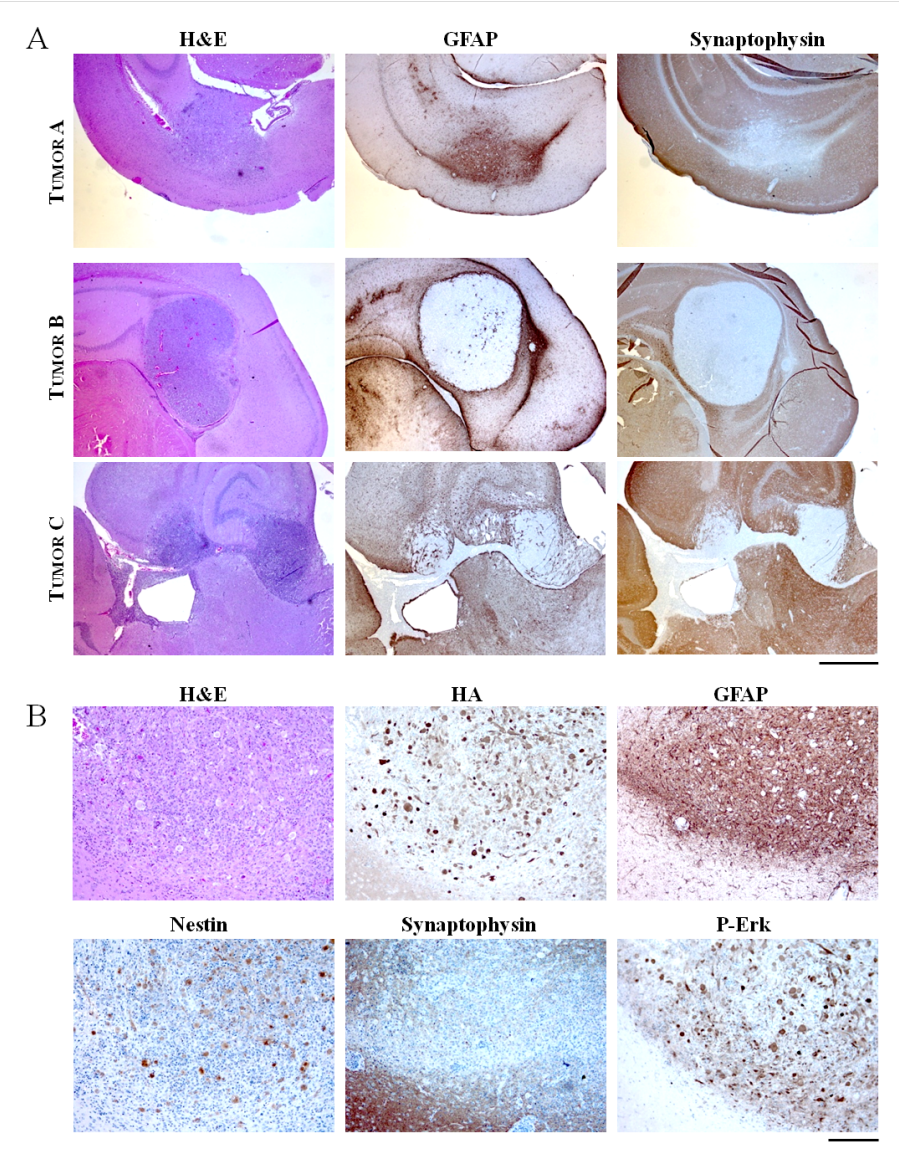

Figure 2.6 Histological examination of brain sections from RCASBP(A) BRAF-KD and CRE injected mice. A: Representative low-power images of brain sections from tumor-bearing mice are shown. H&E: sections stained with hematoxylin and eosin. IHC for synaptophysin demonstrated that none of the tumors were neuronal in origin. Tumor A is representative of tumors that expresses the astrocyte maker GFAP while tumor B is an example that was negative for GFAP expression. Cells in tumor C possessed spindle cell morphology, while tumor B was more epithelioid, and tumor A was mixed as well as containing a population of large, nondividing giant cells. Scale bar represents 1mm. **B:** High-power histological examination of a GFAP expressing tumor. IHC for synaptophysin demonstrates that the tumors are not neuronal and expresses the astrocyte maker GFAP. BRAF-KD expression was detected by IHC for the HA epitope tag on virally delivered BRAF. IHC for P-Erk demonstrates that the MAPK pathway is active in the tumor but not adjacent normal brain. IHC sections were counterstained with hematoxylin. Scale bar represents 200μm.

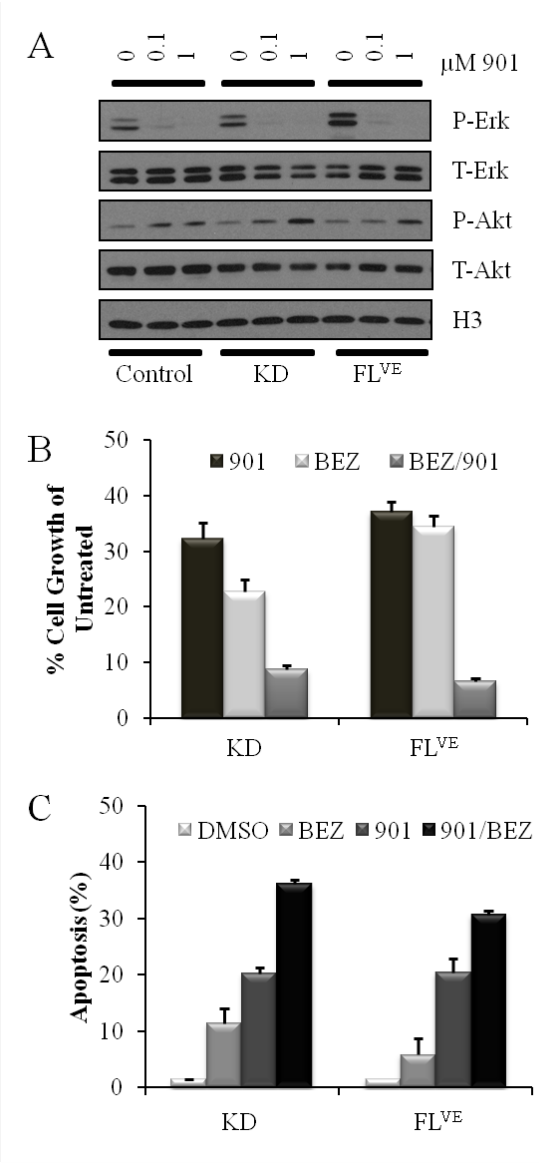

Figure 2.7 Pharmacological inhibition of cells harboring mutant BRAF. A: MEK Inhibition with PD0325901 at 0 μM, 0.1 μM, and 1.0 μM for one hour in RPMI 2% FBS of *Ink4a/Arf*-deficient astrocytes infected with BRAF-KD (KD) and $BRAF^{V600E}$ (FL^{VE}) with corresponding uninfected, negative control astrocytes. MEK inhibition decreases P-Erk levels by western blot. **B:** Growth inhibition in *Ink4a/Arf*-deficient astrocytes infected with BRAF-KD (KD) and $BRAF^{V600E}$ (FL^{VE}) treated in triplicate with 1 μmol/l PD0325901 (901), 1 μmol/l NVP-BEZ235 (BEZ) or combination (BEZ/901) for 96 h. Cells treated with vehicle alone (DMSO) served as controls. Cell growth was measured using the ATPlite assay. Data was normalized to untreated controls and are represented as mean ± S.E.M. **C:** Apoptosis induced by inhibition of MEK and PI3K/mTOR signaling in mouse astrocytes. *Ink4a/Arf*-deficient astrocytes infected with BRAF-KD (KD) and $BRAF^{V600E}$ (FL^{VE}) were treated in triplicate with either DMSO as a control, 1 μmol/l PD0325901 (901), 1 μmol/l NVP-BEZ235 (BEZ) or in combination (BEZ/901) for 96 h. Apoptosis was quantitated using Guava ViaCount. Data are represented as mean ± S.E.M.

CHAPTER 3

HBEGF MODELS THE CLASSICAL SUBTYPE OF GLIOBLASTOMA IN THE CONTEXT OF INK4A/ARF AND PTEN LOSS THROUGH AXL AND EGFR

3.1 Preface

This chapter is a reformatted version of a manuscript submitted to *Cancer Discovery* in April 2016. The work presented herein was completed with the following coauthors: James P. Robinson, Joshua A. Sonnen and Sheri L. Holmen.

3.2 Introduction

Malignant gliomas, including anaplastic astrocytomas and glioblastomas (GBM), are aggressive tumors that confer a poor prognosis upon diagnosis (Louis et al., 2007; Ostrom et al., 2014). Anaplastic astrocytomas are characterized by high mitotic activity and cytological atypia. Glioblastomas retain the features of lower grade gliomas but additionally present with microvascular proliferation and/or pseudopalisading necrosis (Louis et al., 2007). With treatment, which consists of surgery, radiotherapy, and chemotherapy, the average survival for patients diagnosed with GBM is about 14 months (Ostrom et al., 2014). Therefore, there is a strong need to understand the mechanisms

underlying malignant glioma initiation and maintenance such that new targets can be identified and new therapies developed.

Glioblastoma was the first cancer type to be systematically analyzed by The Cancer Genome Atlas (TCGA) network. An integrated genomic approach was used to identify numerous alterations in the disease (Brennan et al., 2013; Verhaak et al., 2010). Sequencing of these human malignant gliomas revealed several alterations in three core pathways. The receptor tyrosine kinase (RTK) – RAS – phosphatidylinositol-3-kinase (PI3K) pathway was altered in 88% of samples, the retinoblastoma (RB) pathway was altered in 78% of samples, and the p53 pathway was altered in 87% of samples (Brennan et al., 2013; Verhaak et al., 2010). In the RTK-RAS-PI3K axis, the most common alterations were mutation or amplification of epidermal growth factor receptor (EGFR) and homozygous deletion of phosphatase and tensin homolog deleted on chromosome ten (PTEN). In the p53 and RB pathways, the most common lesion was homozygous deletion of cyclin-dependent kinase 2A (CDKN2A), which encodes both $p16^{INK4a}$ and $p19^{ARF}$. *EGFR*-amplified tumors, which account for 65% of glioblastomas, are often associated with increased expression of EGFR ligands including heparin-binding epidermal growth factor (EGF)-like growth factor (HBEGF) (Acquaviva et al., 2011; Mishima et al., 1998; Ramnarain et al., 2006).

HBEGF has been associated with the progression of many solid tumors, including breast, pancreatic, and ovarian (He et al., 2015; Ray et al., 2013; Yotsumoto et al., 2010). In up to 40% of primary malignant gliomas, HBEGF has been shown to be co-expressed with EGFR by immunohistochemistry (Mishima et al., 1998; Ramnarain et al., 2006). Additionally, *HBEGF* mRNA transcripts were two- to five-fold greater in GBM compared

to normal brain tissue (Mishima et al., 1998). In normal mouse astrocytes, HBEGF increases cell proliferation and nestin expression, a sign of dedifferentiation (Puschmann et al., 2014). HBEGF is also mitogenic in human glioma cell lines and this activity can be blocked with HBEGF-neutralizing antibodies (Mishima et al., 1998; Ramnarain et al., 2006). In addition to activation of EGFR, HBEGF has been shown in bladder cancer cells to have other pleiotropic properties, including induction of matrix metalloproteinase 9 (MMP9) and vascular endothelial growth factor (VEGF) expression, which allows for tumor invasion and proliferation (Ongusaha et al., 2004). In chicken fibroblasts, expression of HBEGF induces transformation (Fu et al., 1999). In U251 glioma cells, expression of EGFRvIII, the most common variant of EGFR, induces expression of HBEGF. Moreover, silencing of HBEGF decreases EGFRvIII-tumorigenicity in this context (Li et al., 2014; Ramnarain et al., 2006). However, the ability of HBEGF to promote transformation in astrocytes *in vitro* and induce or sustain gliomas *in vivo* has not been assessed.

In the current study, we used the well-established RCAS/TVA glioma mouse model to assess the role of HBEGF in glioma development and maintenance *in vivo*. Compared to genetically engineered models, where every cell within a given tissue carries the genetic lesion, tumors generated using this model arise from a small number of cells within a normal microenvironment, which mimics the human disease. Furthermore, mammalian cells ectopically expressing the viral receptor TVA can be infected with several different RCAS viruses to allow the determination of the minimal components required for tumorigenesis. We demonstrate that HBEGF can promote tumor development in the context of either *Ink4a/Arf* and/or *Pten* loss. Furthermore, suppression of HBEGF expression in tumor-bearing mice resulted in significantly increased survival, which

suggests it may be a relevant target for therapy. Interestingly, we discovered that HBEGF signals through both Egfr and Axl in this context. While AXL has been implicated in glioblastoma formation, it has not been previously reported to play a role in HBEGF signal transduction (Hutterer et al., 2008; Vajkoczy et al., 2006). Therefore, our findings have important implications for the treatment of glioblastoma.

3.3 Results

3.3.1 Overexpression of HBEGF correlates with decreased survival in GBM patients. To assess the effect of ligand overexpression on patient survival, we compared the median survival among cohorts of patients whose tumors overexpressed one of seven different EGFR ligands. We observed that patients harboring malignant gliomas that overexpressed HBEGF had a median survival of only 7.4 months, which was significantly shorter than the median survival of 13.6 months in patients with malignant gliomas that did not overexpress HBEGF (Table 3.1). This suggests that overexpression of HBEGF confers a worse prognosis in these patients. Although HBEGF has been shown to increase the proliferation of human glioma cells *in vitro* (Mishima et al., 1998), little is known about the role of this ligand in the biology of malignant gliomas.

3.3.2 HBEGF promotes anchorage-independent growth. To evaluate the role(s) of specific genes in glioma initiation, progression and maintenance, we and others have used a somatic-cell gene delivery method based on the RCAS/TVA retroviral vector system and successfully induced malignant gliomas *in vivo* (Robinson et al., 2010; Van Brocklin et al., 2012). Using this established model system, we initially assessed the ability of HBEGF to transform primary astrocytes derived from Nestin-TVA;*Ink4a/Arf*$^{lox/lox}$ mice.

These astrocytes were infected with RCAS-Cre alone or in combination with either RCAS-HBEGF and/or RCAS-EGFR. Following confirmation of HBEGF and EGFR expression (Figure 3.1A), the ability of the astrocytes to grow in an anchorage-independent manner was assessed by growth in soft agar. These astrocytes were immortalized by deletion of *Ink4a/Arf* to allow for ease of growth in culture but they are not transformed, as evidenced by the lack of colonies detected in the Nestin-TVA*;Ink4a/Arf*$^{-/-}$ astrocytes without EGFR or HBEGF infection (Figure 3.1B). Anchorage-independent growth was detected in astrocytes expressing HBEGF ($P < 0.001$). While colonies were also observed when EGFR was expressed in the absence of HBEGF, they were significantly fewer in number than was observed in astrocytes expressing HBEGF ($P = 0.01$). No significant difference in colony number was observed between astrocytes expressing HBEGF alone or co-expressing EGFR ($P = 0.2$). This suggests that HBEGF was the limiting factor in this context because the addition of exogenous EGFR did not significantly increase colony formation. EGFR activity was confirmed by adding known quantities of HBEGF (0ng/ml, 0.5ng/ml and 5.0ng/ml) to astrocytes either without (-) or with exogenous receptor (EGFR) (Figure 3.1C). Dose-dependent phosphorylation of EGFR (Y1068), as well as activation of downstream targets, including Akt (S473) and Erk1/2 (T202/204), was observed.

3.3.3 Expression of HBEGF results in reduced survival in vivo in the context of Ink4a/Arf or Pten loss. To evaluate the effect of HBEGF expression in nestin-expressing cells *in vivo*, we utilized Nestin-TVA;*Ink4a/Arf*$^{lox/lox}$ mice and generated both Nestin-TVA;*Pten*$^{lox/lox}$ and Nestin-TVA;*Ink4a/Arf*$^{lox/lox}$;*Pten*$^{lox/lox}$ mice. Exons 2 and 3 of the *Ink4a/Arf* locus are flanked by *LoxP* sites such that in the absence of Cre these mice express normal levels of p16^{INK4a} and p19^{ARF}. Cre-mediated excision renders both *p16*^{Ink4a} and

p19^{Arf} nonfunctional (Aguirre et al., 2003). Exon 5 of the *Pten* locus is flanked by *LoxP* sites such that in the absence of Cre, these mice express normal levels of Pten. Cre-mediated excision eliminates exon 5, which encodes for a region of Pten that is essential for its phosphatase activity (Zheng et al., 2008). Delivery of Cre alone did not result in a decrease in survival within the experimental time point of 16 weeks in any of the strains evaluated (Figure 3.2B and Table 3.2). Intracranial delivery of viruses containing HBEGF and Cre in Nestin-TVA;*Ink4a/Arf*$^{lox/lox}$ mice resulted in a mean survival of 68.5 ± 21.2 days, whereas expression of HBEGF and Cre resulted in a mean survival of 56.1 ± 11.8 days in Nestin-TVA;*Pten*$^{lox/lox}$ mice and 28.7 ± 2.3 days in Nestin-TVA;*Ink4a/Arf*$^{lox/lox}$;*Pten*$^{lox/lox}$ mice (Figure 3.2A and Table 3.2). A significant difference in mean survival was observed between each of these cohorts ($P < 0.05$) (Figure 3.2A).

3.3.4 Addition of exogenous EGFR does not enhance the effect of HBEGF in vivo. Although a significant difference was not observed in soft-agar colony formation when exogenous EGFR was co-expressed with HBEGF, there may be enhanced signaling *in vivo*. We pursued this possibility by delivering RCAS-EGFR along with RCAS-Cre and RCAS-HBEGF in Nestin-TVA;*Ink4a/Arf*$^{lox/lox}$, Nestin-TVA;*Pten*$^{lox/lox}$, and Nestin-TVA;*Ink4a/Arf*$^{lox/lox}$;*Pten*$^{lox/lox}$ mice. The median survival for these cohorts was not significantly different than the same cohorts that lacked exogenous EGFR ($P > 0.1$) (Figure 3.2A, Figure 3.2B, and Table 3.2).

3.3.5 HBEGF-expressing mouse tumors histologically resemble human malignant gliomas. Brain sections were examined following necropsy and were scored as no tumor, low-grade tumor, and high-grade tumor based on histological features apparent on H&E sections. Low-grade tumors demonstrated single cell infiltration with nuclear

atypia, including hyperchromasia and pleomorphism, while high grade tumors also exhibited mitotic figures, vascular proliferation, and areas of pseudopalisading necrosis (Figure 3.3A and Figure 3.3B). Seventy-five percent of the tumors were high grade when both Ink4a/Arf and Pten were lost, while only 36% were high grade with Pten loss alone. No high-grade tumors were observed with loss of Ink4a/Arf alone, but 45% of mice developed low-grade tumors in this cohort. No tumors were observed in brain sections of mice injected only with HBEGF or Cre (Figure 3.3C and Table 3.2). Virally delivered HBEGF was detected in all tumors using immunohistochemistry (IHC) (Figure 3.3A). Loss of Ink4a/Arf and Pten were also confirmed with immunohistochemistry (Figure 3.4). All tumors also expressed the astrocyte marker glial fibrillary acidic protein (GFAP) and the neural progenitor cell marker nestin, though less staining was observed in the tumors with loss of Ink4a/Arf alone (Figure 3.3A). Assessment by IHC of the proliferative marker Ki67 showed that tumors lacking Pten or Pten and In4a/Arf were more proliferative than tumors lacking only Ink4a/Arf ($P < 0.03$) (Figure 3.3B and Figure 3.3D). Tumor penetrance correlated with mean survival; cohorts with combined Ink4a/Arf and Pten loss displayed the highest penetrance (100%), followed by those with Pten loss (90%) and Ink4a/Arf loss (45%) (Figure 3.2A and Figure 3.3C).

3.3.6 EGFR and AXL mediate HBEGF signaling in mouse astrocytes. To determine if HBEGF signals through other RTKs, we performed an unbiased approach using the R&D Proteome Profiler, a membrane-based antibody array, which detects phosphorylation of 39 mouse receptor tyrosine kinase receptors simultaneously. Isogenic astrocytes from Nestin-TVA*;Ink4a/Arf*$^{lox/lox}$ mice were infected with either RCAS-Cre or RCAS-Cre and RCAS-HBEGF in combination. The cells were serum-starved for 24 hours,

lysed, and subjected to the Proteome Profiler immunoassay. As expected, Egfr was phosphorylated in the presence of HBEGF (Figure 3.5A and Figure 3.6). Interestingly, the only other RTK that was differentially phosphorylated was Axl (Figure 3.5 and Figure 3.6). To ascertain the functional significance of Axl phosphorylation in this context, we used Clustered Regularly Interspaced Short Palindromic Repeats (CRISPR)-based gene editing to delete Egfr and/or Axl in the mouse astrocytes. Guide RNAs specific for mouse Egfr and Axl were designed and expressed in vectors containing resistance genes for blasticidin and puromycin, respectively. Single-cell clones were selected and expanded. Gene editing and loss of expression were confirmed through high-resolution melt analysis (HRMA), sequencing, and western blot (Figure 3.5B). Because the guide RNAs are specific for the mouse genome, we performed rescue experiments using the human orthologs of EGFR and AXL (Figure 3.5B). Anchorage-independent growth was assessed by soft agar assay in this context. Cells lacking either Egfr, Axl, or both had significantly fewer colonies than the positive control. Interestingly, loss of Egfr alone had significantly fewer colonies than loss of Axl alone (Figure 3.5C). Expression of human EGFR and/or AXL was able to partially rescue the single knockouts and completely rescue the double knockout in the anchorage-independent growth assay (Figure 3.5C).

3.3.7 HBEGF-driven mouse GBM most closely resembles the classical subtype of human GBM. Human GBM has been classified into four different subtypes: proneural, classical, mesenchymal, and neuronal (Verhaak et al., 2010). High-grade HBEGF-driven tumors in mice resemble human GBM histologically (Figure 3.3A and Figure 3.7A), but it is unclear which subtype, if any, they model. To determine if HBEGF-driven GBM resembled a particular subtype, we generated high-grade gliomas in Nestin-

TVA;*Ink4a/Arf*$^{lox/lox}$;*Pten*$^{lox/lox}$ mice by delivery of RCAS-Cre and RCAS-HBEGF. In addition, in the same mouse strain, gliomas were generated with RCAS-Cre in combination with RCAS-PDGFA or RCAS-BRAF^{V600E}, other drivers previously found to form high-grade gliomas (Figure 3.7A) (Ozawa et al., 2014; Robinson et al., 2010). Previously, gliomas driven by PDGFA in the context of *Ink4a/Arf* and *Pten* loss were shown to resemble the proneural subtype using microarray bead chip technology (Ozawa et al., 2014). RNA was extracted from formalin-fixed paraffin-embedded (FFPE) tumor tissue that had been histologically confirmed by a board-certified Neuropathologist (J.A.S.). Three tumors from each cohort along with brain tissue from six control Nestin-TVA-negative *Ink4a/Arf*$^{lox/lox}$;*Pten*$^{lox/lox}$ mice were analyzed by RNA sequencing from a Ribo-Zero treated library (Figure 3.8A). The transcript coverage and exonic mapping rate were typical for FFPE tissue (Figure 3.8B and Figure 3.8C). The sample cross correlation heat map shows that each of the tumor replicates clustered with each other and the controls clustered separately from the tumors (Figure 3.8A). The transcriptome of each cohort was compared to the TCGA GBM subtype classifier genes after converting those genes to their mouse orthologs. The highest correlation for HBEGF was with the classical subtype (r = 0.14), for PDGFA was the proneural subtype (r = 0.30), for BRAF was the mesenchymal subtype (r = 0.47), and for the control was the neural subtype (r = 0.26), as shown on the heat map (Figure 3.7B). Although the correlation values are relatively low, the results replicated the proneural classification for PDGFA-driven tumors as previously described (Ozawa et al., 2014).

In both our *in vitro* and *in vivo* assays evaluating the oncogenic potential of HBEGF, we did not observe a significant difference with combined overexpression of

EGFR (Figure 3.1B and Figure 3.2B). This suggests that endogenous EGFR is sufficient when HEBGF is overexpressed or that an alternative signaling pathway could be possible. The Proteome Profiler and CRISPR knockout functional studies suggest a role for Axl in HBEGF signaling (Figure 3.5A and Figure 3.5C). Differential expression analysis in the tumors from RNA sequencing showed specific upregulation of Egfr and Axl transcripts in HBEGF tumors (Figure 3.9). In PDGFA-driven tumors, there was specific upregulation of Pdgfra (Figure 3.9). These results were confirmed with real-time PCR for Axl and Egfr on the same tumor samples (Figure 3.7C). HBEGF-driven tumors had a 10-fold increase in Egfr transcript and 6-fold increase in Axl transcript compared to healthy controls and PDGFA-driven tumors (P value < 0.03). HBEGF-directed expression of EGFR likely explains why endogenous EGFR was sufficient both *in vitro* and *in vivo.*

3.3.8 Suppression of HBEGF expression results in tumor regression and increased survival in vivo. *In vitro* neutralizing antibodies that recognize HBEGF decrease the proliferation of cultured glioma cells, suggesting that HBEGF is important for tumor cell maintenance (Mishima et al., 1998; Ramnarain et al., 2006; Sato et al., 2012). Translating these findings *in vivo* is complicated by pharmacological limitations in drug kinetics and perfusion across the blood-brain barrier. To bypass these limitations, we utilized a genetic approach to determine whether HBEGF is required for tumor maintenance *in vivo*. We have previously described the generation of a viral vector that allows expression of inserted genes to be regulated postdelivery using the tet-regulated system (Holmen and Williams, 2005). A tet-responsive element (TRE) was inserted immediately downstream of the envelope gene in the replication-competent avian retroviral vector RCANBP(A) such that expression of any gene inserted downstream of the TRE was

driven from this promoter and not the viral LTR. Expression from the TRE requires the presence of a tetracycline transcriptional activator (tTA) such as tet-off or a reverse tTA (rtTA) such as tet-on. In the context of tet-on, the tet-responsive gene is expressed only in the presence of doxycycline (Dox); in the context of tet-off, the tet-responsive gene is repressed in the presence of Dox (Kistner et al., 1996). In the context of tet-off expression *in vitro*, we observed HBEGF expression that was effectively suppressed by the administration of Dox (Figure 3.10A).

Tumors were generated in Nestin-TVA*;Ink4a/Arf*$^{lox/lox}$ and Nestin-TVA;*Pten*$^{lox/lox}$ mice with retroviruses containing TRE-*HBEGF*, *tet-off*, and *Cre* and confirmed with MRI imaging at 21 days of age. In the Nestin-TVA*;Ink4a/Arf*$^{lox/lox}$ mice, tumor-bearing mice were split into two cohorts, one receiving standard feed ($n = 9$) and one receiving Dox feed ($n = 10$). While the mean survival in the untreated mice was 43.0 ± 7.9 days, the mean survival in the mice treated was 103.7 ± 4.9 days ($P < 0.001$) (Figure 3.10B). In the Nestin-TVA;*Pten*$^{lox/lox}$ mice, tumor-bearing mice were divided into two cohorts, one receiving standard feed ($n = 11$) and one receiving Dox feed ($n = 15$). While the mean survival in the untreated mice was 46.8 ± 6.5 days, all Dox-treated mice survived to the experimental endpoint of 112 days ($P < 0.001$) (Figure 3.10C). Consistent with the survival analysis, 40% of the tumor-bearing Nestin-TVA*;Ink4a/Arf*$^{lox/lox}$ mice experienced tumor regression detectable by MRI, while all of the tumor-bearing Nestin-TVA;*Pten*$^{lox/lox}$ mice showed no evidence of disease (Figure 3.10D and Figure 3.10E). We have previously demonstrated that Dox has no innate tumor suppressive properties; therefore, tumor regression is due to inhibition of HBEGF expression in this context (Robinson et al., 2011).

Intracranial injection of TRE-*HBEGF*, *tet-off*, and *Cre* containing retroviruses into

newborn Nestin-TVA;*Ink4a/Arf*$^{lox/lox}$;*Pten*$^{lox/lox}$ mice led to the formation of high-grade tumors in all injected mice (Figure 3.11A). To evaluate the kinetics of virally delivered HBEGF expression and activity following Dox treatment, we treated mice with Dox for 3 days. Expression of HBEGF as detected by IHC was visible without Dox treatment; however, following 72 hours of Dox treatment very little HBEGF expression was visible by IHC (Figure 3.11A). A significant difference was observed in the mean number of cells staining positively for the proliferation marker Ki67 between the mice that received standard feed and the mice that received Dox feed. While 41.4 ± 4.3 Ki67 positive cells were detected per HPF in the untreated tumor samples, 5.7 ± 1.2 Ki67 positive cells were detected per HPF in the samples treated with Dox for 72 hours ($P = 0.02$) (Figure 3.11B).

MRI was performed at 21 days of age to identify tumor-bearing mice and to monitor tumor growth or regression at multiple time points throughout the study. One cohort of tumor-bearing mice received standard feed ($n = 16$) and the other cohort received Dox feed continuously starting at 21 days of age ($n = 10$). Survival rates were compared between untreated mice and mice given Dox to determine whether the suppression of HBEGF expression increased survival. While the mean survival in the untreated mice was 23.9 ± 0.8 days, the mean survival in the mice treated starting at 21 days was 83.9 ± 7.7 days ($P < 0.001$), with one mouse still alive at the experimental endpoint of 16 weeks (Figure 3.11C). This mouse remains tumor-free by MRI at 20 weeks of age (Figure 3.12A). To assess tumor maintenance in more advanced tumors, another cohort received Dox feed starting at 28 days of age ($n = 10$) (Figure 3.11C). The mean survival in the mice treated starting at 28 days was 62.0 ± 7.5 days, which was significantly different from the untreated mice ($P < 0.001$). Furthermore, the mice treated at 28 days also had significantly reduced

mean survival compared to the mice treated at 21 days ($P = 0.02$), demonstrating that earlier treatment increases survival.

3.3.9 Recurrent tumors develop in the absence of HBEGF expression in the context of Ink4a/Arf and Pten loss. Tumors recurred in 19 / 20 responding Nestin-TVA;*Ink4a/Arf*$^{lox/lox}$;*Pten*$^{lox/lox}$ mice while on Dox treatment. The MRI data from a representative mouse that developed recurrent disease while on Dox treatment is shown in Figure 3.12B. A small tumor is visible before Dox treatment but no tumor was visible at 28, 42, or 64 days; however, tumor recurrence was visible starting at 84 days and a large recurrent tumor was detected at 104 days. Brain tissue was examined and H&E analysis confirmed GBM in this mouse. Of evaluable mice with recurrent tumors, 50% re-expressed HBEGF and 50% recurred in the absence of HBEGF expression (Figure 3.11D and Figure 3.13). Future studies will evaluate the mechanism(s) of resistance in tumors that recurred in the absence of HBEGF expression.

3.4 Discussion

Using an established mouse model of glioma (Robinson et al., 2010), we assessed the sufficiency of HBEGF in gliomagenesis. While not sufficient on its own, HBEGF cooperates with *Ink4a/Arf* or *Pten* loss to promote gliomagenesis. To our knowledge, this is the first report showing that HBEGF can lead to malignant glioma development in this context. Comparison of the HBEGF tumors to the human subtype signatures show that they most closely resemble the classical subtype (Verhaak et al., 2010). We also show that previously published mouse models for PDGFA and BRAF^{V600E} resemble the proneural and mesenchymal subtypes, respectively (Ozawa et al., 2014; Robinson et al., 2010;

Verhaak et al., 2010).

We have observed that in astrocytes *in vitro*, HBEGF activates not only Egfr but also Axl, a member of the TAM family of RTKs. AXL has been shown to be upregulated in human glioma cell lines and tissue, but activation of AXL in the presence of HBEGF has not previously been reported in gliomas or other cancers (Hutterer et al., 2008; Vajkoczy et al., 2006). Although unreported in the context of HBEGF, a role for AXL in mediating EGFR signaling has been cited as a mechanism of resistance against targeted EGFR therapies in lung and breast cancer (Liu et al., 2009; Zhang et al., 2012). It is thought that there is a physical interaction between the two receptors, allowing for transactivation that permits enhanced, diversified downstream signaling. It is possible that HBEGF activates AXL via transactivation from an activated EGFR receptor. This phenomenon has been reported in breast cancer cells, where AXL was found to co-immunoprecipitate with EGFR (Meyer et al., 2013).

While determination of the initial events in the genesis of a glioma are biologically important, it is perhaps more important clinically to ascertain the conditions for tumor maintenance to help guide clinical intervention. As an initial step toward developing targeted therapies, we used a tetracycline-regulated system to control HBEGF expression to assess the necessity of HBEGF in sustaining tumor growth. We demonstrated increased mean survival in all cohorts of mice after inhibition of HBEGF. While half of the tumors in the Nestin-TVA;*Ink4a/Arf*$^{lox/lox}$;*Pten*$^{lox/lox}$ mice recurred due to re-activation of HBEGF, half recurred in the absence of HBEGF expression. Future studies will evaluate the mechanism(s) of resistance in these tumors. Our study suggests that HBEGF not only promotes the formation of gliomas but is also important for tumor maintenance, which

suggests that it is a good target for therapy.

3.5 Materials and Methods

3.5.1 Mice and genotyping. Nestin-TVA;*Ink4a/Arf*$^{lox/lox}$, Nestin-TVA;*Pten*$^{lox/lox}$, Nestin-TVA;*Ink4a/Arf*$^{lox/lox}$;*Pten*$^{lox/lox}$ mice were generated from pre-existing strains (kind gifts of Eric Holland, Ronald DePinho, and Marcus Bosenberg). The mice are on a mixed genetic background consisting of FVB/n, 129, and C57Bl/6. PCR genotyping for the TVA transgene and for the *Ink4a/Arf*^{lox}, wild-type *Ink4a/Arf, Pten*^{lox}, and wild-type *Pten* alleles was performed as previously described (Cho et al., 2015). All experiments were approved by the IACUC before experimentation. For treatment studies, diet containing 625 mg/kg of doxycycline was used (Envigo Teklad TD.08434).

3.5.2 Cell culture. Nestin-TVA;*Ink4a/Arf*$^{lox/lox}$ primary astrocytes were established by physical disruption of newborn mouse brains into single cells using scalpels and 0.25% trypsin. Cell cultures were maintained in RPMI (Invitrogen) containing 10% FBS and 0.5% gentamicin at 37°C with 5% CO2. To disrupt Egfr and Axl via CRISPR gene editing, astrocytes were infected with VSV-G-pseudotyped plenti-CRISPRv2-Egfr (target: CCTCCATTAGACCATCCAGG) containing blasticidin resistance and/or plenti-CRISPRv2-Axl (target: CAGGTGCCAGAGGACTCACG) containing puromycin resistance. Clones were selected using 2.5 μg/ml puromycin and/or 80 μg/ml blasticidin. Both CRISPR-Cas9 constructs were generated by the Mutation Generation and Detection (MGD) core at the University of Utah. Clones were first screened with high-resolution melt analysis (HRMA) with the following primers: EGFR-HF (CTCCTGGACCCACTTCTT GTTC), EGFR-HR (AGGGATTCTCTCCACGGTGTTG), AXL-HF (CACCTGGGT

CTGGGTGTTATC), and AXL-HR (CCAGGGAATATCACAGGTGCCA) and then edited candidates were confirmed with sanger sequencing EGFR-SF (GTGGGAGT CACAGCACGTTAAA), EGFR-SR (TCACTTACCAAGGCTGACTGGA), AXL-SF (TATCACAAGCTCAGAGCCACGT), AXL-SR (ATCCCAGGCCTTCTTCCTAACA) followed by western blot analysis.

3.5.3 Viral constructs. The avian retroviral vectors used in this study are either replication-competent Avian Leukosis Virus (ALV) long terminal repeat (LTR) splice acceptor Bryan polymerase subgroup A [RCASBP(A)] or replication-competent ALV LTR no splice acceptor Bryan polymerase subgroup A [RCANBP(A)], hereafter referred to as RCAS and RCAN, respectively. RCAS-CRE and RCAS-TETOFF have previously been described (Van Brocklin et al., 2012). RCAS-HBEGF and RCAN-TRE-HBEGF were created by PCR amplification from pcDNA3-proHB-EGF-CS (Addgene #11601) using AGCTTGGTACCGAGCTCG and GTCAATGGTGATGGTGATGAT primers, followed by TOPO cloning into the Gateway entry vector pCR8 (Invitrogen) and recombination into RCAS-DV or RCAN-DV using LR Clonase Enzyme Mix (Invitrogen). RCAS-EGFR and RCAS-AXL were also cloned using LR recombination from the Human Kinase ORF Kit (Addgene Kit #1000000014). RCAS-PDGFA was cloned using LR recombination from the Gateway PLUS shuttle X03795.1 (Genecopoeia). RCAS-BRAF^{V600E} has been described previously (Robinson et al., 2010). To propagate the viruses, proviral DNA was transfected into DF-1 cells, an immortalized chicken fibroblast line, grown at 39°C using the calcium phosphate transfection method. RCAS vectors are replication-competent in the DF-1 cell line and high titer viral stocks were obtained.

3.5.4 In vitro infection. Primary astrocytes were seeded in 6-well plates at a density of 5×10^4 cells/well and maintained in RPMI with 10% FBS and 1% gentamicin at 37 °C. After the cells attached, 1 mL of filtered virus-containing medium was added in the presence of 8 μg/ml polybrene (Sigma) for 3 h at 37°C in 5% CO_2 and repeated on three consecutive days.

3.5.5 Soft Agar assay. To assess anchorage-independent growth, 1.5×10^5 cells were suspended in 0.35% Difco Noble Agar (Becton Dickinson) in RPMI with 10% FBS and layered over presolidified 0.65% Difco Noble Agar in RPMI with 10% FBS per well of a six-well dish. Each cell line was assayed in triplicate following 1μg/μl nitroblue tetrazolium stain (Invitrogen) added 200 μl overnight.

3.5.6 Western blotting. Protein concentrations were determined using the Bio-Rad D_C Protein Assay (Bio-Rad). The proteins were separated on 4-20% or 8-16% Tris-glycine gradient polyacrylamide gels, transferred to nitrocellulose, and incubated for 1 h at room temperature in blocking solution (0.05% Tween-20 in Tris-buffered saline with 5% NFDM or 5% BSA). Blots were immunostained for the following antigens: phospho-Erk at Thr202/Tyr204 (#4370, 1:1000, CST); total Erk (#9102, 1:1000, CST); vinculin (#4650, 1:1000, CST); H3 (#4499, 1:2000, CST); phosphor-Egfr (#3777, 1:1000, CST); Egfr (#4267, 1:1000, CST); Axl (#4977, 1:1000, CST); and HBEGF (#AF-259-NA, 1:500, R&D). The blots were then incubated with an anti-mouse or anti-rabbit IgG-HRP secondary antibody as appropriate, incubated with ECL solution (Amersham), and exposed to film (Kodak).

3.5.7 R&D Proteome Profiler RTK-Array. Astrocytes were serum-starved overnight and then lysed in buffer provided in the Proteome Profiler Mouse Phospho-RTK

Array Kit (R&D). After binding of lysate with detection antibody and subsequent washing, array membranes were chemiluminescently detected with film (Kodak). The arrays were quantitated by densitometry using Image J.

3.5.8 In vivo infection. Infected DF-1 cells from a confluent culture in a 10-cm dish were trypsinized, pelleted, resuspended in 50 µL PBS, and placed on ice. Newborn mice were injected intracranially 2 mm ventral from bregma (intersection of the coronal and sagittal sutures) with 5 µL of infected DF-1 cells using a gas-tight Hamilton syringe as described previously (Robinson et al., 2010).

3.5.9 Histological analysis. Brain tissue from injected mice was fixed in 10% formalin, embedded in paraffin, and 4-µm sections were adhered to glass slides. The sections were stained with hematoxylin and eosin or left unstained for immunohistochemistry (IHC). Images were captured using a Zeiss Axio microscope equipped with an AxioCam ICc3 camera (Zeiss).

3.5.10 Bioinformatics and genomics. TCGA glioblastoma survival data were accessed through the cBioPortal (Cerami et al., 2012). For RNAseq analysis, tumors were microdissected from 10 µm FFPE sections and extracted using the Ambion Recoverall Kit (Ambion). Samples were prepped by the High-throughput Genomics Core at University of Utah with TruSeq Stranded Total RNA with Ribo-Zero Gold and then sequenced with HiSeq 50 Cycle Single-Read Sequencing v4 (Illumina). Reads were aligned to the mouse genome (mm10) and differential gene expression were determined with the open source USeq/DESeq2 package by the Bioinformatics Analysis core at the University of Utah. Genes were selected using two thresholds, an FDR of <10% and absolute log2 ratio > 1. GBM classifier genes were accessed from the TCGA data portal and were converted to

mouse orthologues genes using Biomart (Ozawa et al., 2014; Verhaak et al., 2010). Tumor and control variance normalized expression data (rlog values) were converted to median-centered log2 fold change and compared to the TCGA classifier genes using pairwise Pearson correlations.

3.5.11 Immunohistochemistry. Tissue sections were deparaffinized and antigen retrieval was performed in Rodent Decloaker (Biocare Medical) by boiling at 120 °C for 10 min. Sections were treated with 3% H_2O_2 and blocked in Rodent Block M (Biocare Medical) for 30 min. Primary antibodies were diluted in Renaissance background reducing diluent (Biocare Medical). Sections were incubated overnight at 4 °C and probed with Mach 4 HRP-polymer, Mouse-on-Mouse HRP-polymer, Rat-on-Mouse HRP-polymer or Goat-on-Rodent HRP-polymer (Biocare Medical) for 30 min. Visualization was carried out with Betazoid DAB (Biocare Medical). Sections were counterstained with hematoxylin. Antibodies against the following antigens were used: GFAP (#13-0300, 1:200, Invitrogen), Pten (#M3627, 1:150, Dako), $p19^{ARF}$ (#MA1-16664, Invitrogen), synaptophysin (#ab32127, 1:200, Abcam), Nestin (#ab6142, 1:250, Abcam), HBEGF (#AF-259-NA, 1:250, R&D) and Ki-67 (#M7246, 1:100, Dako).

3.5.12 Magnetic resonance imaging. Mice were anesthetized using 2% isoflurane with oxygen (1 L/min). A 50 µl bolus of MultiHance (Bracco) MRI contrast was injected intraperitoneally 15 min before scanning. A fast gradient-echo three-plane localizer for graphical prescription preceded acquisition of contrast-enhanced images on a 7T Bruker MRI using a T_1-weighted multislice multiecho (MSME) sequence, as previously described (Van Brocklin et al., 2012; Robinson et al., 2011) (Robinson et al., 2011; Van Brocklin et al., 2012).

3.5.13 Statistical analysis. Western blot and RTK array density analysis were performed using Image J. Survival data analysis was done using a log-rank test of the Kaplan Meier estimate of survival. To compare means, two-tailed Student's t test was used. P values below 0.05 were considered significant.

3.6 Acknowledgements

We thank the members of the VanBrocklin, McMahon, and Holmen labs as well as E. Holland, R. DePinho, and M. Bosenberg for providing mouse strains, reagents, and advice. We thank the Huntsman Cancer Institute Vivarium staff for assistance. We thank Tim Parnell for his bioinformatics expertise. We also thank Adam Welker for his immunohistochemistry optimizations. We acknowledge the use of the Mutation Generation and Detection Core, the DNA Synthesis Core, the DNA Sequencing Core, and the Small Animal Imaging Core supported by P30 CA042014 awarded to Huntsman Cancer Institute from the National Cancer Institute. We also acknowledge use of the Huntsman Cancer Institute Shared Resources for high-throughput genomics and bioinformatics analysis, glass wash, and research histology. This work was supported by the National Institute of Neurological Disorders and Stroke [R01NS073870] and the National Cancer Institute [F30CA203096].

3.7 References

Acquaviva, J., Jun, H.J., Lessard, J., Ruiz, R., Zhu, H., Donovan, M., Woolfenden, S., Boskovitz, A., Raval, A., Bronson, R.T., et al. (2011). Chronic activation of wild-type epidermal growth factor receptor and loss of Cdkn2a cause mouse glioblastoma formation. Cancer Res. *71*, 7198–7206.

Aguirre, A.J., Bardeesy, N., Sinha, M., Lopez, L., Tuveson, D. a, Horner, J., Redston, M.S.,

and Depinho, R. a (2003). Activated Kras and Ink4a / Arf deficiency cooperate to produce metastatic pancreatic ductal adenocarcinoma. Genes Dev. 3112–3126.

Brennan, C.W., Verhaak, R.G.W., McKenna, A., Campos, B., Noushmehr, H., Salama, S.R., Zheng, S., Chakravarty, D., Sanborn, J.Z., Berman, S.H., et al. (2013). The somatic genomic landscape of glioblastoma. Cell *155*, 462–477.

Van Brocklin, M.W., Robinson, J.P., Lastwika, K.J., McKinney, A.J., Gach, H.M., and Holmen, S.L. (2012). Ink4a/Arf loss promotes tumor recurrence following Ras inhibition. Neuro. Oncol. *14*, 34–42.

Cerami, E., Gao, J., Dogrusoz, U., Gross, B.E., Sumer, S.O., Aksoy, B.A., Jacobsen, A., Byrne, C.J., Heuer, M.L., Larsson, E., et al. (2012). The cBio Cancer Genomics Portal: An open platform for exploring multidimensional cancer genomics data. Cancer Discov. *2*, 401–404.

Cho, J.H., Robinson, J.P., Arave, R.A., Burnett, W.J., Kircher, D.A., Chen, G., Davies, M.A., Grossmann, A.H., VanBrocklin, M.W., McMahon, M., et al. (2015). AKT1 Activation Promotes Development of Melanoma Metastases. Cell Rep. *13*, 898–905.

Fu, S. l, Bottoli, I., Goller, M., and Vogt, P.K. (1999). Heparin-binding epidermal growth factor-like growth factor, a v-Jun target gene, induces oncogenic transformation. Proc. Natl. Acad. Sci. U. S. A. *96*, 5716–5721.

He, C., Lv, X., Hua, G., Lele, S.M., Remmenga, S., Dong, J., Davis, J.S., and Wang, C. (2015). YAP forms autocrine loops with the ERBB pathway to regulate ovarian cancer initiation and progression. Oncogene 1–15.

Holmen, S.L., and Williams, B.O. (2005). Essential role for Ras signaling in glioblastoma maintenance. Cancer Res. *65*, 8250–8255.

Hutterer, M., Knyazev, P., Abate, A., Reschke, M., Maier, H., Stefanova, N., Knyazeva, T., Barbieri, V., Reindl, M., Muigg, A., et al. (2008). Axl and growth arrest-specific gene 6 are frequently overexpressed in human gliomas and predict poor prognosis in patients with glioblastoma multiforme. Clin. Cancer Res. *14*, 130–138.

Kistner, A., Gossen, M., Zimmermann, F., Jerecic, J., Ullmer, C., Lübbert, H., and Bujard, H. (1996). Doxycycline-mediated quantitative and tissue-specific control of gene expression in transgenic mice. Proc. Natl. Acad. Sci. U. S. A. *93*, 10933–10938.

Li, L., Chakraborty, S., Yang, C.-R., Hatanpaa, K.J., Cipher, D.J., Puliyappadamba, V.T., Rehman, a, Jiwani, a J., Mickey, B., Madden, C., et al. (2014). An EGFR wild type-EGFRvIII-HB-EGF feed-forward loop regulates the activation of EGFRvIII. Oncogene *33*, 4253–4264.

Liu, L., Greger, J., Shi, H., Liu, Y., Greshock, J., Annan, R., Halsey, W., Sathe, G.M.,

Martin, A.M., and Gilmer, T.M. (2009). Novel mechanism of lapatinib resistance in HER2-positive breast tumor cells: Activation of AXL. Cancer Res. *69*, 6871–6878.

Louis, D.N., Ohgaki, H., Wiestler, O.D., Cavenee, W.K., Burger, P.C., Jouvet, A., Scheithauer, B.W., and Kleihues, P. (2007). The 2007 WHO classification of tumours of the central nervous system. Acta Neuropathol. *114*, 97–109.

Meyer, A.S., Miller, M.A., Gertler, F.B., and Lauffenburger, D.A. (2013). The receptor AXL diversifies EGFR signaling and limits the response to EGFR-targeted inhibitors in triple-negative breast cancer cells. Sci. Signal. *6*, ra66.

Mishima, K., Higashiyama, S., Asai, A., Yamaoka, K., Nagashima, Y., Taniguchi, N., Kitanaka, C., Kirino, T., and Kuchino, Y. (1998). Heparin-binding epidermal growth factor-like growth factor stimulates mitogenic signaling and is highly expressed in human malignant gliomas. Acta Neuropathol. *96*, 322–328.

Ongusaha, P.P., Kwak, J.C., Zwible, A.J., Macip, S., Higashiyama, S., Taniguchi, N., Fang, L., and Lee, S.W. (2004). HB-EGF is a potent inducer of tumor growth and angiogenesis. Cancer Res. *64*, 5283–5290.

Ostrom, Q.T., Gittleman, H., Liao, P., Rouse, C., Chen, Y., Dowling, J., Wolinsky, Y., Kruchko, C., and Barnholtz-Sloan, J. (2014). CBTRUS Statistical Report: Primary Brain and Central Nervous System Tumors Diagnosed in the United States in 2007-2011. Neuro. Oncol. *16 Suppl 4*, iv1–iv63.

Ozawa, T., Riester, M., Cheng, Y.K., Huse, J., Squatrito, M., Helmy, K., Charles, N., Michor, F., and Holland, E.C. (2014). Most human non-GCIMP glioblastoma subtypes evolve from a common proneural-like precursor glioma. Cancer Cell *26*, 288–300.

Puschmann, T.B., Zandén, C., Lebkuechner, I., Philippot, C., De Pablo, Y., Liu, J., and Pekny, M. (2014). HB-EGF affects astrocyte morphology, proliferation, differentiation, and the expression of intermediate filament proteins. J. Neurochem. *128*, 878–889.

Ramnarain, D.B., Park, S., Lee, D.Y., Hatanpaa, K.J., Scoggin, S.O., Otu, H., Libermann, T. a, Raisanen, J.M., Ashfaq, R., Wong, E.T., et al. (2006). Differential gene expression analysis reveals generation of an autocrine loop by a mutant epidermal growth factor receptor in glioma cells. Cancer Res. *66*, 867–874.

Ray, K.C., Moss, M.E., Franklin, J.L., Weaver, C.J., Higginbotham, J.N., Song, Y., Revetta, F.L., Blaine, S. a, Bridges, L.R., Guess, K.E., et al. (2013). Heparin-binding epidermal growth factor-like growth factor eliminates constraints on activated Kras to promote rapid onset of pancreatic neoplasia. Oncogene *33*, 1–9.

Robinson, J.P., VanBrocklin, M.W., Guilbeault, a R., Signorelli, D.L., Brandner, S., and Holmen, S.L. (2010). Activated BRAF induces gliomas in mice when combined with Ink4a/Arf loss or Akt activation. Oncogene *29*, 335–344.

Robinson, J.P., Vanbrocklin, M.W., McKinney, A.J., Gach, H.M., and Holmen, S.L. (2011). Akt signaling is required for glioblastoma maintenance in vivo. Am. J. Cancer Res. *1*, 155–167.

Sato, S., Drake, A.W., Tsuji, I., and Fan, J. (2012). A potent anti-HB-EGF monoclonal antibody inhibits cancer cell proliferation and multiple angiogenic activities of HB-EGF. PLoS One *7*, e51964.

Vajkoczy, P., Knyazev, P., Kunkel, A., Capelle, H., Behrndt, S., von Tengg-Kobligk, H., Kiessling, F., Eichelsbacher, U., Essig, M., Read, T., et al. (2006). Dominant-negative inhibition of the Axl receptor tyrosine kinase suppresses brain tumor cell growth and invasion and prolongs survival. Proc. Natl. Acad. Sci. U. S. A. *103*, 5799–5804.

Verhaak, R.G.W., Hoadley, K. a, Purdom, E., Wang, V., Qi, Y., Wilkerson, M.D., Miller, C.R., Ding, L., Golub, T., Mesirov, J.P., et al. (2010). Integrated genomic analysis identifies clinically relevant subtypes of glioblastoma characterized by abnormalities in PDGFRA, IDH1, EGFR, and NF1. Cancer Cell *17*, 98–110.

Yotsumoto, F., Oki, E., Tokunaga, E., Maehara, Y., Kuroki, M., and Miyamoto, S. (2010). HB-EGF orchestrates the complex signals involved in triple-negative and trastuzumab-resistant breast cancer. Int. J. Cancer *127*, 2707–2717.

Zhang, Z., Lee, J.C., Lin, L., Olivas, V., Au, V., LaFramboise, T., Abdel-Rahman, M., Wang, X., Levine, A.D., Rho, J.K., et al. (2012). Activation of the AXL kinase causes resistance to EGFR-targeted therapy in lung cancer. Nat. Genet. *44*, 852–860.

Zheng, H., Ying, H., Yan, H., Kimmelman, A.C., Hiller, D.J., Chen, A.-J., Perry, S.R., Tonon, G., Chu, G.C., Ding, Z., et al. (2008). p53 and Pten control neural and glioma stem/progenitor cell renewal and differentiation. Nature *455*, 1129–1133.

Table 3.1 HBEGF is associated with decreased survival. Median survival of GBM patients from the TCGA dataset with or without upregulation of known EGFR ligands with associated logrank p-value from cBioPortal. The EGFR ligands listed are epidermal growth factor (EGF), heparin-binding EGF-like growth factor (HBEGF), transforming growth factor-alpha (TGFa), amphiregulin (AREG), betacellulin (BTC), epiregulin (EREG), and epigen (EPGN).

EGFR Ligands	Median Survival (months)		p-value
	with upregulation	without upregulation	
AREG	5.1	13.7	<0.01
BTC	9.9	13.4	0.97
EGF	10.6	13.4	0.81
EPGN	7.4	13.4	0.36
EREG	2.5	13.4	0.014
HBEGF	7.4	13.6	<0.01
TGFa	16.1	13.3	0.75

Table 3.2 Survival data for *in vivo* studies. Mean survival of TVA positive, tumor-bearing mice in three different strains of Nestin-TVA mice: *Ink4a/Arf*$^{lox/lox}$, *Pten*$^{lox/lox}$, and *Ink4a/Arf*$^{lox/lox}$;*Pten*$^{lox/lox}$ that have been injected with different combinations of RCAS viruses containing Cre, HBEGF or EGFR. E.E. denotes that all mice survived to the experimental endpoint (112 days). N/D denotes not done. No injected TVA negative mice developed tumors.

Genes Delivered	Mean Survival of Nestin-TVA Mice (days)		
	Ink4a/Arf$^{lox/lox}$	*Pten*$^{lox/lox}$	*Ink4a/Arf*$^{lox/lox}$;*Pten*$^{lox/lox}$
Cre	E.E.	E.E.	E.E.
HBEGF	E.E.	N/D	N/D
EGFR, Cre	E.E.	E.E	E.E.
HBEGF, Cre	68.5 ± 21.2	56.1 ± 11.8	28.7 ± 2.3
HBEGF, EGFR, Cre	76.5 ± 16.4	60.1 ± 16.7	32.3 ± 3.4

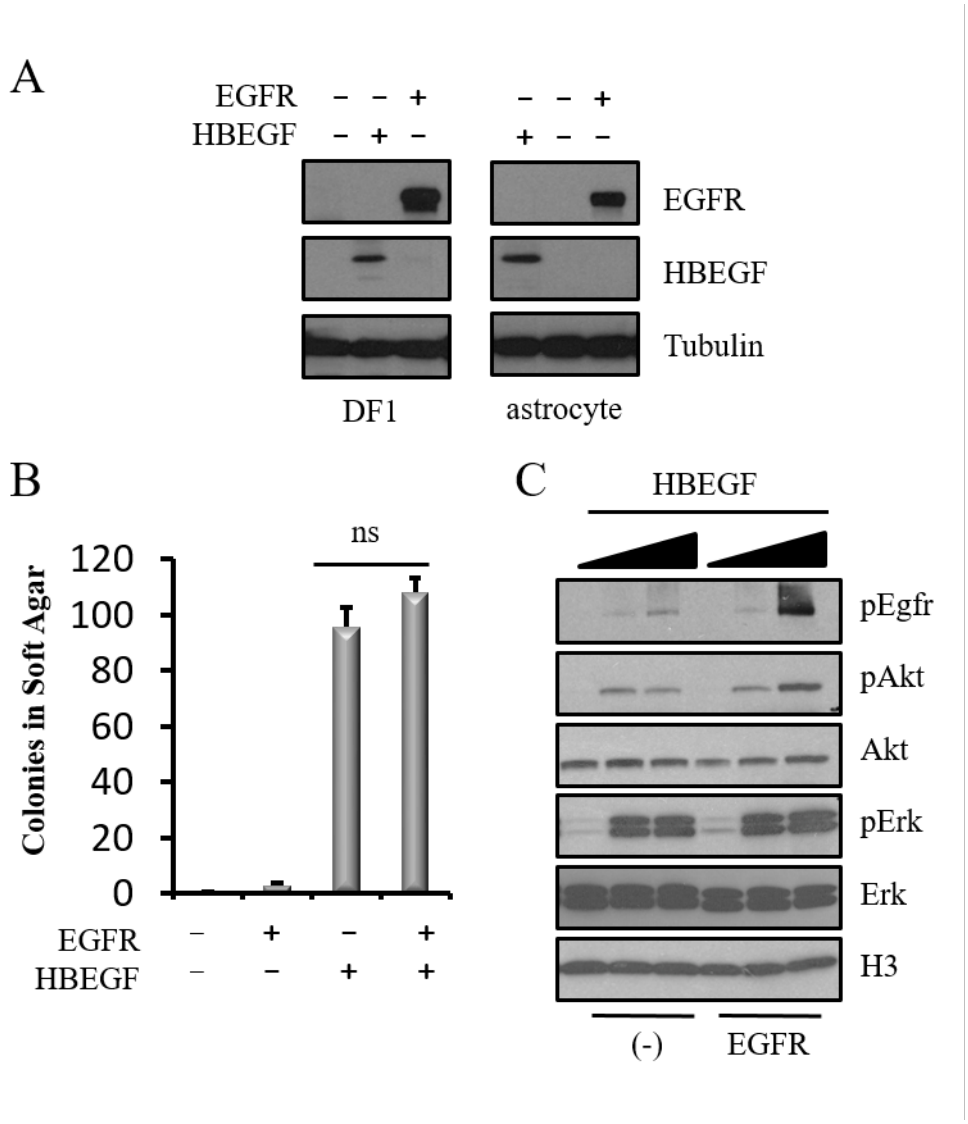

Figure 3.1 HBEGF promotes anchorage-independent growth of immortal astrocytes. **A:** Expression of EGFR and HBEGF in DF1 cells and Nestin-TVA*Ink4a/Arf*-null mouse astrocytes. **B:** Soft agar colony formation of *Ink4a/Arf*-null astrocytes expressing exogenous EGFR and/or HBEGF compared with RCAS-Cre infected control cells. Data are represented as mean ± S.E.M. **C:** Western blot analysis of downstream effector pathways in *Ink4a/Arf*-null astrocytes expressing either endogenous (-) or exogenous (EGFR). HBEGF was added to serum-free media at two different concentrations (0.5 ng/ml and 5.0 ng/ml).

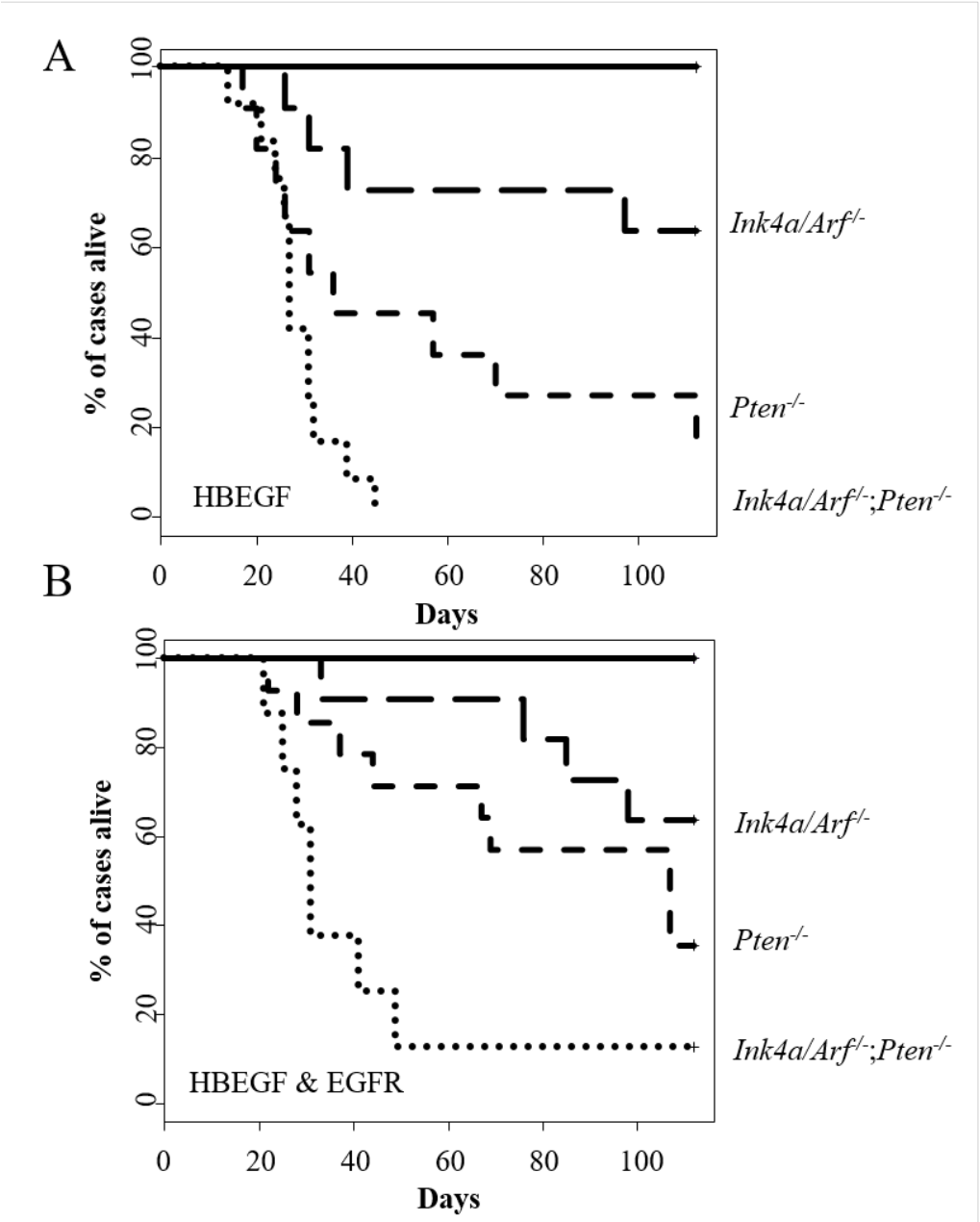

Figure 3.2 HBEGF cooperates with loss of *Ink4a/Arf* and *Pten* to promote glioma formation. A: Kaplan-Meier survival analysis of Nestin-TVA;*Ink4a/Arf*$^{lox/lox}$ (n = 11, long dash), Nestin-TVA;*Pten*$^{lox/lox}$ (n = 11, short dash), and Nestin-TVA;*Ink4a/Arf*$^{lox/lox}$;*Pten*$^{lox/lox}$ (n = 12, round dash) mice injected with viruses containing HBEGF and/or Cre was compared with injection of viruses containing HBEGF alone in Nestin-TVA;*Ink4a/Arf*$^{lox/lox}$ (n = 10, solid line) **B:** Kaplan-Meier survival analysis of Nestin-TVA;*Ink4a/Arf*$^{lox/lox}$ (n = 12, long dash), Nestin-TVA;*Pten*$^{lox/lox}$ (n = 12, short dash), and Nestin-TVA;*Ink4a/Arf*$^{lox/lox}$;*Pten*$^{lox/lox}$ (n = 12, round dash) mice injected with viruses containing HBEGF, EGFR, and Cre compared with injection of viruses containing Cre alone in all three strains (n = 33, solid line).

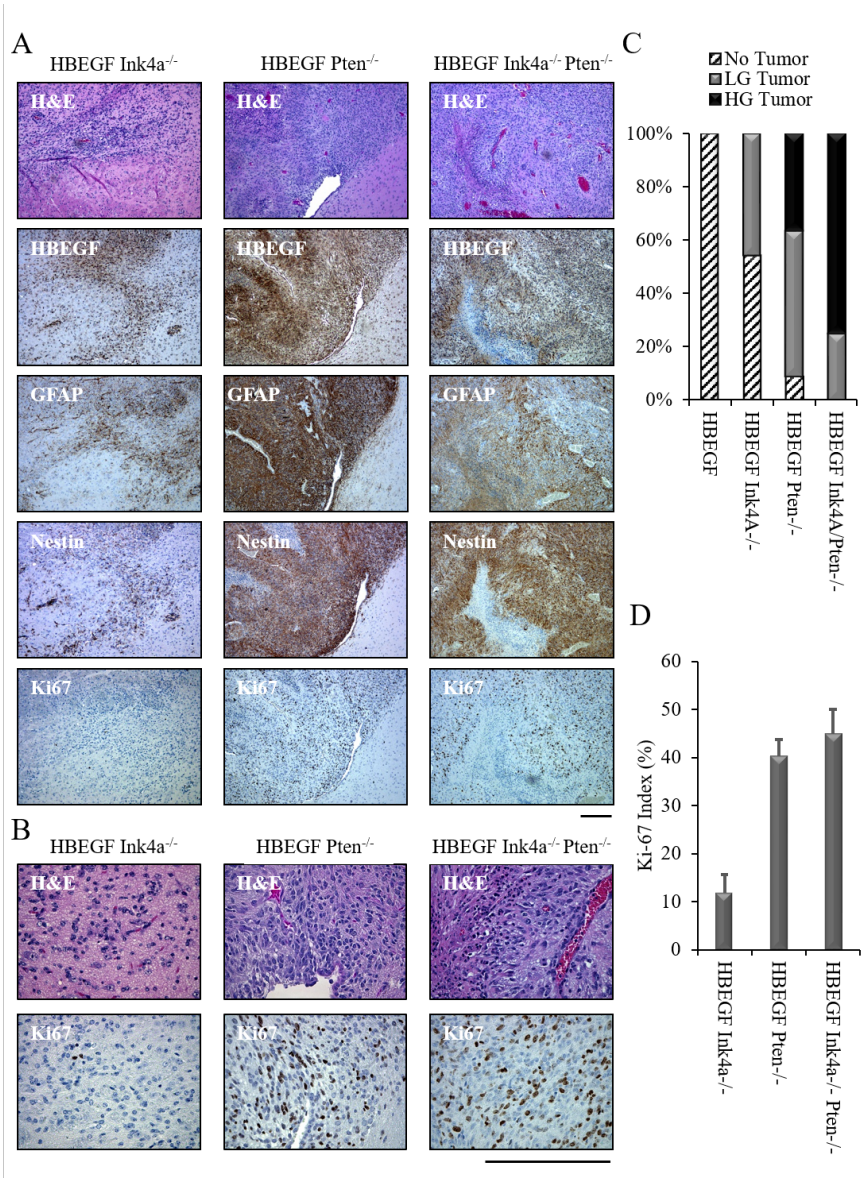

Figure 3.3 Histological examination of brain sections from injected mice. A: Representative H&E and HBEGF, GFAP, Nestin, and Ki67 immunohistochemistry images of HBEGF-driven tumors from each strain of mice injected with viruses containing HBEGF and Cre. Scale bar represents 300 μm. **B:** Representative high-power H&E and Ki67 images of HBEGF-driven tumors from each strain of mice injected with viruses containing HBEGF and Cre. Scale bar represents 300μm. **C:** Percentage of each tumor grade observed in Nestin-TVA;*Ink4a/Arf*$^{lox/lox}$, Nestin-TVA;*Pten*$^{lox/lox}$, and Nestin-TVA;*Ink4a/Arf*$^{lox/lox}$;*Pten*$^{lox/lox}$ mice injected with viruses containing HBEGF alone or in combination with Cre. Low grade (LG) tumors were characterized by nuclear atypia and pleomorphism while high grade tumors (HG) were characterized by the presence of necrosis, vascular proliferation, and mitotic figures. **D.** Quantification of Ki-67 proliferation index for HBEGF-driven tumors. For each tumor, the average of four high-power fields is shown. Data are represented as mean percentage ± S.E.M.

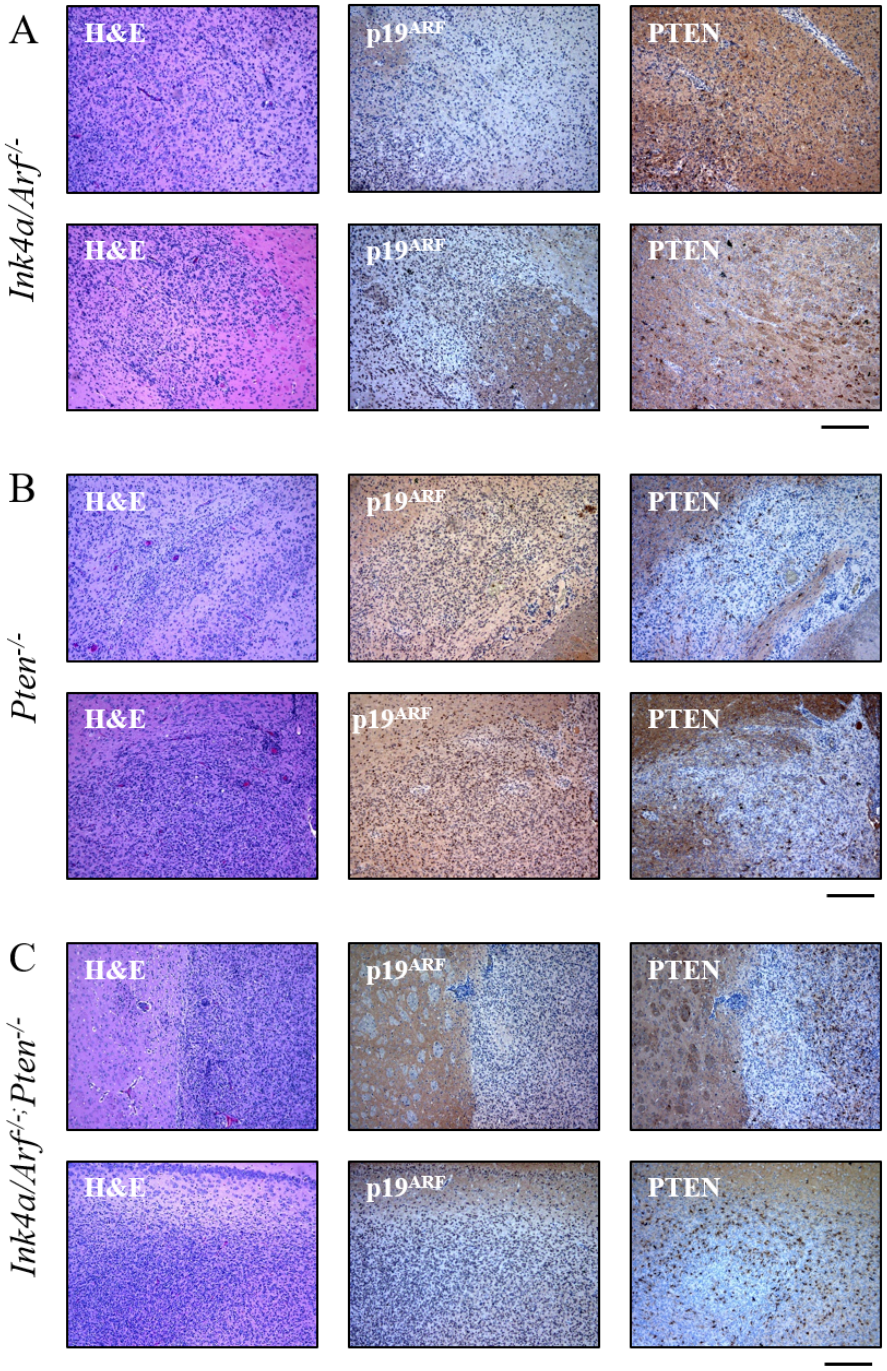

Figure 3.4 Confirmation of Ink4a/Arf and Pten loss in tumors following delivery of Cre. Viral delivery and expression of Cre recombinase was confirmed by immunohistochemistry using antibodies against $p19^{Arf}$ and Pten in tumors induced with with RCAS-HBEGF and RCAS-Cre in **A**: Nestin-TVA;*Ink4a/Arf*$^{lox/lox}$ mice **B:** Nestin-TVA;*Pten*$^{lox/lox}$ mice, and **C:** Nestin-TVA;*Ink4a/Arf*$^{lox/lox}$;*Pten*$^{lox/lox}$ mice. Scale bar represents 300 μm.

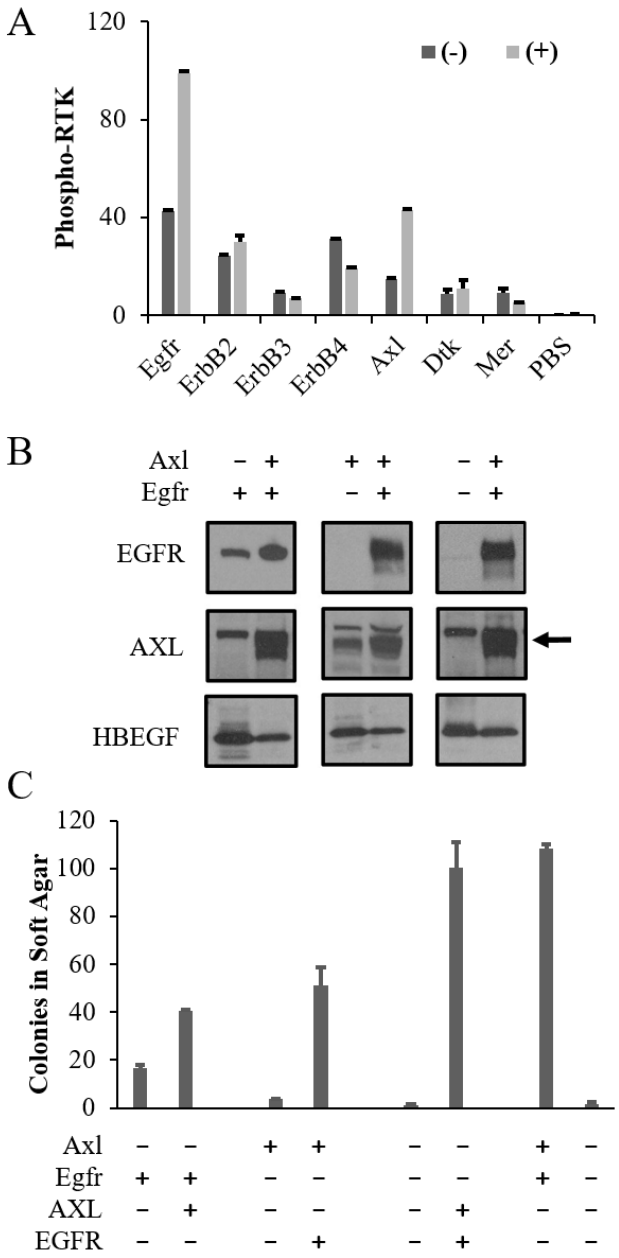

Figure 3.5 Both Egfr and Axl mediate HBEGF signaling. A: Phosphorylation of multiple RTKs was simultaneously assayed in isogenic astrocytes in the presence (+) or absence (-) of HBEGF. A subset of RTKs analyzed representing the ErbB and TAM family members are shown. Data are represented as mean ± S.E.M. **B.** Endogenous Axl and/or Egfr expression was eliminated using CRISPR-mediated gene editing (-) in Nestin-TVA;*Ink4a/Arf*-null astrocytes . Human AXL and EGFR were expressed following RCAS-mediated infection for rescue (+). The arrow represents the AXL band. **C.** Astrocytes from B were assayed for soft-agar colony formation to determine the functional significance of Axl and Egfr loss. Data are represented as mean ± S.E.M.

A

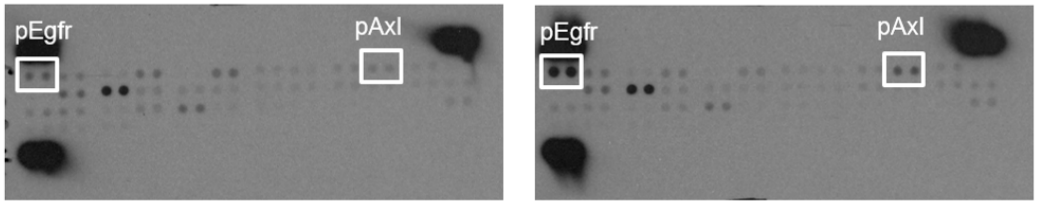

(-) HBEGF (+) HBEGF

B

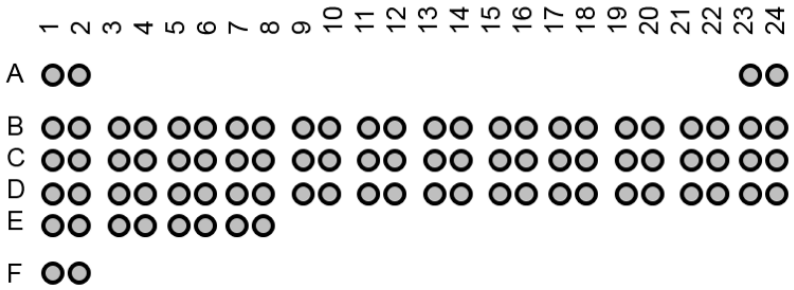

C

Coord.	RTK/Control	Coord.	RTK/Control	Coord.	RTK/Control
A1, 2, 23, 24	+ Control	D7, 8	VEGFR3	C3, 4	MSPR
B1, 2	EGFR	D9, 10	MUSK	C5, 6	PDGFRA
B3, 4	ERBB2	D11, 12	EPHA1	C7, 8	PDGFRB
B5, 6	ERBB3	D13, 14	EPHA2	C9, 10	SCFR
B7, 8	ERBB4	D15, 16	EPHA3	C11, 12	FLT-3
B9, 10	FGFR2	D17, 18	EPHA6	C13, 14	M-CSFR
B11, 12	FGFR3	D19, 20	EPHA7	C15, 16	C-RET
B13, 14	FGFR4	D21. 22	EPHA8	C17, 18	TIE1
B15, 16	IR	D23, 24	EPHB1	C19, 20	TIE2
B17, 18	IGF-1R	E1, 2	EPHB2	C21, 22	TRKA
B19, 20	AXL	E3, 4	EPHB4	C23, 24	TRKB
B21, 22	DTK	E5, 6	EPHB6	D1, 2	TRKC
B23, 24	MER	E7, 8	- control	D3, 4	VEGFR1
C1, 2	HGFR	F1, F2	+ control	D5, 6	VEGFR2

Figure 3.6 HBEGF activates Egfr and Axl. A: Isogenic astrocytes in the presence (+) or absence (-) of HBEGF were assayed for phosphorylation of different RTKs in parallel. Increased phosphorylation in the presence of HBEGF was only seen for Egfr (B1,B2) and Axl (B19, B20). **B.** Coordinates for the RTK arrays shown in A. **C**. Key for the different RTKs corresponding to the coordinates shown in B.

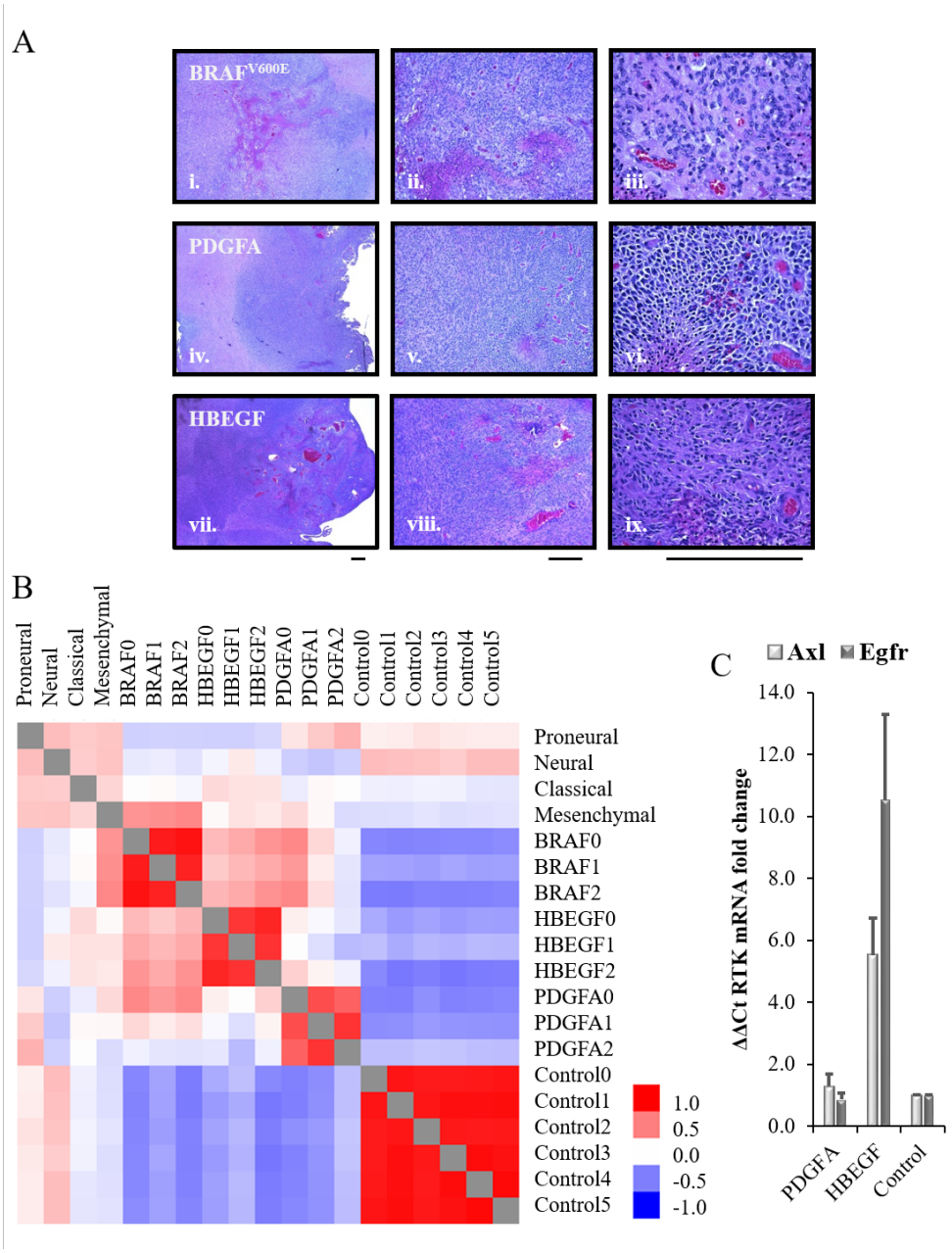

Figure 3.7 Molecular comparison between mouse and human GBM. A: Representative H&E sections for high-grade gliomas derived in the Nestin-TVA;*Ink4a/Arf*$^{lox/lox}$;*Pten*$^{lox/lox}$ mouse model using RCAS-Cre and three different drivers: BRAF^{V600E}(i., ii., iii.), PDGFA (iv., v., vi.), and HBEGF (vii., viii., ix.) showing 4x, 10x and 40x magnification, respectively. Scale bar represents 300µm. **B:** Heatmap showing Pearson correlations between the TCGA subtypes (proneural, neural, classical, mesenchymal) and high-grade mouse gliomas driven by RCAS-BRAF^{V600E}, PDGFA, and HBEGF in the absence of Ink4a/Arf and Pten. **C**: Real-time PCR analysis of Axl, Egfr, Pdgfra mRNA levels in either HBEGF or PDGFA tumors. Rn18s was used as an endogenous reference. Relative quantification was carried out using the comparative Ct method with TVA negative injected controls.

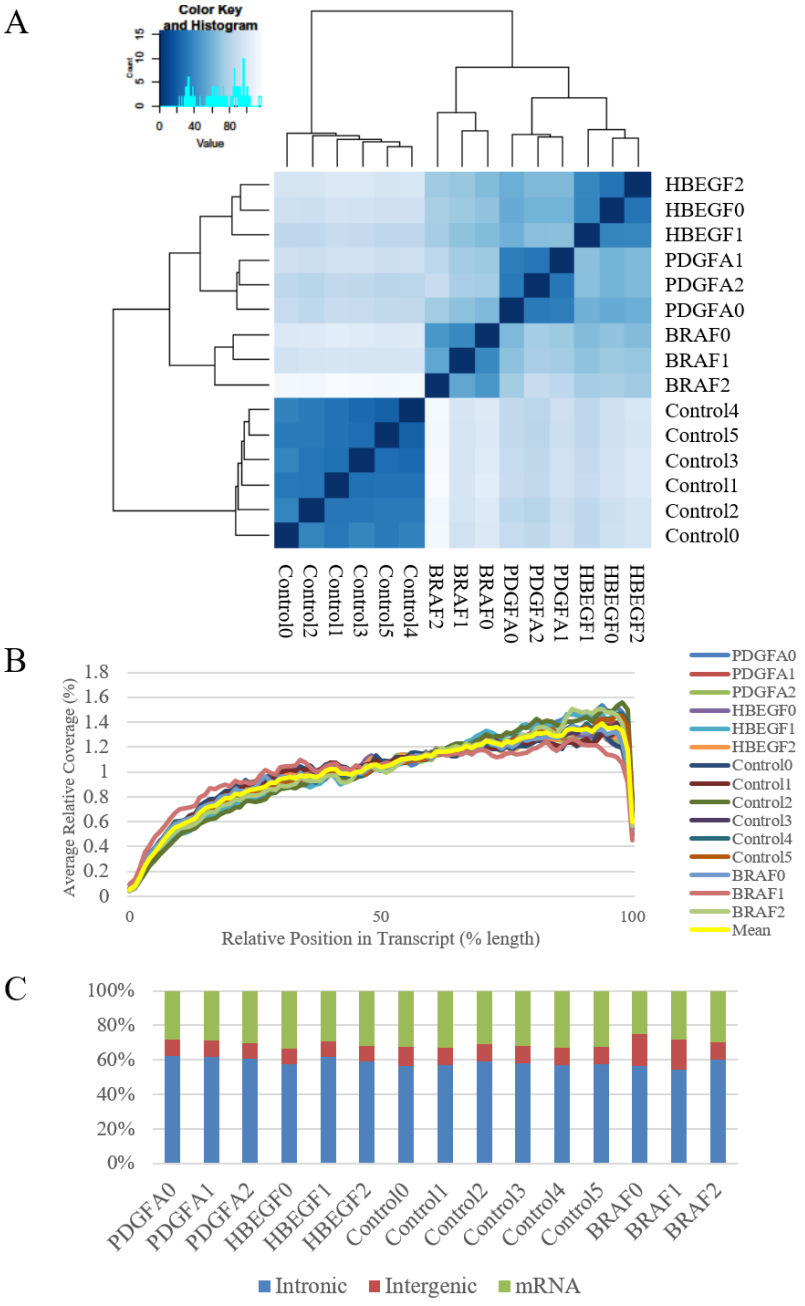

Figure 3.8 RNA-Seq Metrics. A: Cluster heatmap for intrasample variability displayed as a distance matrix based on raw counts from individual samples generated with the USeq package Defined Region Differential Seq (DRDS). High-grade gliomas derived in the Nestin-TVA;*Ink4a/Arf*$^{lox/lox}$;*Pten*$^{lox/lox}$ mouse model using RCAS-Cre and three different drivers: BRAF^{V600E}, PDGFA, and HBEGF were compared to TVA negative controls. **B:** 5′ to 3′ coverage for all transcripts calculated with the Picard tool, CollectRNASeqMetrics. **C:** Proportion of reads mapping to intronic, intergenic, and mRNA also from the Picard tool, CollectRNASeqMetrics.

A

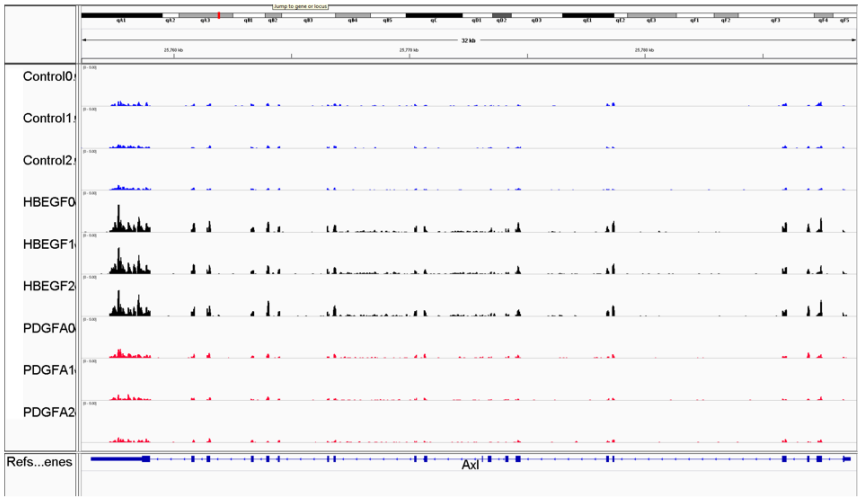

B

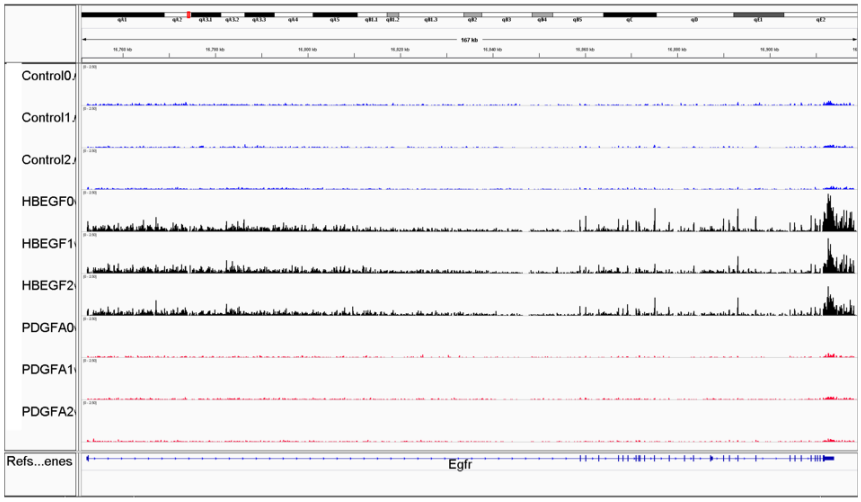

C

Axl	Log 2 ratio	Fold change	FDR
PDGFA vs Control	0.29	1.23x	5.83
HBEGF vs Control	1.85	3.61x	148.74

Egfr	Log 2 ratio	Fold change	FDR
PDGFA vs Control	-0.39	0.76x	15.12
HBEGF vs Control	2.92	7.58x	735.50

Figure 3.9 RNA-Seq read coverage data for HBEGF and PDGFA driven tumors. **A:** Relative transcript levels for Axl across three replicates of healthy TVA negative controls, three HBEGF-driven tumors, and three PDGFA-driven tumors derived in the Nestin-TVA;*Ink4a/Arf*$^{lox/lox}$;*Pten*$^{lox/lox}$ mouse model. RNA sequencing read coverage was generated from the USeq utility Sam 2 USeq and visualized with the Integrative Genomics Viewer. **B:** Same as in A but for Egfr. **C:** Fold change in Axl and Egfr transcript comparing tumor samples to healthy controls from RNA sequencing. Log2 ratios were calculated from the combined replicates. FDR is a log transformed p-value from DRDS, where the p value has been adjusted for multiple testing. A FDR >30 is considered very significant.

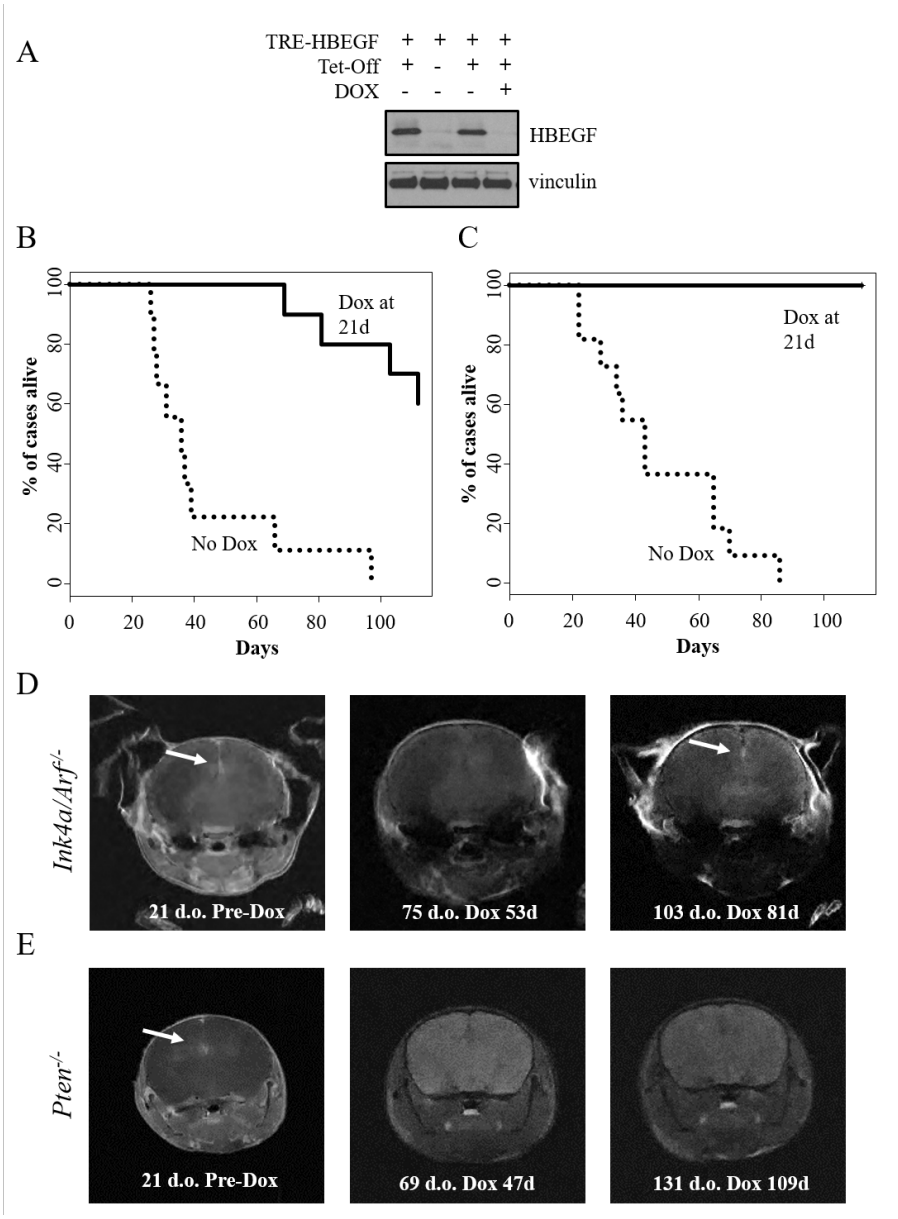

Figure 3.10 Suppression of HBEGF expression *in vitro* and *in vivo*. A: Western blot of isogenic astrocytes infected with TRE-HBEGF and/or tet-off with or without 2 µg/ml of doxycycline for 72 h. **B:** Kaplan-Meier survival analysis of tumor-bearing Nestin-TVA;*Ink4a/Arf*$^{lox/lox}$ injected with RCAN-TRE-HBEGF, RCAS-tet-off, and RCAS-Cre that were not treated (n = 9, round dash) and treated starting at 21 days of age (n = 21, solid line). **C:** Same as in B but for Nestin-TVA;*Pten*$^{lox/lox}$ injected with RCAN-TRE-HBEGF, RCAS-tet-off, and RCAS-Cre (n = 11, round dash) (n=21, solid line). **D:** MRI showing initial regression of RCAN-TRE-HBEGF tumors in Nestin-TVA;*Ink4a/Arf*$^{lox/lox}$ mice after doxycycline treatment starting at 21 days of age and subsequent resistant tumors at 103 days of age. The abbreviation d.o. represents days old. **E:** MRI showing initial regression of RCAN-TRE-HBEGF tumors in Nestin-TVA;*Pten*$^{lox/lox}$ mice after doxycycline treatment starting at 21 days of age and no evidence of disease at 131 days of age.

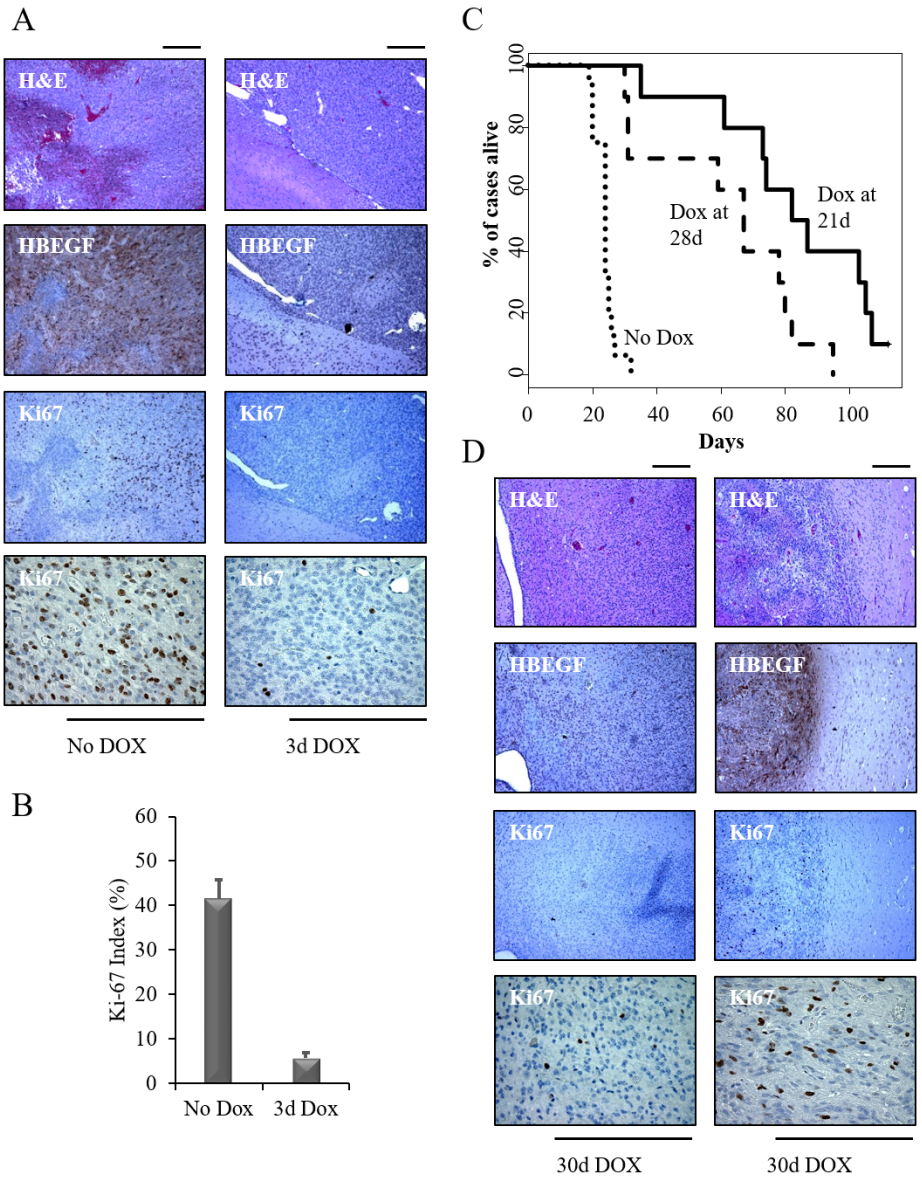

Figure 3.11 Suppression of HBEGF expression prolongs survival *in vivo*. A: Immunohistochemical analysis of HBEGF and Ki67 in brain tissue isolated from Nestin-TVA;*Ink4a/Arf*$^{lox/lox}$;*Pten*$^{lox/lox}$ mice injected with RCAN-TRE-HBEGF, RCAS-tet-off, and RCAS-Cre that were either untreated or treated with doxycycline for 3 days. Scale bar represents 300 µm. **B:** The Ki67 staining was quantified using two representative tumors for each cohort. For each tumor, the average of four high-power fields is shown. Data are represented as mean ± S.E.M. **C:** Kaplan-Meier survival analysis of Nestin-TVA;*Ink4a/Arf*$^{lox/lox}$;*Pten*$^{lox/lox}$ injected with RCAN-TRE-HBEGF, RCAS-tet-off, and RCAS-Cre that were not treated (n = 16, round dash), treated starting at 21 days of age (n = 10, solid line), or treated starting at 28 days of age (n = 10, short dash). **D:** Immunohistochemical analysis of regressed tumors using antibodies against HBEGF and Ki67 with corresponding H&E. Scale bar represents 300 µm.

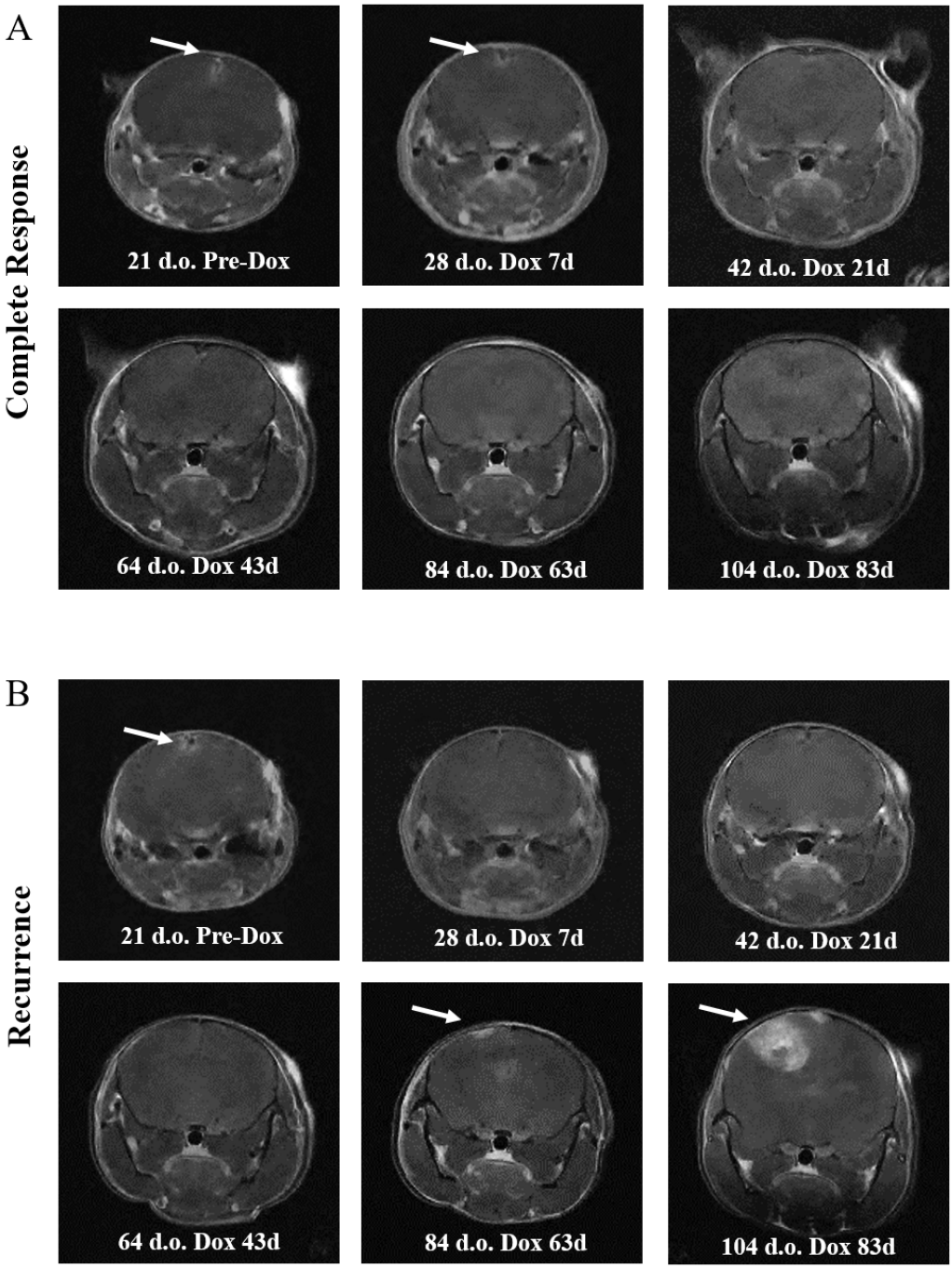

Figure 3.12 MRI analysis. A: MRI showing regression of RCAN-TRE-HBEGF tumors in Nestin-TVA;*Ink4a/Arf*$^{lox/lox}$;*Pten*$^{lox/lox}$ mice after doxycycline treatment starting at 21 days of age and no evidence of disease at 104 days of age. The abbreviation d.o. represents days old. **B:** MRI from a mouse showing a tumor at 21 days of age, followed by initial regression at 28 days of age, and subsequent recurrent tumor at 104 days of age.

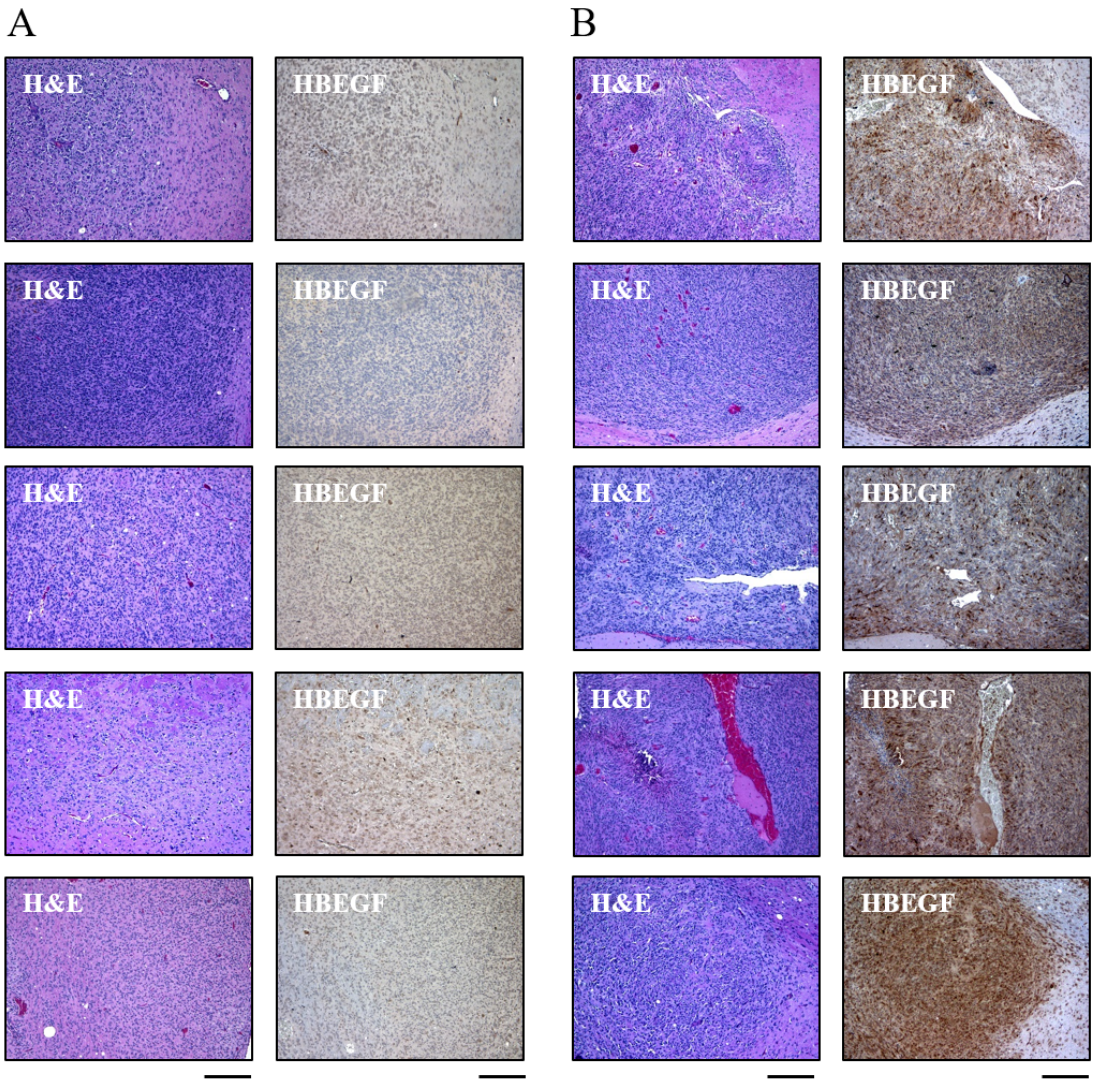

Figure 3.13 HBEGF expression in regressed tumors. A: Immunohistochemical analysis of regressed tumors using an antibody against HBEGF for Nestin-TVA;*Ink4a/Arf*$^{lox/lox}$;*Pten*$^{lox/lox}$ injected with RCAN-TRE-HBEGF, RCAS-tet-off, and RCAS-Cre that were doxycycline treated. These regressed tumors showed no HBEGF expression. **B:** Same as in A but for tumors that re-expressed HBEGF. Scale bar represents 300 μm.

CHAPTER 4

CONCLUSION

4.1 Chapter Summaries

In Chapter 2, the tumorigenic properties of the BRAF fusion genes observed in 80% of pilocytic astrocytomas were shown to be due to the C-terminal kinase domain (Jones et al., 2009). This finding is supported by *in vitro* functional data in colony formation assays of Nestin-TVA mouse astrocytes. When astrocytes expressing the BRAF kinase domain were injected orthotopically in syngeneic mice, highly cellular and invasive gliomas that lacked malignant properties such as necrosis and endothelial hyperplasia were observed. As a complementary approach, the BRAF kinase domain was delivered with the RCAS retrovirus allowing for somatic cell gene transfer into TVA-expressing neural progenitor cells *in vivo*. All of the mice lived to the experimental endpoint of 12 weeks. Histological analysis of brain tissue from these mice revealed tumors in 21% of the mice in the context of *Ink4a/Arf* loss. These tumors were well circumscribed and had a lower mitotic index compared to tumors driven by expression of full-length $BRAF^{V600E}$ (Robinson et al., 2010). These results establish that the BRAF-KD alone can cooperate with *Ink4a/Arf* loss to drive gliomagenesis *in vivo* and that the transforming properties of the different BRAF fusion genes lie within the kinase domain of BRAF. Thus the N-terminal portion of the fusions such as FAM131b, SRGAP3, and KIAA1549 likely function to direct expression to the

appropriate cells in the brain. As $BRAF^{V600E}$ inhibitors activate rather than inhibit the BRAF fusion genes, combined MEK and PI3K/mTOR inhibition was used and showed great efficacy in astrocytes expressing the BRAF kinase domain in nanomolar concentrations. This is a marked improvement over the 10μM concentration needed for the second-generation BRAF inhibitors (Sievert et al., 2013).

In Chapter 3, HBEGF, which is co-expressed with EGFR in a subset of malignant gliomas, was demonstrated to promote the development of gliomas of varying grades in a context-specific manner (Mishima et al., 1998; Ramnarain et al., 2006). In immortalized but nontransformed mouse astrocytes, expression of activated HBEGF led to the formation of colonies in soft agar. Using the RCAS-TVA system, expression of HBEGF in *Ink4a/Arf*-deficient mice led to the formation of low-grade gliomas with a penetrance of 54%. When HBEGF was expressed in a *Pten*-deficient background, high-grade tumors were observed with an overall glioma penetrance of 90%. Co-expressing exogenous EGFR did not impact colony formation *in vitro* or tumor formation *in vivo*, so the possibility of alternative signaling pathways was pursued. Using a proteome profiler, activation of *Axl* in mouse astrocytes expressing HBEGF was discovered, and the functional significance of this activation was confirmed through CRISPR-mediated gene editing. Using RNA sequencing and qPCR, we discovered that *Egfr* and *Axl* are transcriptionally upregulated by HBEGF. This likely explains why exogenous EGFR was redundant in this context.

Expression profiling of the HBEGF tumors was done in conjunction with the RCAS-TVA glioma models for PDGFA and $BRAF^{V600E}$. These tumors were then compared to the TCGA subtypes (Ozawa et al., 2014; Robinson et al., 2010; Verhaak et al., 2010). The $BRAF^{V600E}$, PDGFA, and HBEGF-driven tumors resembled most closely

the mesenchymal, proneural, and classical subtypes, respectively. In addition, the healthy control samples derived from injected TVA-negative mice showed similarities to the neural subtype, which is defined by the expression of neuronal markers. With the validation of the role of HBEGF in the initiation of gliomas, a tetracycline-inducible model for HBEGF in tumor maintenance was developed. In the context of *Pten* loss, no resistant tumors developed by the standard 16-week endpoint in the absence of HBEGF expression. In contrast, in the context of *Ink4a/Arf* loss, resistant tumors were observed, suggesting that *Ink4a/Arf* loss promotes tumor recurrence following HBEGF inhibition.

4.2 Preview of Appendices

Appendix A concerns the analysis of the HBEGF-driven tumors that were co-injected with a functional *EGFR* receptor. If *EGFR* were critical for gliomagenesis in this context, we would have expected to observe exogenous *EGFR* expression in the majority of the tumors. As virally delivered EGFR is HA epitope-tagged, it could be distinguished from endogenously expressed Egfr using immunohistochemistry. We observed that 57% (4 / 7) of *Ink4a/Arf*-deficient tumors, 60% (3 / 5) of *Pten*-deficient tumors, and 28% (2 / 7) of *Ink4a/Arf*- and *Pten*-deficient tumors expressed exogenous EGFR. In Chapter 3, survival of mice injected with HBEGF and mice injected with both HBEGF and EGFR were compared, but no significant difference was observed. Loss of *Ink4a/Arf* and *Pten* with EGFR overexpression did not result in tumor formation. With HBEGF co-overexpression, exogenous EGFR expression was detected in some of the tumors, but the latency of these tumors was not different from those that only expressed endogenous levels of Egfr.

Appendix B is also an ancillary study from the work done in Chapter 3 about

evaluating the role of AXL in HBEGF signaling. As observed with EGFR co-expression, co-expression of AXL in HBEGF-driven tumors did not affect survival. AXL was also C-terminally tagged with HA, and 40% (2 / 5) of *Ink4a/Arf*-deficient tumors, 12% (1 / 8) of *Pten*-deficient tumors, and 41% (5 / 12) of *Ink4a/Arf*- and *Pten*-deficient tumors were found to express virally delivered AXL. With the caveat of relatively small numbers in each cohort, it appears that the selection pressure for expression of exogenous EGFR in HBEGF-driven tumors is stronger than that for AXL. In addition, EGFR was expressed the highest in *Ink4a/Arf*-deficient tumors, which were lower grade gliomas, while AXL was expressed the highest in *Ink4a/Arf*- and *Pten*-deficient tumors, which were higher grade gliomas. The expression of exogenous AXL in these tumors as well as preliminary co-immunoprecipitation data support the role of AXL in HBEGF-mediated signaling outlined in Chapter 3. However, as observed for EGFR, the latency of these tumors was not different from those that only expressed endogenous levels of Axl.

Appendix C describes unpublished data with the role of PDGFA in gliomagenesis. *In vitro* studies were carried out in PDGFA-expressing astrocytes similar to the work done with HBEGF. Interestingly, when the investigation shifted towards *in vivo* work, it was found that PDGFA alone was sufficient to initiate gliomas and that loss of *Ink4a/Arf* or *PTEN* did not significantly affect gliomagenesis. The sufficiency of PDGFA alone was more apparent when its cognate receptor PDGFRA was co-injected, as the addition of PDGFRA actually increased survival. When expression of PDGFRA was assessed in all mice that were co-injected with PDGFA and PDGFRA, 29% (10 / 34) showed strong staining. Furthermore, the tumors that were positive for exogenous PDGFRA expression had increased tumor latency compared to tumors that only expressed exogenous PDGFRA.

Appendix D outlines ongoing work to develop an inducible model for $BRAF^{V600E}$-driven gliomas. Several attempts in the lab previously failed to produce viable virus that could confer expression of full-length mutant BRAF. It was suspected that the size of BRAF was too large to fit into the retrovirus capsid, so a lentiviral vector approach was pursued. This led to the creation of the TzTOC-$BRAF^{V600E}$ vector, which contains two independent promoters. The tetracycline-responsive promoter controls expression of mutant BRAF while a separate CMV promoter controls expression of the tetracycline transactivator, tet-off, and Cre recombinase. Although the vector worked *in vitro* and *in vivo*, an alternative approach was sought because of low penetrance and the long latency of tumor formation. The tumors derived through the lentiviral TzTOC vector were confirmed to express mutant BRAF. Currently, a new RCAN vector with a modified, shorter tet-responsive element is being utilized with promising *in vitro* results. Mice are currently being bred to do the *in vivo* validation.

4.3 Perspectives for Future Work

The work presented in the previous chapters outlines an investigation of two oncogenic drivers, BRAF and HBEGF, with a thorough characterization of key tumor suppressors that cooperate with these drivers to induce gliomas *in vivo*. Exciting work remains in the potential therapeutic applications for these tumors that will hopefully impact the treatment of patients.

In the inducible HBEGF model, there are still doxycycline-responsive tumors at 6 months. These are the same mice in the 60% of responders that were reported in chapter 3. In addition, none of the *Pten*-deficient tumors have recurred. These mice will be monitored

further with longitudinal MRI scans for evidence of tumor recurrence. For the tumors that have recurred, future work will be directed at elucidating the mechanism of resistance using both candidate and unbiased approaches.

As most pilocytic astrocytomas do not contain *Ink4a/Arf* loss, it would be worthwhile to derive tumors with intact *Ink4a/Arf*. No tumors were seen within the 12-week period, so an extension of the experimental endpoint would be the next logical step. In addition, a continuation of the validation of targeting the kinase domain of BRAF with MEK and PI3K inhibitors *in vivo* would be another exciting future direction.

4.4 Conclusion

The main focus of the Holmen lab is to define essential targets for human cancers through the development of preclinical mouse models. In line with this goal, the work in this dissertation investigates the role of mutant BRAF and HBEGF in the initiation and maintenance of gliomas using an *in vivo* model. The essential role of the kinase domain of BRAF was defined using both a transplantation model of astrocytes as well as a somatic cell gene transfer system, which afforded the use of MEK and PI3K inhibition as candidate therapy. Using those same tools, the role of HBEGF in glioma formation was also investigated. The use of CRISPR-mediated gene editing, RTK proteomics, and RNA sequencing defined a novel involvement of AXL in HBEGF-mediated signaling that has therapeutic implications. With an inducible model of HBEGF gliomagenesis, a new target for therapy was validated that could prove useful in the future management of malignant gliomas.

4.5 References

Jones, D.T.W., Kocialkowski, S., Liu, L., Pearson, D.M., Ichimura, K., and Collins, V.P. (2009). Oncogenic RAF1 rearrangement and a novel BRAF mutation as alternatives to KIAA1549:BRAF fusion in activating the MAPK pathway in pilocytic astrocytoma. Oncogene *28*, 2119–2123.

Mishima, K., Higashiyama, S., Asai, A., Yamaoka, K., Nagashima, Y., Taniguchi, N., Kitanaka, C., Kirino, T., and Kuchino, Y. (1998). Heparin-binding epidermal growth factor-like growth factor stimulates mitogenic signaling and is highly expressed in human malignant gliomas. Acta Neuropathol. *96*, 322–328.

Ozawa, T., Riester, M., Cheng, Y.K., Huse, J., Squatrito, M., Helmy, K., Charles, N., Michor, F., and Holland, E.C. (2014). Most human non-GCIMP glioblastoma subtypes evolve from a common proneural-like precursor glioma. Cancer Cell *26*, 288–300.

Ramnarain, D.B., Park, S., Lee, D.Y., Hatanpaa, K.J., Scoggin, S.O., Otu, H., Libermann, T. a, Raisanen, J.M., Ashfaq, R., Wong, E.T., et al. (2006). Differential gene expression analysis reveals generation of an autocrine loop by a mutant epidermal growth factor receptor in glioma cells. Cancer Res. *66*, 867–874.

Robinson, J.P., VanBrocklin, M.W., Guilbeault, a R., Signorelli, D.L., Brandner, S., and Holmen, S.L. (2010). Activated BRAF induces gliomas in mice when combined with Ink4a/Arf loss or Akt activation. Oncogene *29*, 335–344.

Sievert, A.J., Lang, S., Katie, L., Madsen, P.J., Slaunwhite, E., Choudhari, N., Kellet, M., Storm, P.B., Resnick, A.C., Kjetland, E.F., et al. (2013). Paradoxical activation and RAF inhibitor resistance of BRAF protein kinase fusions characterizing pediatric astrocytomas. Proc. Natl. Acad. Sci. *110*, 8750–8750.

Verhaak, R.G.W., Hoadley, K. a, Purdom, E., Wang, V., Qi, Y., Wilkerson, M.D., Miller, C.R., Ding, L., Golub, T., Mesirov, J.P., et al. (2010). Integrated genomic analysis identifies clinically relevant subtypes of glioblastoma characterized by abnormalities in PDGFRA, IDH1, EGFR, and NF1. Cancer Cell *17*, 98–110.

APPENDIX A

EXPRESSION OF EGFR IN HBEGF-DRIVEN TUMORS

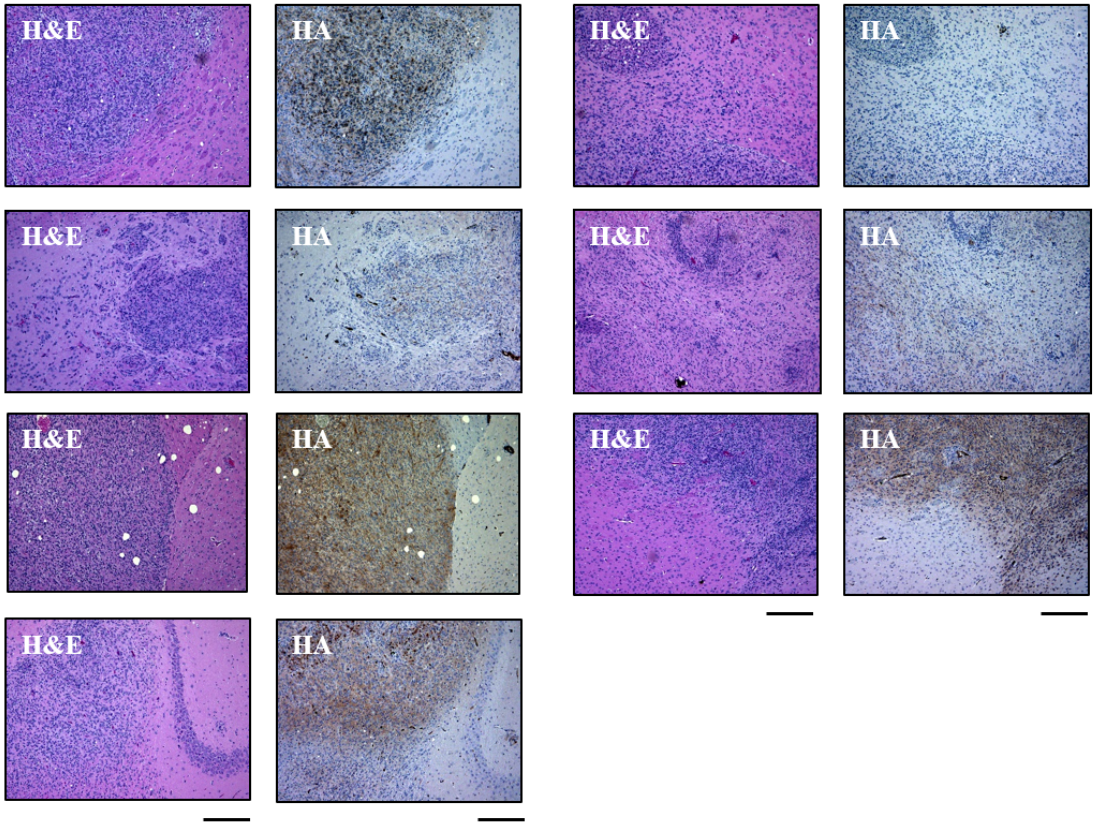

Figure A.1 Expression of EGFR in HBEGF-driven tumors in the context of *Ink4a/Arf* loss. Representative H&E and HA immunohistochemistry images of HBEGF-driven tumors in Nestin-TVA;*Ink4a/Arf*$^{lox/lox}$ mice injected with viruses containing HBEGF, Cre, and HA-tagged EGFR. Scale bars represent 300 μm.

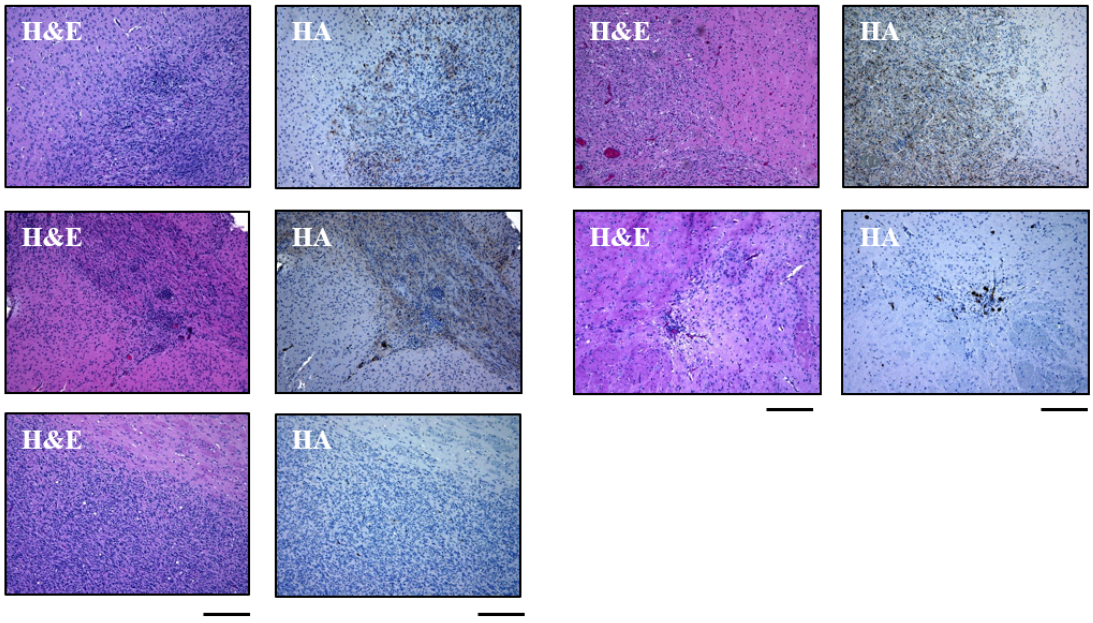

Figure A.2 Expression of EGFR in HBEGF-driven tumors in the context of *Pten* loss. Representative H&E and HA immunohistochemistry images of HBEGF-driven tumors in Nestin-TVA;*Pten*$^{lox/lox}$ mice injected with viruses containing HBEGF, Cre, and HA-tagged EGFR. Scale bars represent 300 μm.

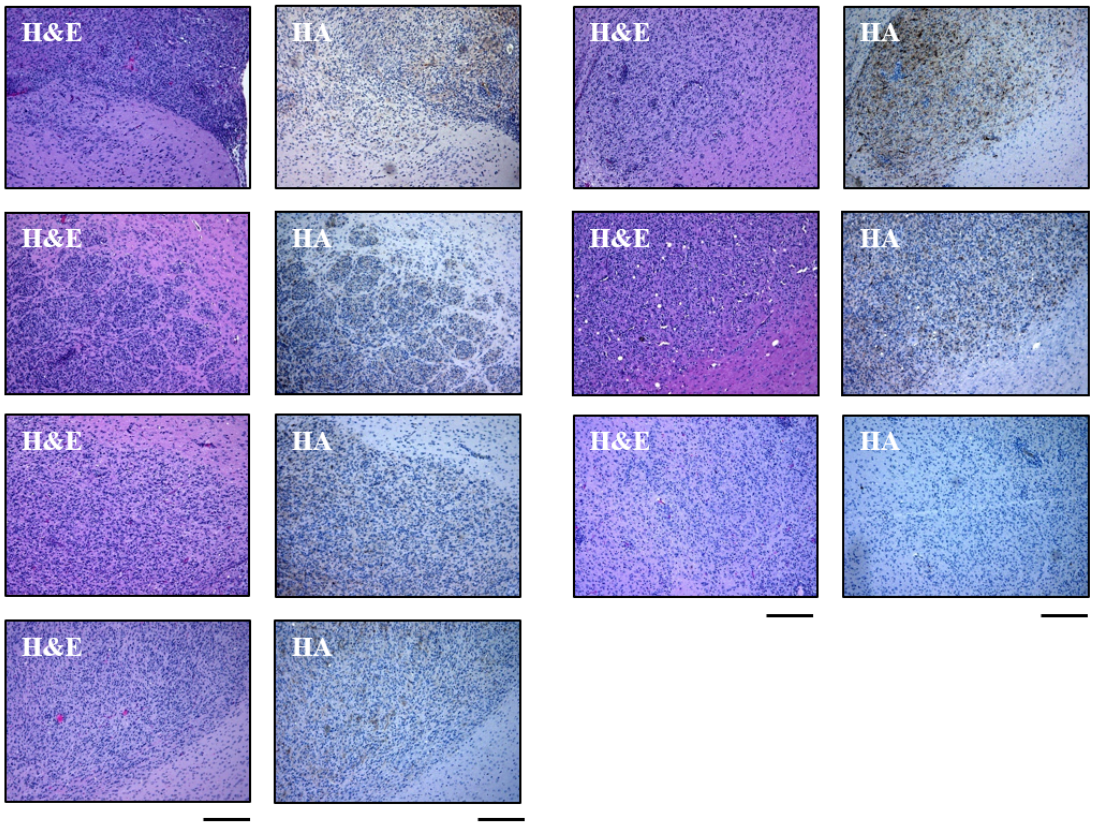

Figure A.3 Expression of EGFR in HBEGF-driven tumors in the context of *Ink4a/Arf* and *Pten* loss. Representative H&E and HA immunohistochemistry images of HBEGF-driven tumors in Nestin-TVA;*Ink4a/Arf*$^{lox/lox}$;*Pten*$^{lox/lox}$ mice injected with viruses containing HBEGF, Cre, and HA-tagged EGFR. Scale bars represents 300 μm.

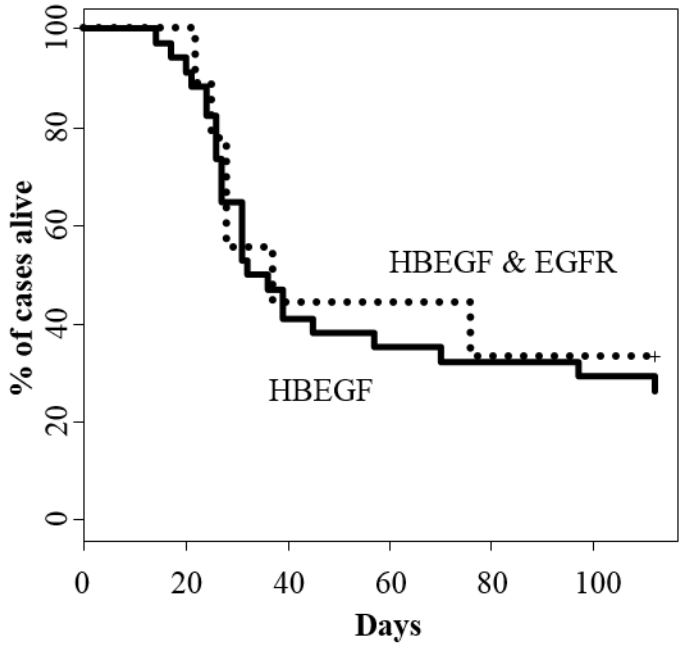

Figure A.4 Comparison of HBEGF-driven tumors with and without exogenous EGFR expression. Kaplan-Meier survival analysis of Nestin-TVA;*Ink4a/Arf*$^{lox/lox}$, Nestin-TVA;*Pten*$^{lox/lox}$, and Nestin-TVA;*Ink4a/Arf*$^{lox/lox}$; *Pten*$^{lox/lox}$ mice injected with viruses containing HBEGF, EGFR, and Cre with confirmed expression of exogenous EGFR (n = 9, round dash) compared with injection of viruses containing HBEGF and Cre alone (n = 34, solid line, $P = 0.748$).

APPENDIX B

EXPRESSION OF AXL IN HBEGF-DRIVEN TUMORS

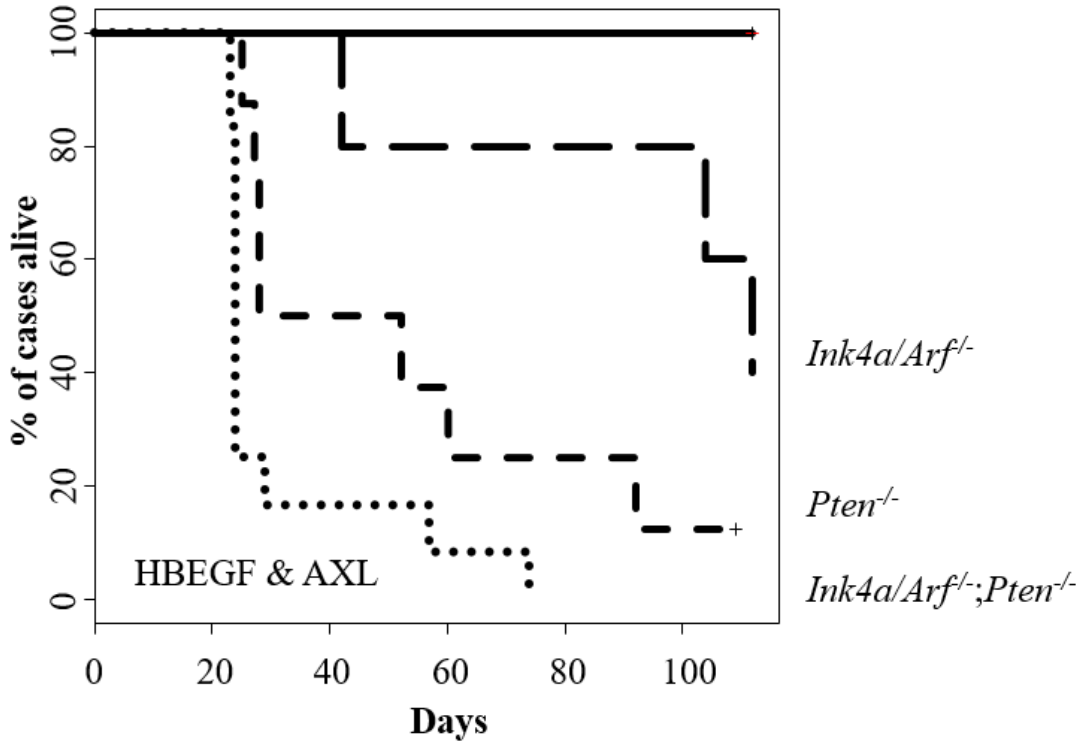

Figure B.1 Survival analysis of different cohorts of Nestin-TVA mice injected with HBEGF, Cre and/or AXL. Kaplan-Meier survival analysis of Nestin-TVA;*Ink4a/Arf*$^{lox/lox}$ (n = 5, long dash, P = 0.0315), Nestin-TVA;*Pten*$^{lox/lox}$ (n = 8, short dash, P = 0.002), and Nestin-TVA;*Ink4a/Arf*$^{lox/lox}$;*Pten*$^{lox/lox}$ (n = 12, round dash, P < 0.001) mice injected with viruses containing HBEGF, AXL, and Cre compared with injection of viruses containing AXL and Cre alone in Nestin-TVA;*Ink4a/Arf*$^{lox/lox}$;*Pten*$^{lox/lox}$ (n = 6, solid line).

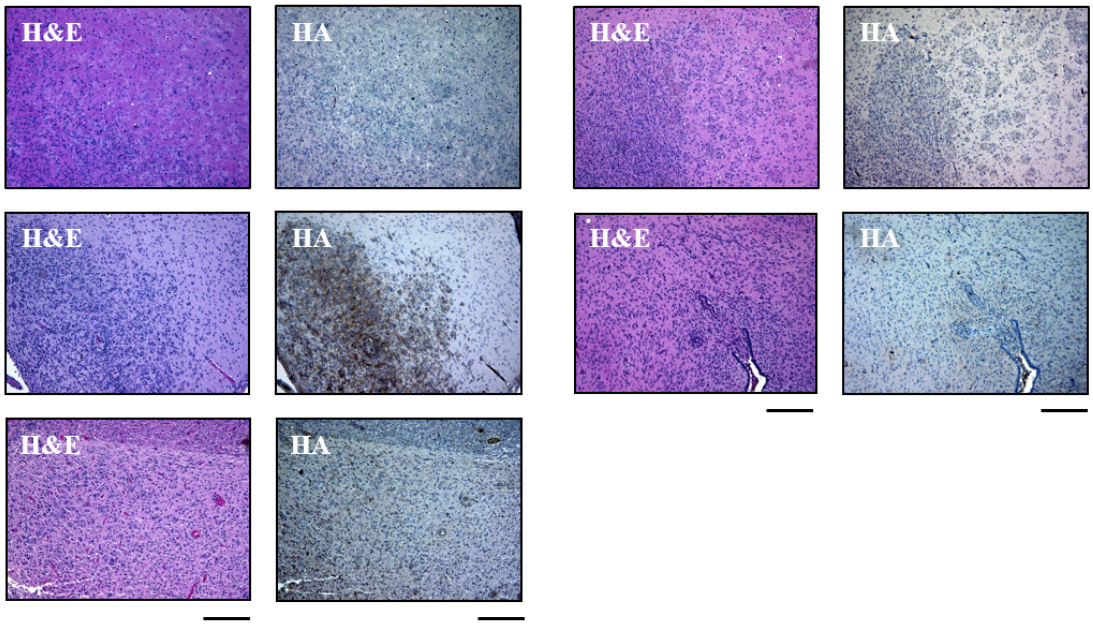

Figure B.2 Expression of AXL in HBEGF-driven tumors in the context of *Ink4a/Arf* loss. Representative H&E and HA immunohistochemistry images of HBEGF-driven tumors in Nestin-TVA;*Ink4a/Arf*$^{lox/lox}$ mice injected with viruses containing HBEGF, Cre, and HA-tagged AXL. Scale bars represent 300 μm.

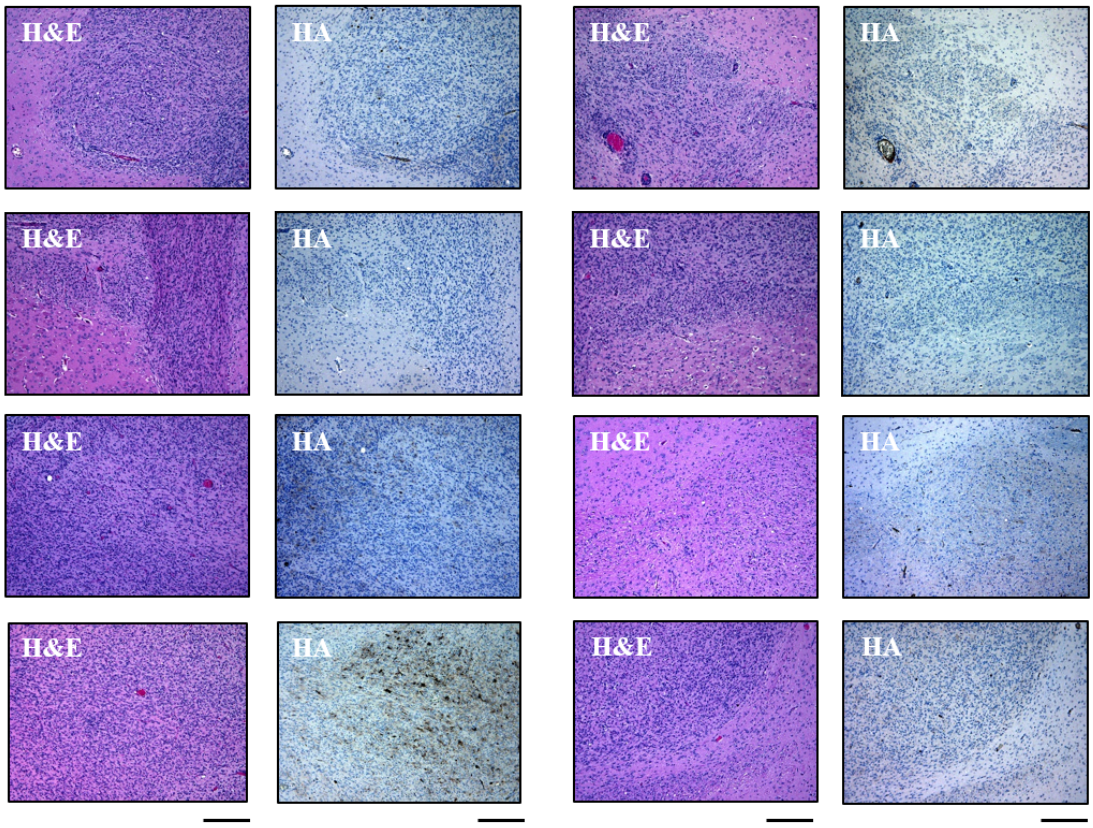

Figure B.3 Expression of AXL in HBEGF-driven tumors in the context of *Pten* loss. Representative H&E and HA immunohistochemistry images of HBEGF-driven tumors in Nestin-TVA;*Pten*$^{lox/lox}$ mice injected with viruses containing HBEGF, Cre, and HA-tagged AXL. Scale bars represent 300 μm.

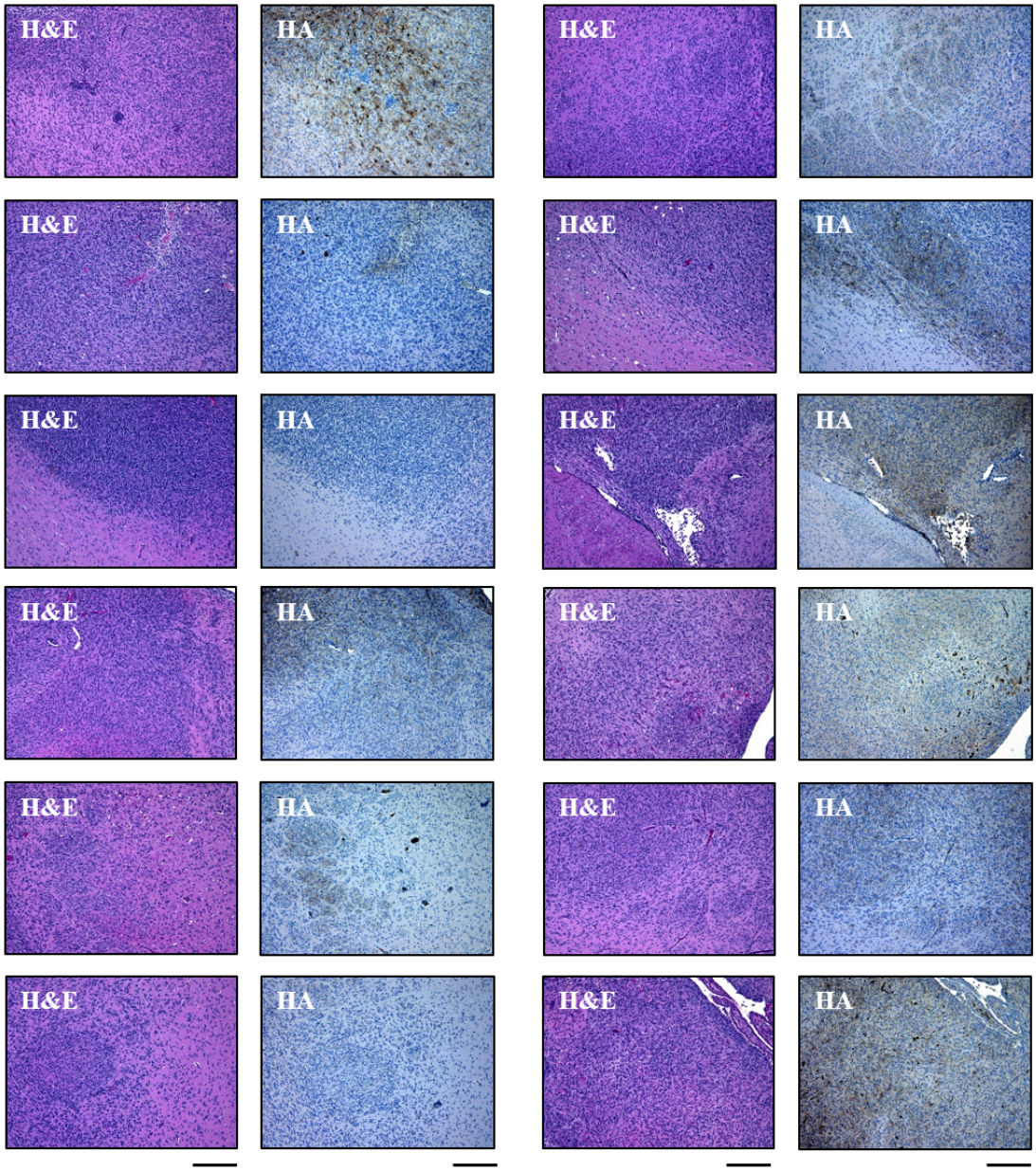

Figure B.4 Expression of AXL in HBEGF-driven tumors in the context of *Ink4a/Arf* and *Pten* loss. Representative H&E and HA immunohistochemistry images of HBEGF-driven tumors in Nestin-TVA;*Ink4a/Arf*$^{lox/lox}$;*Pten*$^{lox/lox}$ mice injected with viruses containing HBEGF, Cre, and HA-tagged AXL. Scale bars represent 300 μm.

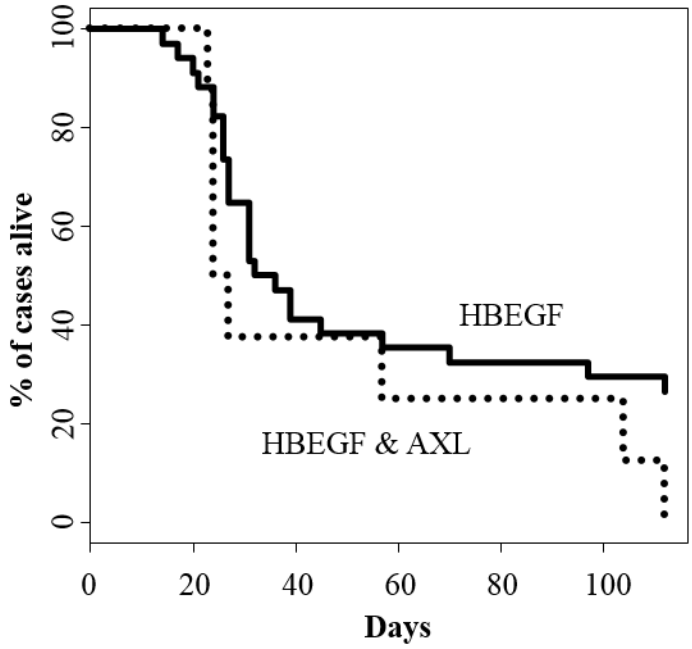

Figure B.5 Comparison of HBEGF-driven tumors with and without exogenous AXL expression. Kaplan-Meier survival analysis of Nestin-TVA;*Ink4a/Arf*$^{lox/lox}$, Nestin-TVA;*Pten*$^{lox/lox}$, and Nestin-TVA;*Ink4a/Arf*$^{lox/lox}$;*Pten*$^{lox/lox}$ mice injected with viruses containing HBEGF, AXL, and Cre with confirmed expression of exogenous AXL (n = 8, round dash) compared with injection of viruses containing HBEGF and Cre alone (n = 34, solid line, $P = 0.158$).

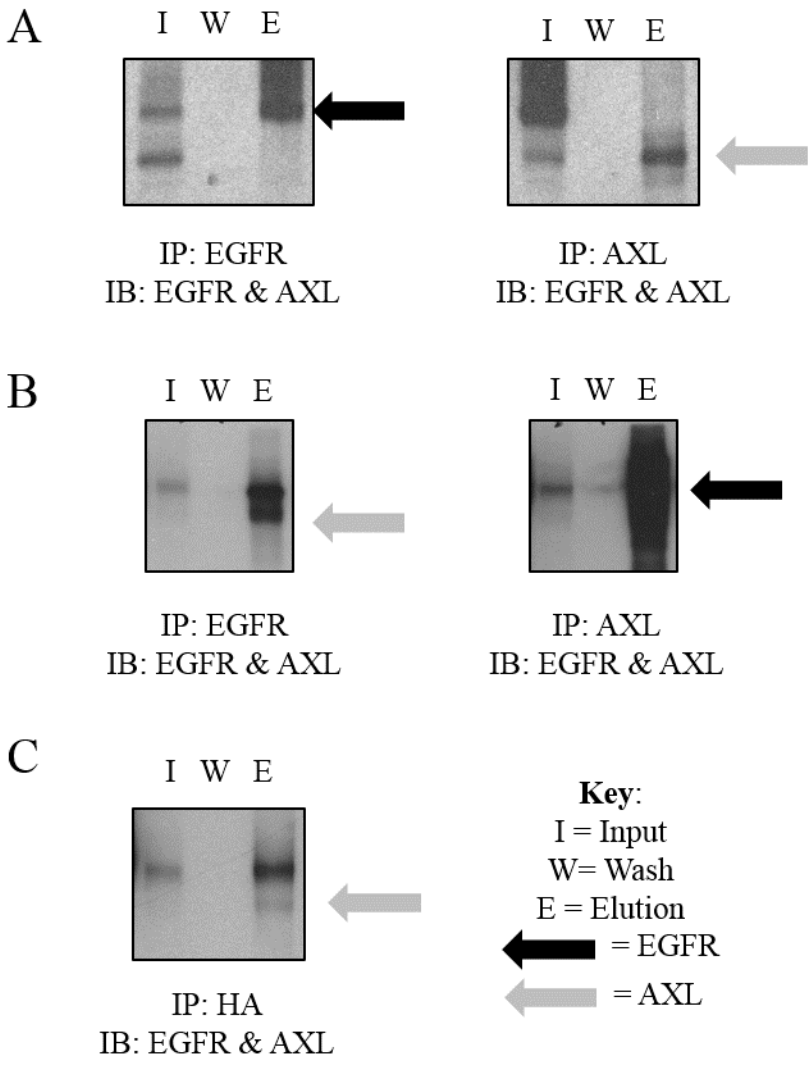

Figure B.6 Co-immunoprecipitation of EGFR and AXL. A: Dynabeads Co-IP assay was performed on 293FT cells that were transfected with plasmids encoding Myc-tagged AXL and HA-tagged EGFR. Normalized cell lysates were subjected to IP using protein A bound to anti-EGFR or anti-AXL antibodies. Input cell lysates, co-IP wash collections, and co-IP elutions were analyzed by western blotting using anti-EGFR and anti-AXL antibodies. Black arrow denotes band corresponding to EGFR while gray arrow denotes band corresponding to AXL. **B:** Same as in A except cells were treated with BS^3 (bis(sulfosuccinimidyl)suberate), a water-soluble, membrane-insoluble N-hydroxy-succinimide ester to crosslink surface proteins. **C:** Same as in B except normalized cell lysates were subjected to IP using anti-HA antibody.

APPENDIX C

EXPRESSION OF PDGFRA IN PDGFA-DRIVEN TUMORS

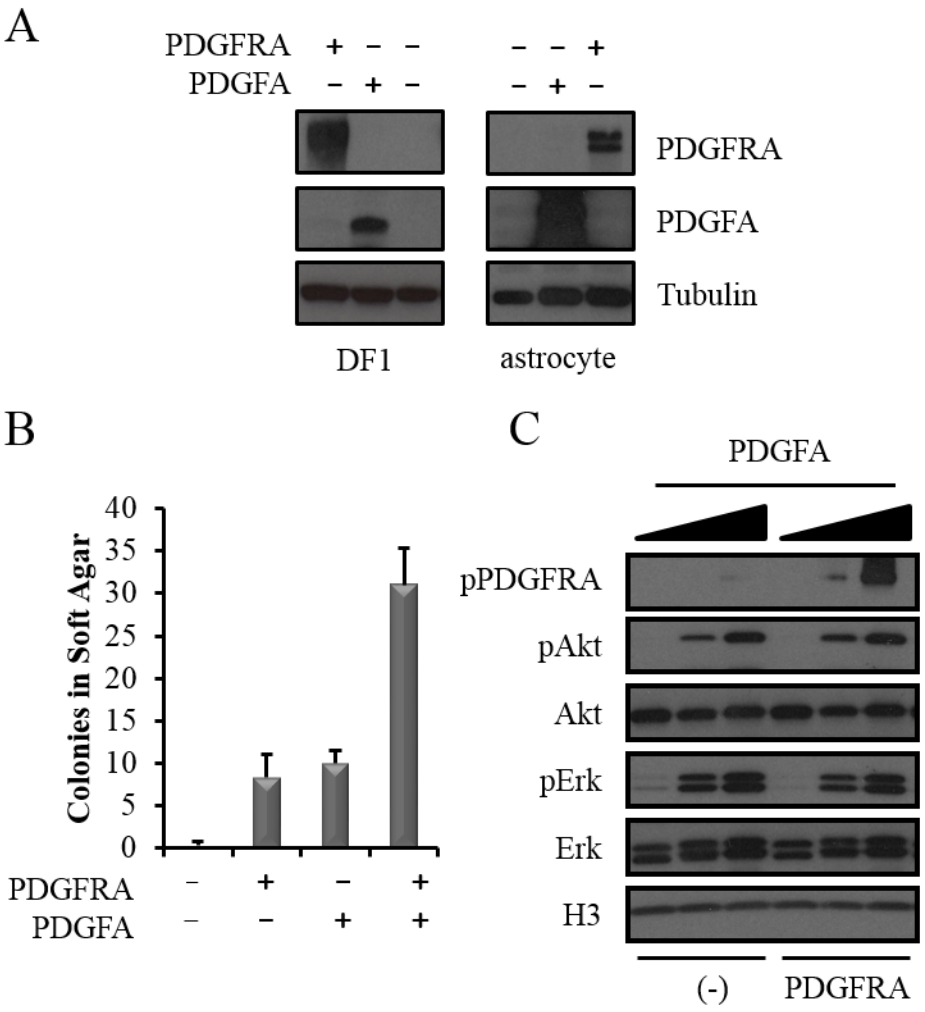

Figure C.1 PDGFA promotes anchorage-independent growth of immortal astrocytes. **A:** Expression of PDGFRA and PDGFA in DF1 cells and Nestin-TVA*Ink4a/Arf*-null mouse astrocytes. **B:** Soft agar colony formation of *Ink4a/Arf*-null astrocytes expressing exogenous PDGFRA and/or PDGFA compared with RCAS-Cre infected control cells. Data are represented as mean ± S.E.M. **C:** Western blot analysis of downstream effector pathways in *Ink4a/Arf*-null astrocytes expressing either endogenous (-) or exogenous (PDGFRA). PDGFA was added to serum-free media at two different concentrations (0.5 ng/ml and 5.0 ng/ml).

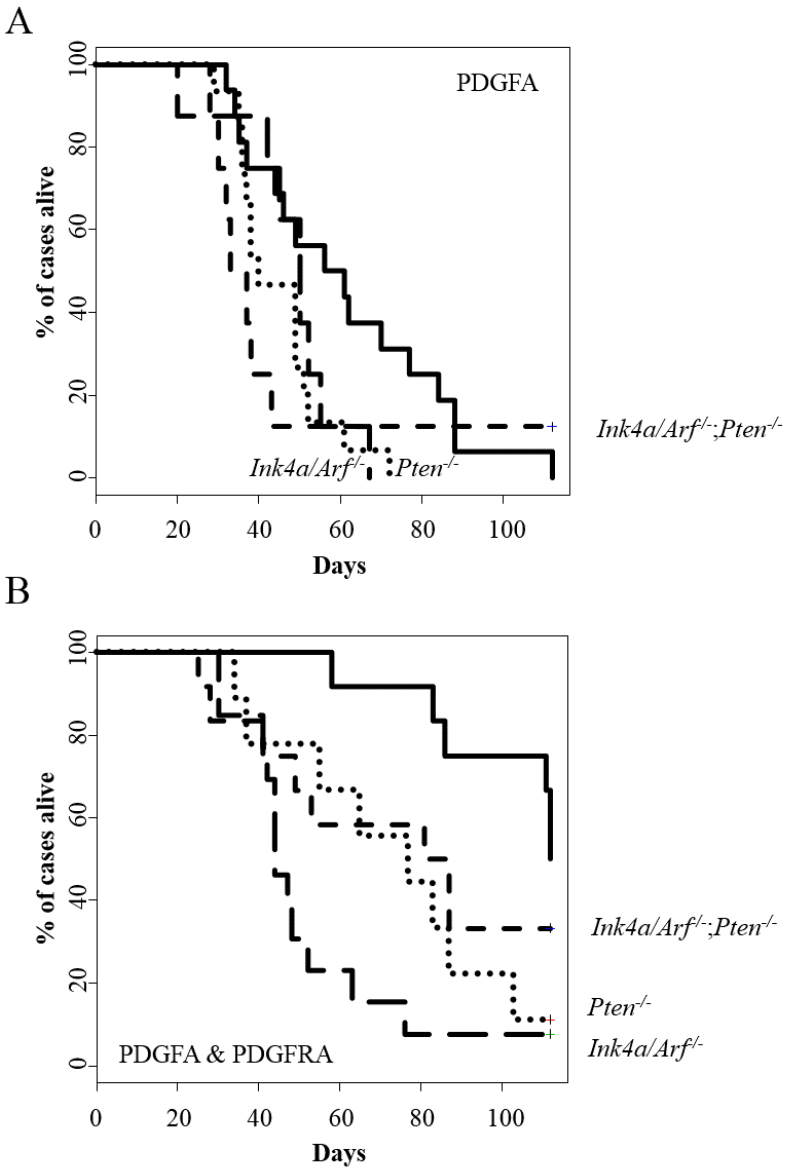

Figure C.2 PDGFA cooperates with loss of *Ink4a/Arf* and *Pten* to promote glioma formation. A: Kaplan-Meier survival analysis of Nestin-TVA;*Ink4a/Arf*$^{lox/lox}$ (n = 8, long dash, P = 0.0998), Nestin-TVA;*Pten*$^{lox/lox}$ (n = 15, round dash, P = 0.0205), and Nestin-TVA;*Ink4a/Arf*$^{lox/lox}$; *Pten*$^{lox/lox}$ (n = 8, short dash, P = 0.228) mice injected with viruses containing PDGFA and/or Cre were compared with injection of viruses containing PDGFA alone in Nestin-TVA;*Ink4a/Arf*$^{lox/lox}$ (n = 16, solid line). **B:** Kaplan-Meier survival analysis of Nestin-TVA;*Ink4a/Arf*$^{lox/lox}$ (n = 13, long dash, P < 0.001), Nestin-TVA;*Pten*$^{lox/lox}$ (n = 9, round dash, P = 0.00697), and Nestin-TVA;*Ink4a/Arf*$^{lox/lox}$;*Pten*$^{lox/lox}$ (n = 12, short dash, P = 0.168) mice injected with viruses containing PDGFA, PDGFRA, and Cre compared with injection of viruses containing PDGFA and PDGFRA in Nestin-TVA;*Ink4a/Arf*$^{lox/lox}$ (n = 12, solid line) mice.

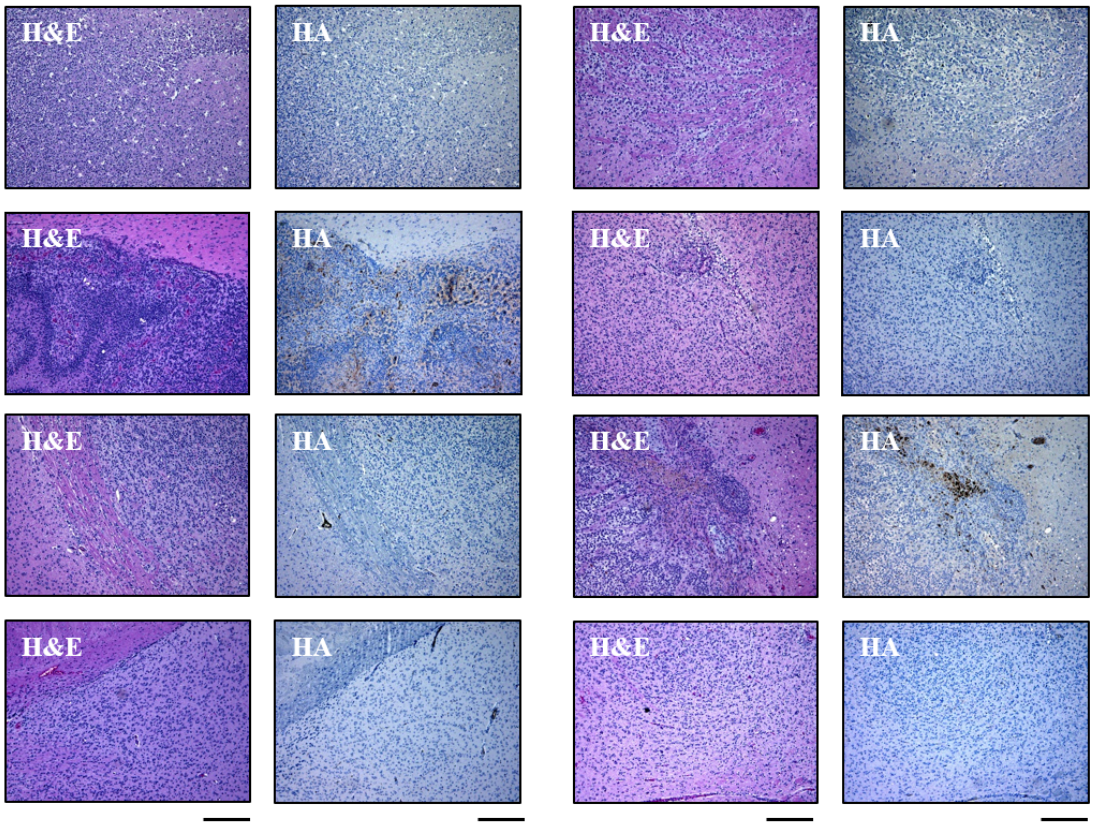

Figure C.3 Expression of PDGFRA in PDGFA-driven tumors. Representative H&E and HA immunohistochemistry images of PDGFA-driven tumors in Nestin-TVA mice injected with viruses containing PDGFA and HA-tagged PDGFRA. Scale bars represent 300 μm.

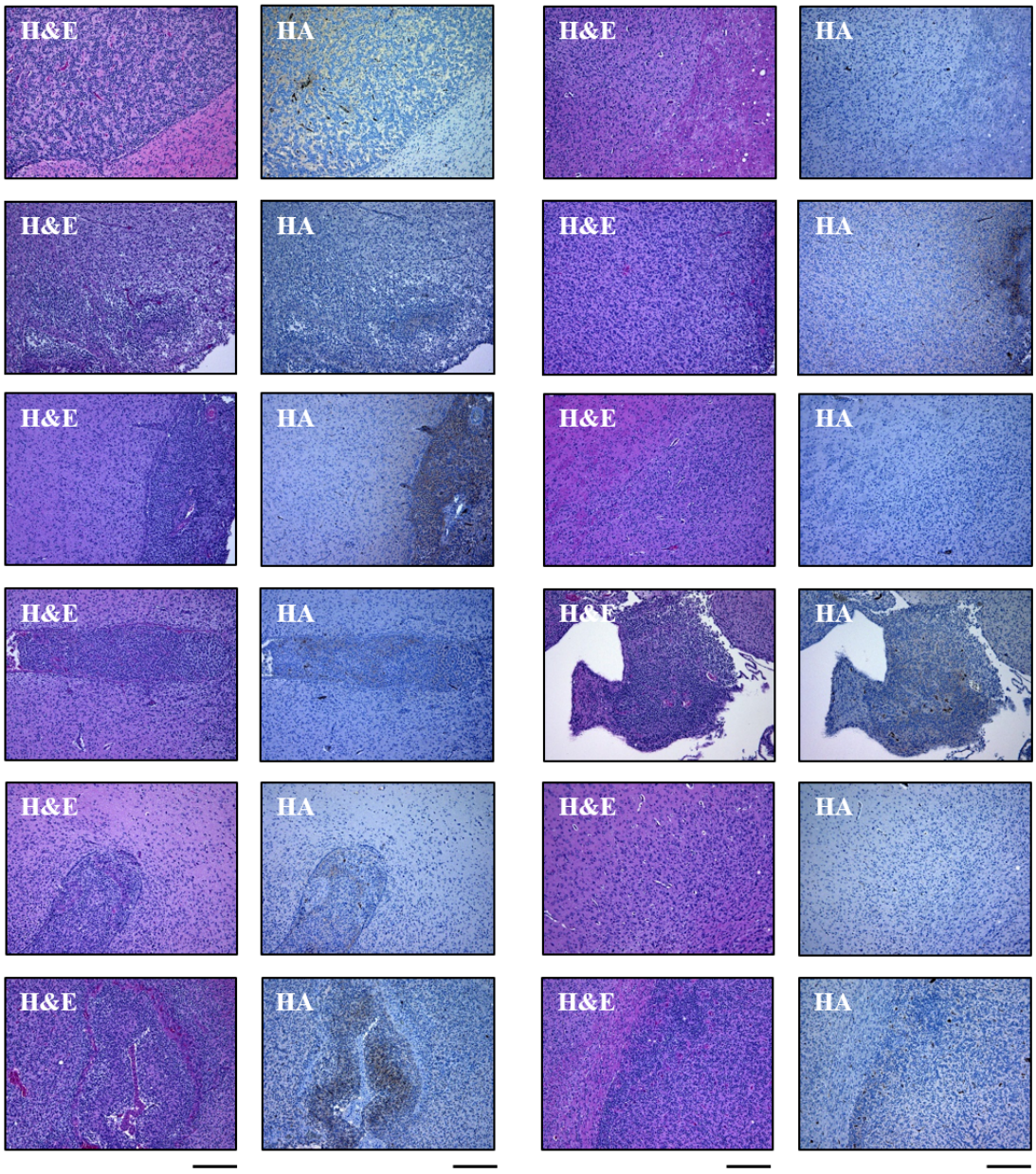

Figure C.4 Expression of PDGFRA in PDGFA-driven tumors in the context of *Ink4a/Arf* loss. Representative H&E and HA immunohistochemistry images of PDGFA-driven tumors in Nestin-TVA;*Ink4a/Arf*$^{lox/lox}$ mice injected with viruses containing PDGFA, Cre, and HA-tagged PDGFRA. Scale bars represent 300 μm.

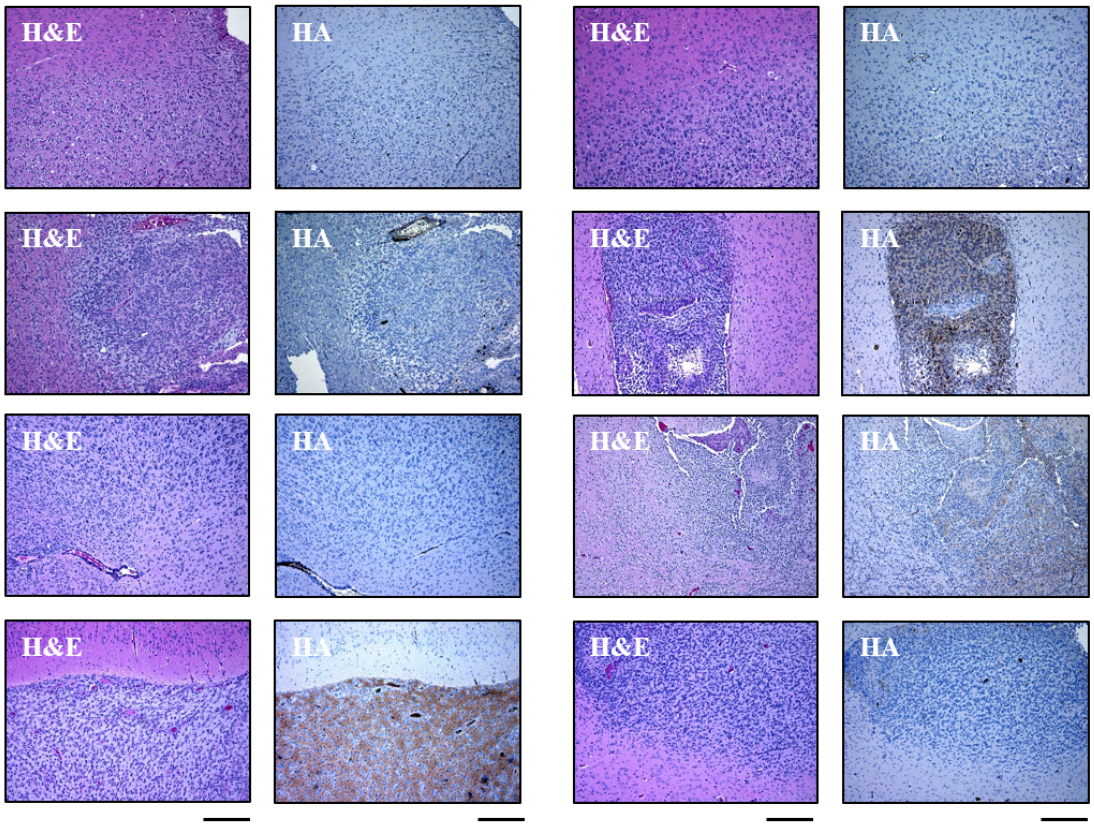

Figure C.5 Expression of PDGFRA in PDGFA-driven tumors in the context of *Pten* loss. Representative H&E and HA immunohistochemistry images of PDGFA-driven tumors in Nestin-TVA;*Pten*$^{lox/lox}$ mice injected with viruses containing PDGFA, Cre, and HA-tagged PDGFRA. Scale bars represent 300 μm.

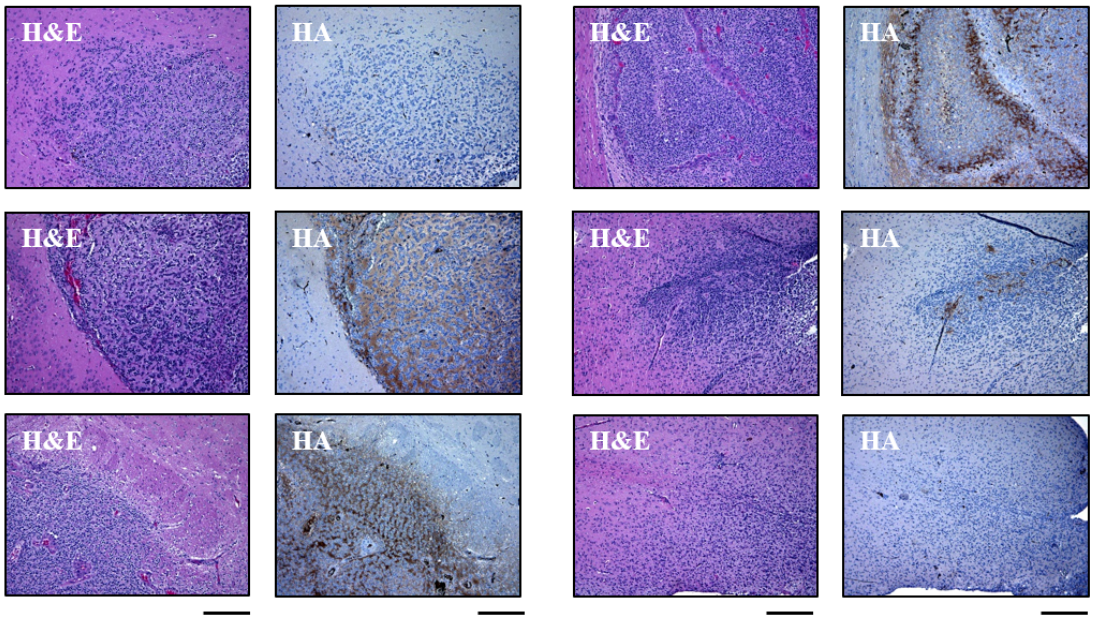

Figure C.6 Expression of PDGFRA in PDGFA-driven tumors in the context of *Ink4a/Arf* and *Pten* loss. Representative H&E and HA immunohistochemistry images of PDGFA-driven tumors in Nestin-TVA;*Ink4a/Arf*$^{lox/lox}$;*Pten*$^{lox/lox}$ mice injected with viruses containing PDGFA, Cre, and HA-tagged PDGFRA. Scale bars represent 300 μm.

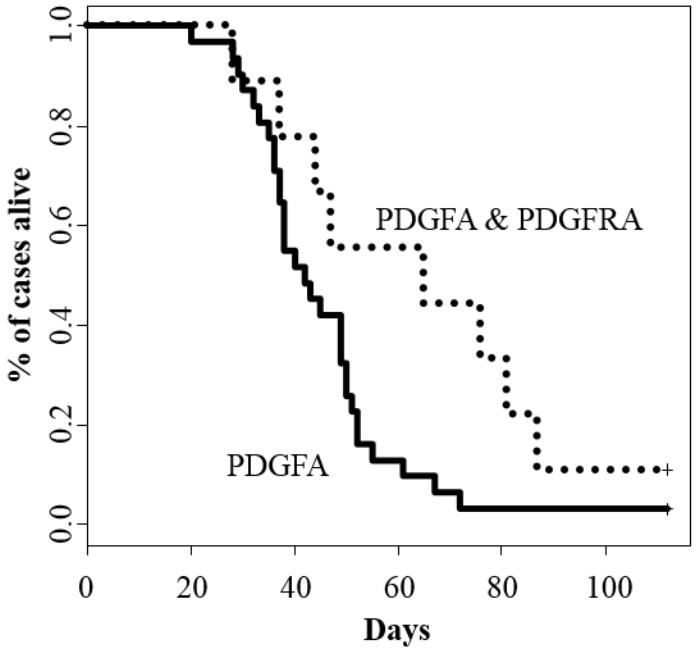

Figure C.7 Comparison of PDGFA-driven tumors in the presence or absence of exogenous PDGFRA expression. Kaplan-Meier survival analysis of Nestin-TVA;*Ink4a/Arf*$^{lox/lox}$, Nestin-TVA;*Pten*$^{lox/lox}$, and Nestin-TVA;*Ink4a/Arf*$^{lox/lox}$; *Pten*$^{lox/lox}$ mice injected with viruses containing PDGFA, PDGFRA, and Cre with confirmed expression of exogenous PDGFRA (n = 9, round dash) compared with injection of viruses containing PDGFA and Cre alone (n = 31, solid line, $P = 0.0402$).

APPENDIX D

GENERATION OF AN INDUCIBLE $BRAF^{V600E}$-DRIVEN GLIOMA MODEL

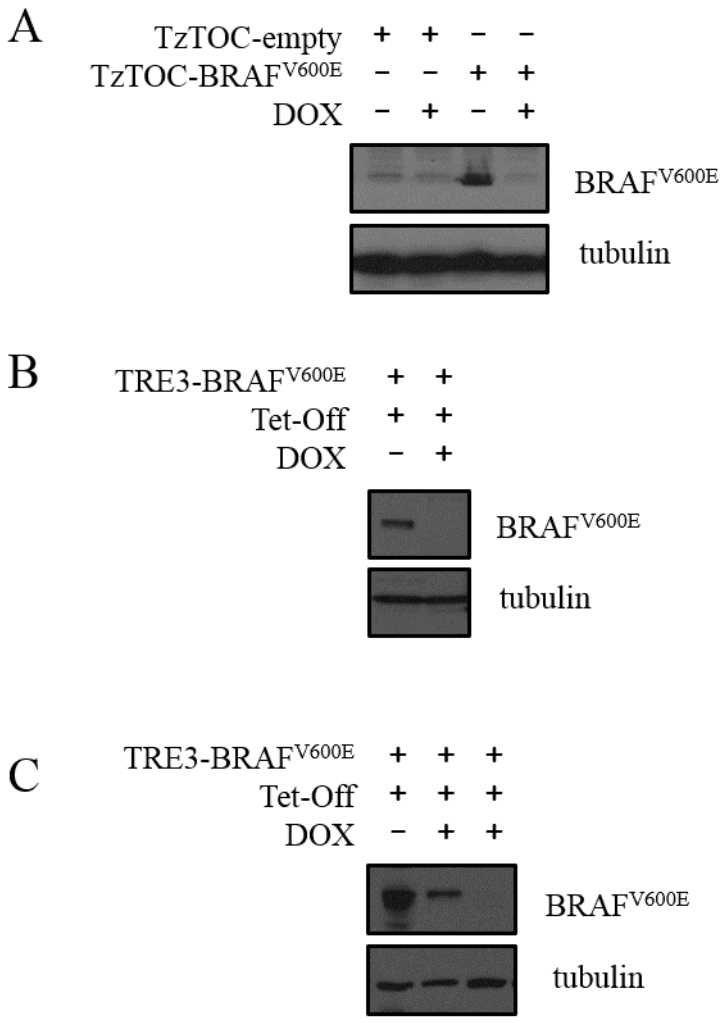

Figure D.1 Suppression of BRAF^{V600E} expression *in vitro*. A: TzTOC-BRAF^{V600E} is a lentiviral vector with two promoters, a tetracycline-responsive promoter upstream of the HA-tagged BRAF^{V600E} and another constitutively active promoter upstream of 3x-FLAG tagged tet-off and c-Myc tagged Cre linked with a P2A, a peptide with a cis-acting hydrolase element for bicistronic expression. Western blot of Nestin-TVA*Ink4a/Arf*-null mouse astrocytes infected with TzTOC-BRAF^{V600E} or TzTOC-empty vector with or without 2 μg/ml of doxycycline for 72 h. **B:** Western blot of Nestin-TVA*Ink4a/Arf*-null mouse astrocytes infected with TRE3-BRAF^{V600E} and tet-off with or without 2 μg/ml of doxycycline for 72 h. **C:** Western blot of tet-off expressing DF1 chicken fibroblasts infected with TRE3-BRAF^{V600E} with or without 2 μg/ml of doxycycline for 24h and 72 h.

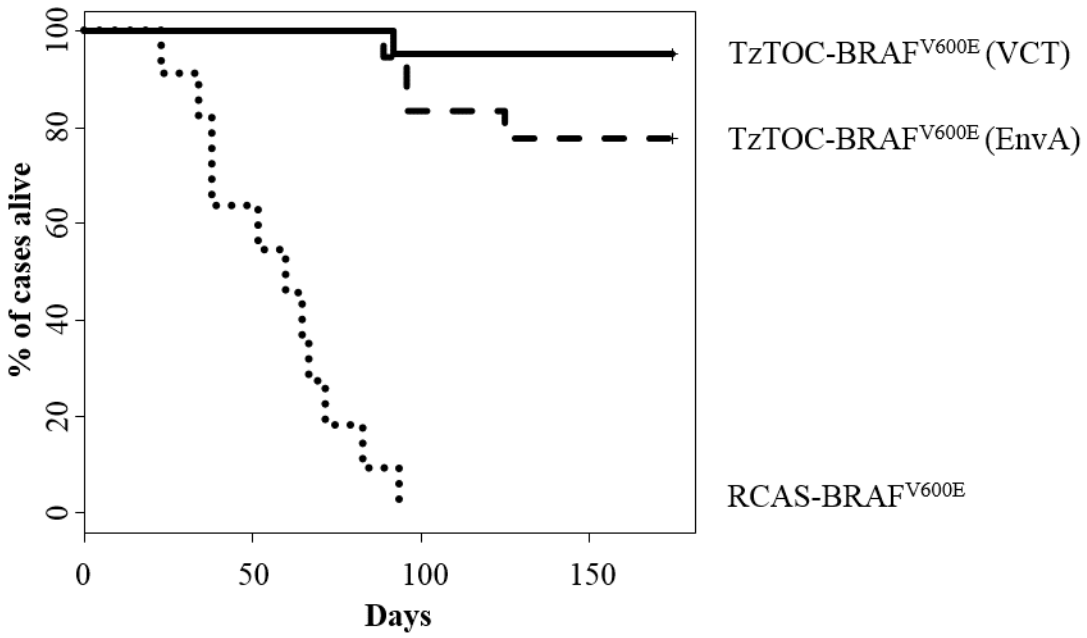

Figure D.2 Inducible BRAF^{V600E} cooperates with loss of *Ink4a/Arf* and *Pten* to promote glioma formation but with lower penetrance compared with RCAS-BRAF^{V600E}. Kaplan-Meier survival analysis of Nestin-TVA;*Ink4a/Arf*$^{lox/lox}$;*Pten*$^{lox/lox}$ mice injected with RCAS-BRAF^{V600E} and RCAS-Cre (n = 11, round dash) compared to mice injected with TzTOC-BRAF^{V600E} pseudotyped with EnvA (n = 18, long dash, $P < 0.001$) and mice injected with TzTOC-BRAF^{V600E} pseudotyped with VCT, a chimeric receptor between VSV-G and EnvA (n = 21, solid line, $P < 0.001$).

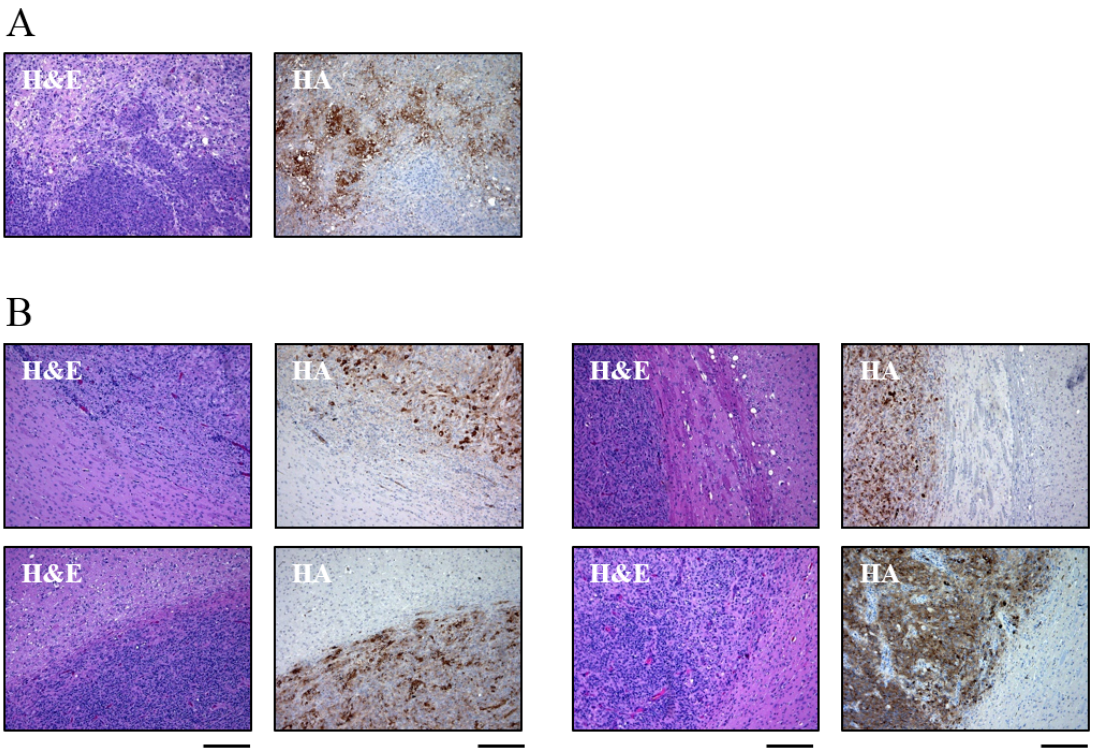

Figure D.3 Confirmation of HA-tagged BRAF^{V600E} expression in BRAF^{V600E}-driven tumors in the context of *Ink4a/Arf* and *Pten* loss. A: Representative H&E and HA immunohistochemistry images of BRAF^{V600E}-driven tumors in Nestin-TVA; *Ink4a/Arf*$^{lox/lox}$;*Pten*$^{lox/lox}$ mice after delivery of TzTOC-BRAF^{V600E} pseudotyped with VCT, a chimeric receptor between VSV-G and EnvA. Scale bars represent 300 μm. **B:** Same as in A but for BRAF^{V600E}-driven tumors in Nestin-TVA;*Ink4a/Arf*$^{lox/lox}$;*Pten*$^{lox/lox}$ mice after delivery of TzTOC-BRAF^{V600E} pseudotyped with EnvA.